Morphing a Straight-Bladed Vertical Axis Wind Turbine Design: CFD-Based Analysis

Thijs J. M. Eijkhout

Morphing a Straight-Bladed Vertical Axis Wind Turbine Design: CFD-Based Analysis

by

Thijs J. M. Eijkhout

Master Thesis

in partial fulfilment of the requirements for the degree of

Master of Science
in Mechanical Engineering

at the Department Maritime and Transport Technology of Faculty
Mechanical, Maritime and Materials Engineering of Delft University of Technology

Student number:	4385993	
MSc track:	Multi-Machine Engineering	
Report number:	2022.MME.8700	
Thesis committee:	Dr. J. Jovanova	Supervisor
	Dr. ir. H. Polinder	Chair
	Dr. ir. C.J. Simão Ferreira	External Examiner
Date:	August 12, 2022	

Summary

Nowadays the wind turbine is an integral part of the energy mix. For a long time, the horizontal axis wind turbine (HAWT) was prioritised over the VAWT and consequently received a lot of attention for research. However, during the oil crisis of 1973, the vertical axis wind turbine (VAWT) managed to gain renewed interest as an alternative energy source. Around the year 1990, the significance of the VAWT waned again until 2010. After 2010 the VAWT finally received the commitment from researchers it deserved. For a long time, the potential of the VAWT has been neglected. As of today, the three most important lift-based VAWT types are the curved-bladed VAWT, helical-bladed VAWT and the straight-bladed vertical axis wind turbine (SB-VAWT). The SB-VAWT proves to be the most potent candidate of the three. The SB-VAWT is an undisputed turbine when it comes to manufacturability and costs. Moreover, the SB-VAWT reaches its highest peak aerodynamic efficiency compared to its vertical counterparts. However, the self-starting capabilities are poor. Because the SB-VAWT is the better choice overall, further improvement could result in a new standard for the wind energy industry. VAWTs are namely able to rotate regardless of the wind direction whereas HAWTs need turbine control for optimal operation. Besides that, the gearbox and generator of the VAWT are located on the ground which reduces maintenance and installation costs. Moreover, the VAWT is suitable to operate in suburban areas for domestic purposes. In this work, the SB-VAWT is analysed for further improvement. Lastly, both solar panel tracking systems and shape memory alloy (SMA) are discussed in the introduction. These two subjects contribute to the concepts that are generated in this work but are not considered during the final VAWT design process. Thus, both subjects are supplementary to the VAWT that is analysed. The main research question of this work reads as follows:

"Does integrating actuation in a vertical axis wind turbine increase the maximum energy harvesting using the wind as an external stimulus?"

To answer this question, the fundamentals of wind energy and wind turbines have been explored. Furthermore, a suitable model has to be chosen for analysing the VAWT. Consequently, the following research questions are developed:

- Which type of VAWT has the most potential to be enhanced?
- What are the key performance indicators (KPIs)?
  - What factors influence the KPIs?
  - What is a suited model for calculating the KPIs?
- Does morphing and/or moving the rotor blades result in enhanced self-starting capabilities and overall performance of the VAWT?

First of all, the wind itself is analysed on how to extract energy from the incoming wind. After the essentials of wind energy are comprehended, the state-of-the-art VAWT is discussed. A journey from the 10th century to the present is made and some potential applications for the (near) future are mentioned. Even an extraterrestrial application is shortly specified. Besides that, the different existing VAWTs and their types are explored. After that, the design methodology is addressed. Design criteria and design constraints of the VAWT design are stated. Thereafter, the design parameters of the VAWT are analysed and examined by existing literature. In addition, the KPIs are identified before the concepts are generated. By applying a morphological chart, two final designs were chosen due to their same score. After evaluating both concepts, the concept which contributes the most to this engineering field is chosen. This is also supported by literature which indicated that there was a research gap present in one of the two concepts. The chosen candidate is the V-VAWT. The V-VAWT is an SB-VAWT of which the two rotor blades are pointing outward under an angle of 45 degrees due to actuating. The diameter of the turbine is 0.6m whereas the height of the rotor blades is 0.4m.

Now that the final concept is chosen, both the V-VAWT and the SB-VAWT are analysed. First, a computer-aided design (CAD) model by the means of SolidWorks is made from the V-VAWT and

the SB-VAWT. After that, a model for analysing both VAWTs has to be chosen. For modelling both VAWTs, ANSYS Fluent simulation software is utilised. ANSYS Fluent uses computational fluid dynamics (CFD) for evaluating the performance of wind turbines. The CAD models are imported into ANSYS Fluent and meshed hereafter. The mesh exists out of two domains; a stationary domain and a rotating domain. The stationary domain is modelled as a cube whereas the rotating domain is modelled as a sphere. Wind speeds of 2, 3, 6 and 10 m/s. After setting up the solution, the standard $k-\omega$ turbulence model is chosen. Afterwards, the dynamic mesh method (DMM) is used for both turbines. With 15,000 time steps of 0.002 seconds, the first 30 seconds are modelled. Dynamic meshing demands a lot of computing power. For this reason, the sliding mesh method (SMM) is introduced to decrease the computing time. However, an estimation has to be made for every tip-speed ratio (TSR). First of all, a relationship between the optimal TSR and turbine solidity has been found in the literature. This made it possible to find the rotations per minute (rpm) at the optimal TSR. Hence, the rpm for every TSR can be obtained. For every SMM simulation, the turbine makes ten rotations for reliable results. Five TSR values were considered using the SMM:

- 0.25
- 0.75
- 1.25
- 1.75
- 2.25

The simulation models were verified by increasing the inlet wind velocity. Validation of the models was done by comparing the models to an experiment. The results of the DMM indicated that the V-VAWT has poor starting capabilities as opposed to the SB-VAWT. In addition, the power coefficient of the V-VAWT is lower than that of the SB-VAWT when the TSR is approximately lower than 1 or higher than 2 using the SMM. Moreover, the average coefficient of lift of the SB-VAWT is higher than that of the V-VAWT. However, the V-VAWT has a higher peak efficiency than that of the SB-VAWT, but the absolute power output is lower at those $Cp(\lambda)$ data points. Furthermore, the SB-VAWT has a wider operational range. For further validation of the model, the SB-VAWT is also compared to the double-stream-tube model (DMST) which is provided by QBlade software. Additionally, the experimental data shown by Yamada et al. (2011) is considered for validation purposes. The data shows that the model is validated. It is not recommended to implement actuation in order to receive the V-shape from the initial SB-VAWT. Even if the power coefficient of the V-VAWT is higher at the optimal TSR, the absolute power output is worse than that of the SB-VAWT. Thus, for small-scale VAWTs, it is not effective to morph the SB-VAWT into a V-VAWT. That is also the case for the operational range. Still, it might be effective to morph the SB-VAWT into a V-VAWT when the turbine is of a larger size.

Acknowledgements

First and foremost, I could not have undertaken this journey without Dr. Jovana Jovanova. She allowed this work to be my own work but guided me in the right direction whenever necessary. Besides that, she was always available when I needed her. I would like to extend my sincere thanks to Dr. ir. Henk Polinder who gave me new insights after every discussion which made it possible to improve my work. Additionally, I am also grateful to Dr. ir. M.J.B.M. Pourquie, for steering me in the right direction with the CFD modelling. Thanks should also go to Dr. ir. C.J. Simao Ferreira who was a great source of inspiration for this work.

I would also like to thank my parents, brother and girlfriend. They were always supporting me during this inspiring year in which we also welcomed my daughter Zora. Thank you!

Thijs Eijkhout
August, 2022

Contents

List of Tables

List of Figures

Nomenclature

List of abbreviations

AoA	Angle of attack
APC	Average power coefficient
BEM	Blade element momentum
BET	Blade element theory
CAD	Computer-aided design
CFD	Computational fluid dynamics
DMM	Dynamic mesh method
HAWT	Horizontal axis wind turbine
KPI	Key performance indicator
LDR	Light-dependent resistor
MST	Multiple-stream tube
NACA	National Advisory Committee for Aeronautics
Nitinol	Nickel Titanium Naval Ordnance Laboratory
OJF	Open jet facility
OWSME	One-way shape memory effect
RANS	Reynolds-averaged Navier–Stokes
rpm	Rotations per minute
SB-VAWT	Straight-bladed vertical axis wind turbine
SMA	Shape memory alloy
SME	Shape memory effect
SMM	Sliding mesh method
SST	Single-stream tube
TSR	Tip-speed ratio
TWSME	Two-way shape memory effect
VAWT	Vertical axis wind turbine
DMST	Double-multiple-stream tube

List of Greek Symbols

α	Angle of attack
β	Pitch angle
Δt	Step size
δ	Rotor blade angle
β_t	Tilt angle
ϵ	Strain
θ	Azimuth angle
λ	Tip-speed ratio
ν_{air}	Kinematic viscosity of air
ρ_{air}	Air density
σ	Stress
ω	Angular velocity

List of Roman Symbols

A	Swept area
A_f	Austenite finish temperature
A_r	Aspect ratio
A_s	Austenite start temperature
M_f	Martensite finish temperature
M_s	Martensite start temperature
C	Cell size
c	Chord length
C_{apc}	Average power coefficient
C_p	Power coefficient
C_T	Torque coefficient
$C_{pressure}$	Pressure coefficient
D	Rotor diameter
E_k	Kinetic energy
F_D	Drag force
F_L	Lift force
F_N	Normal force
F_T	Tangential force
H	Blade height
I	Turbulence intensity
N	Number of blades
P_∞	Static pressure
P_m	Mechanical power
P_{wind}	Wind power
R	Rotor radius

Re_c	Local Reynolds number
T	Temperature
T_r	Rotor torque
U	Induced velocity
V	Tangential velocity of the rotor
V_∞	Undisturbed wind stream
V_{int}	Outer rim velocity of the rotating domain
W	Relative wind velocity
$\dot{m}_{air}$	Mass flow of air

CHAPTER 1

Introduction

1.1 Research context

Following the Paris Agreement, the European Council committed to reduce greenhouse gas emissions in 2030 by 40% compared to the base year of 1990. Furthermore, the contribution of renewable energy sources to the total energy consumption of the European Union has to be at least 27% by the year 2030[12]. In this report, a new innovation is proposed in order to contribute to this energy transition by improving a straight-bladed vertical axis wind turbine (SB-VAWT) by using actuation. Moreover, solar panel tracking systems are also considered.

1.2 Research problem

Many solar panels tend to be static as they are placed in a fixed position with respect to the sun. To utilise their full potential, often solar tracking systems are used for increasing their efficiency. However, additional actuation and control are generally necessary for arranging the solar panel in a favourable position regarding the position of the sun. The two prevailing categories of solar panel tracking systems are the single-axis tracking systems and the dual-axis tracking systems. The single-axis tracking system is able to pursue the sun using only one axis of rotation (horizontal, vertical or tilted), usually starting with respect to the sunrise in the east and tracking the sun until it sets in the west. The dual-axis tracking system uses two axes together: The horizontal axis and the vertical axis. Both tracking categories are depicted in Fig. 1 where β_t is the tilt angle. Furthermore, the main mechanisms of tracking can also be divided into four approaches:

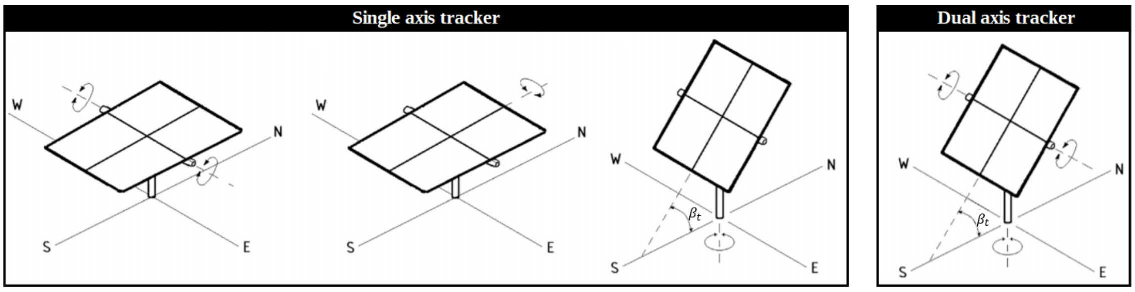

Figure 1: Single-axis and dual-axis solar panel tracking systems

- Active tracking
- Passive tracking
- Chronological tracking
- Manual tracking

Active tracking uses light-dependent resistor (LDR) sensors in order to trigger actuation for aligning the solar panel in an optimal position with respect to the sun. This results in a higher power output[15][98]. However, it increases the complexity of the system as microcontrollers, actuation, extra materials and more maintenance are necessary[52][41]. Another drawback of active tracking is that LDR sensors are less capable of functioning during overcast days. An energy gain of 20% up to 40% using active solar tracking is achievable depending on the type of actuation, single- or-dual axis system, solar panel type and the weather[85]. The passive tracking approach only takes the heat of the sun in consideration by using the heat for thermal expansion in specific materials. This expanding and contracting behaviour of materials, due to temperature differences, results in actuating the solar panel perpendicular to the sun. It is in theory possible to integrate shape memory alloy (SMA) as an actuator for this kind of tracking system using the heat of the sun as a stimulus. It also has an energy gain of 39% compared to static solar panels[96]. Also, a disorder of balance between two states may be exploited. For example, a pressure difference between two cylinders filled with a refrigerant liquid which are heated by solar radiation[48]. Fig. 2 shows such an arrangement. When the sun rises, one of the refrigerant cylinders that sees first light is radiated with solar beams. The refrigerant liquid is heated which results in a rise in pressure and forces the liquid to the other cylinder. Hence, the solar panel rotates around the pivot point with the position of the sun. Passive tracking systems do not need actuation, are easy to install and have low maintenance costs[11]. Nonetheless, their accuracy is rather low and strong dependence on weather conditions. Also, their complexity is significantly increased when opting for a dual-axis tracker which also influences the accuracy even more. Using the pressure difference method, an energy gain of at least 23% may be achieved compared to fixed solar panels[35].

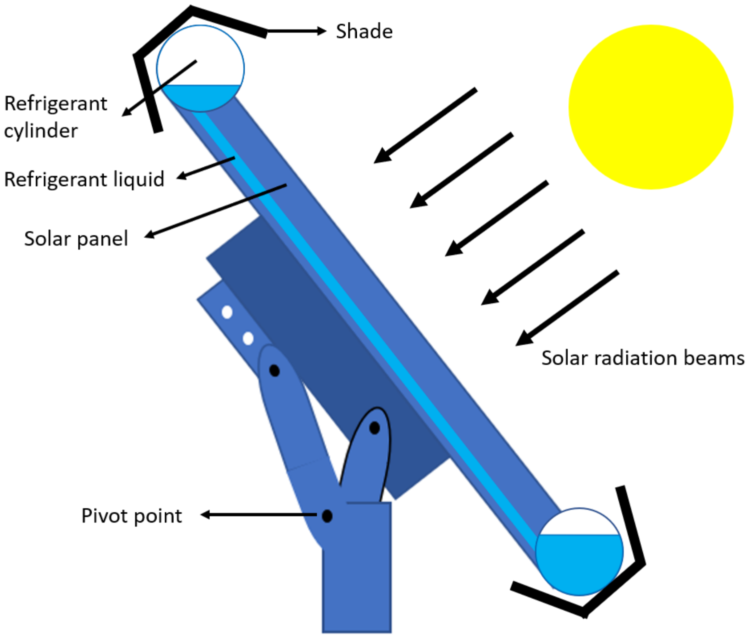

Figure 2: Passive solar tracking systems using pressure differences due to solar radiation

Both active and passive tracking are a continuous process whereas chronological tracking operates discontinuous. The solar panel rotates with a predetermined angle or angles, depending on whether the system is single-axis or dual-axis. The rotation finds place after a certain interval in order to move the solar panel in the preferred position with respect to the sun. Due to the fact the solar panel only rotates during fixed periods, the amount of energy required for actuation is less compared to active tracking[16][37]. Furthermore, chronological tracking is also the more efficient option during overcast days as active tracking required LDR sensors[120]. The preferred angle of rotation is 15° per hour in the case of a chronological single axis tracker[100][110]. Depending on the weather, the type of solar panel, whether the dual or single axis arrangement is used and the actuation technology, chronological tracking improves the net energy production by 8.5% up to even 40% as opposed to stationary solar panels[60][120]. The last mechanism is manual solar tracking. This is a straightforward technique. The solar panels are manually adjusted for a certain period. The sun has a lower altitude angle in the winter than it has in the summer. Therefore, the tilt angle of the solar panel has to be adjusted in order to receive the best solar radiation during that period. Manual tracking increases the energy gain between 10% to 17% depending on whether the panels are adjusted once in a year or season, respectively[3]. This may even increase up to 31% when the angle is adjusted daily[132]. Manual tracking dramatically reduces the complexity of the system as there is no controller and actuation needed. Also, when adjusting the angle, one has the opportunity to clean the solar panels in order to reduce soiling. Wind energy also plays an important role in the energy transition. By 2030, The Global Wind Energy Council estimates that 2.110 GW of power is generated using wind as a renewable energy source which accounts for 20% of the global energy needs[29]. Besides the familiar horizontal axis wind turbine (HAWT), which is used for large-scale energy harvesting, the alternative is a vertical axis wind turbine (VAWT) which is used on a smaller scale. Examples of the HAWT and the VAWT are presented in Fig. 3 and Fig. 4, respectively.

Figure 3: Horizontal axis wind turbines

Figure 4: Helical-bladed vertical axis wind turbine

The main characteristic that the HAWT and the VAWT have in common, is that both of these turbines extract energy from the wind in order to convert it to mechanical energy. The annual energy output of wind turbines is often defined by the capacity factor. The capacity factor is calculated by dividing the actual annual energy output by the maximum theoretical energy output the turbine can achieve in the 8760 hours a year has. Needless to say, if there is no wind or the wind speed at a given time is too low, the capacity factor of wind turbines decreases. Furthermore, there are some key differences between the HAWT and the VAWT which are given in Table 1.

Table 1: Characteristics of HAWT and VAWT[13][59][97][102][127]

HAWT	**VAWT**
Relatively high volume production	Produces energy regardless of wind direction
Relatively high efficiency	Axis of rotation is perpendicular to wind direction
Immune to backtracking effect	Requires relatively little space
Requires a lot of space	Relatively easy to maintain
Complex maintenance and installation	Produces energy at low wind speeds
Self-starting	Relatively low noise production
Turbine control is vital for optimal operation	Can be installed in urban areas
Produces quite an amount of noise	Relatively low efficiency
Operational during high wind speeds	Relatively low starting torque
High reliability	Can be used for domestic purposes

Solar panels and wind turbines, both vertical axis and horizontal axis, are a well-established technology that is proven to contribute to the energy transition. Nonetheless, integrating smart materials into these structures is still an undiscovered field in engineering. A popular smart material is Nitinol (Nickel Titanium Naval Ordnance Laboratory) which is accidentally discovered by William J. Buehler and Frederick Wang in 1959[62]. During a meeting, a sample of Nitinol was deformed. After the deformation, the sample was heated up and it returned to its original shape. Therefore, the overarching name for these materials is called SMA. This process is called the shape memory effect (SME). Another interesting characteristic of Nitinol is the relatively high strain recovery it can achieve, namely up to 8%[128] which is called superelastic (also known as pseudoelastic) behaviour. Besides Nitinol, there are a lot of other SMAs available. However, not every SMA is commercially available due to the fact it can be a reasonably expensive material. Common SMAs which are accessible for commercial use besides Nitinol are Cu-Al-Ni, Cu-Zn-Al and Ni-Ti-Cu [50][31][107]. Furthermore, there are two types of SMEs which are called the one-way shape memory effect (OWSME) and the two-way shape memory effect (TWSME). OWSME occurs when the SMA is plastically (but reversible) deformed after applying a load with the result that the SMA can only return to its original shape after heating takes place. The OWSME process on a macroscopic scale is shown in Fig. 5 whereas Fig. 6 presents the process on a microscopic scale with the different possible crystal structures.

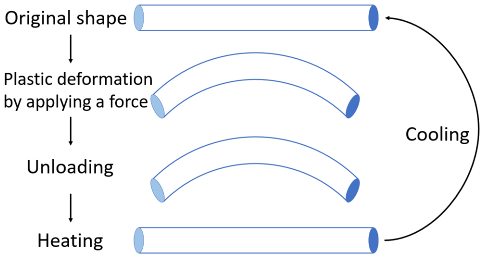

Figure 5: Macroscopic one-way shape memory effect

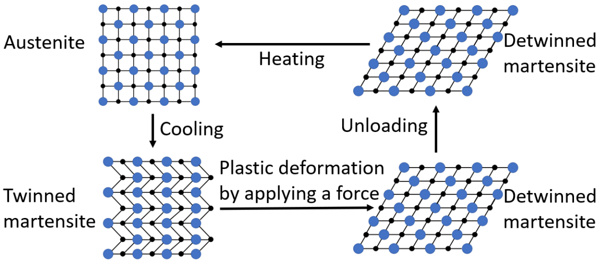

Figure 6: Microscopic one-way shape memory effect

On the other hand, TWSME has two scenarios where it remembers two different shapes: One deformed shape is remembered throughout the cooling process whereas the other deformed shape is remembered during the heating procedure. Thus, an SMA with the TWSME has the ability to memorialise two shapes: One for high temperatures and one for low temperatures. In order to obtain these shapes, the original shape has to undergo a severe plastic, irreversible deformation. The TWSME process is demonstrated on a macroscopic level in Fig. 7 and on a microscopic level in Fig. 8. The commercial use of TWSME for SMAs is often proven to be inconvenient as the material must be trained. Furthermore, the strain recovery declines to 50% compared to the strain recovery for OWSME when using the same SMA[51][89][104]. Moreover, at higher temperatures, the strain of TWSME for SMA declines considerably fast[68][69]. This is another argument that the OWSME is preferred over TWSME considering reliability, consistency and costs.

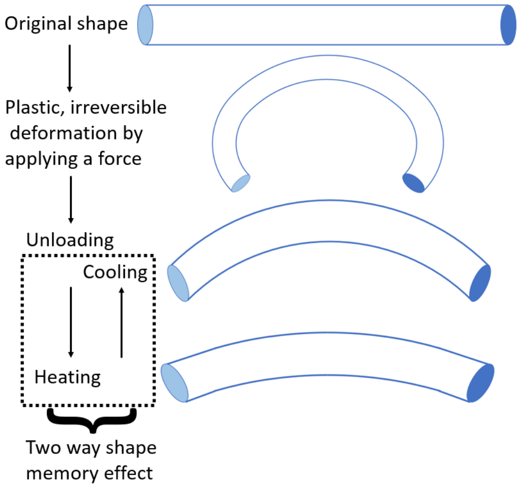

Figure 7: Macroscopic two-way shape memory effect

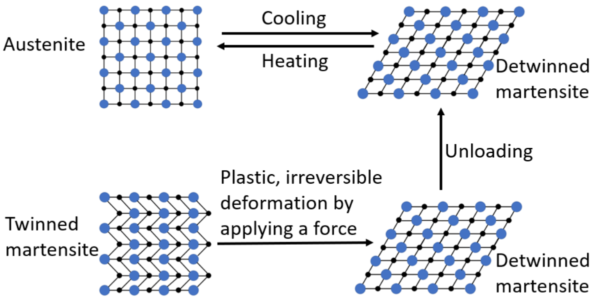

Figure 8: Microscopic two-way shape memory effect

The phase transformation temperatures of a SMA are the martensite start temperature M_s, martensite finish temperature M_f, austenite start temperature A_s and the austenite finish temperature A_f. Fig. 9 shows all the relevant characteristics of SMA in a 3D-stress-strain-temperature graph, where also σ represents the stress, T the temperature and ϵ the strain.

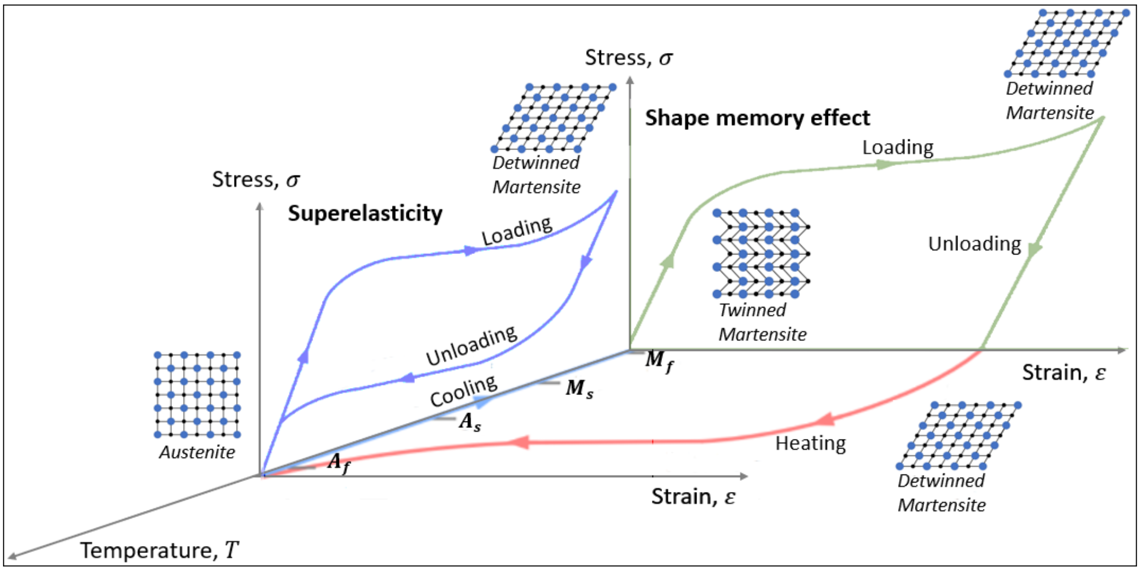

Figure 9: 3D Stress-strain-temperature of shape memory alloys showing the shape memory effect and their superelastic behaviour

1.3 Research objective

As mentioned before, little to no research has been done on integrating smart materials with renewable energy sources such as wind and sun. Even hybrid innovations using the wind and the sun as external stimuli simultaneously are still a fairly unexplored field. There are a lot of challenges awaiting the energy transition to take place. Therefore, combining the VAWT with a solar panel (tracking system) and integrating an actuator might drastically increase the efficiency of such a hybrid power unit. Hence, the research goal is *to apply actuation for maximising the energy output using wind energy as an external stimulus.* During this work, combining all topics proved to be challenging due to time constraints. Therefore, the main scope of this work is to improve on existing VAWTs using actuation for a (temporarily) change of its shape increasing its overall performance.

1.4 Research questions

The main research question developed for this thesis reads as follows:

> *"Does integrating actuation in a vertical axis wind turbine increase the maximum energy harvesting using the wind as an external stimulus?"*

To answer this question, the fundamentals of wind energy and wind turbines have been explored. Furthermore, a suitable model has to be chosen for analysing the VAWT. Consequently, the following research questions are developed:

- Which type of VAWT has the most potential to be enhanced?
- What are the key performance indicators (KPIs)?
  - What factors influence the KPIs?
  - What is a suited model for calculating the KPIs?
- Does morphing and/or moving the rotor blades result in enhanced self-starting capabilities and overall performance of the VAWT?

1.5 Research scope

Before proposing a design, a thorough literature review[34] has been carried out regarding SMA characteristics, SMA applications, solar panels (and their tracking methods) and general characteristics of VAWTs. While there is much literature to find for each individual subject, there is little to find when combining these aforementioned topics.

However, the research scope of this work is limited to VAWTs. Therefore, SMA actuation is only considered as an option for VAWT actuation while also other methods of actuation are a possibility. Likewise, the solar panel (tracking system) are considered supplementary. Moreover, the conceptual designs only consider the straight-bladed vertical axis wind turbine (SB-VAWT) for the reason that its counterparts are generally performing somewhat worse regarding certain characteristics of a VAWT. This is supported by literature and will be explained later in this work.

1.6 Research outline

With regard to having a clear overview of this work, an outline has been made which is presented in Fig. 10.

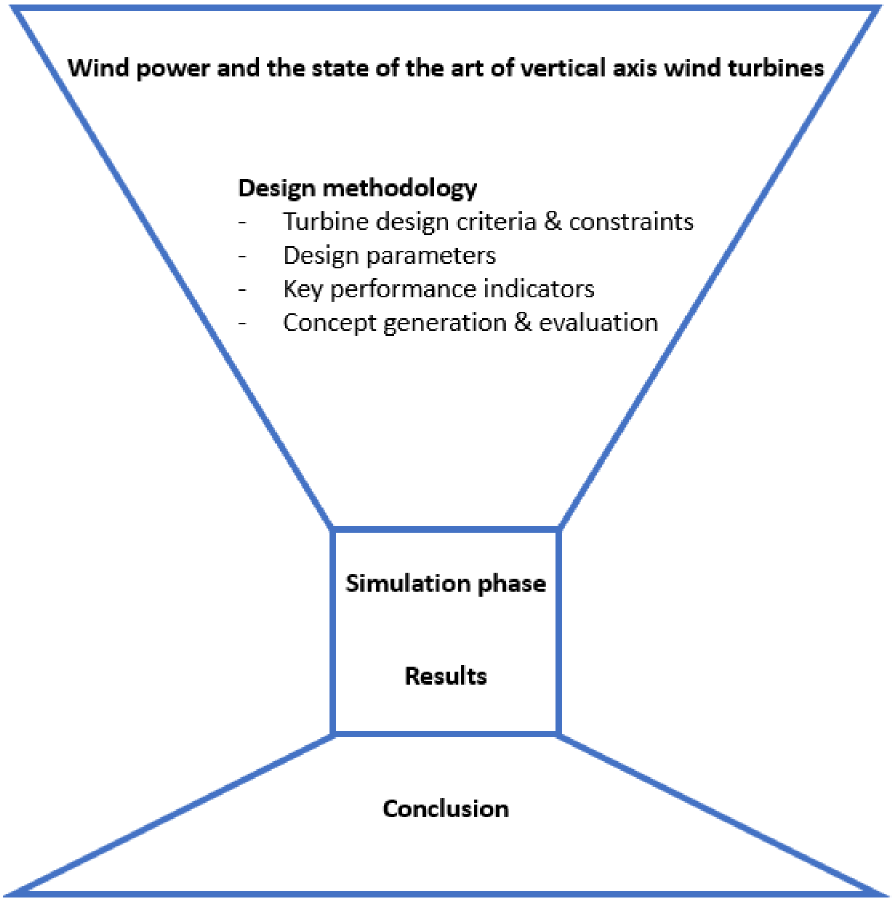

Figure 10: Research outline of this study

First of all the basic principles of wind energy are discussed. After that, the history and basic mechanics of different VAWTs are discussed. Moreover, the state of the art VAWT is discussed with its (future) potential for society. Even extraterrestrial conditions are considered for the wind turbine. After that, the design methodology is explained which covers the design criteria and constraints. Besides that, the design parameters are revealed together with the key performance indicators (KPIs). After setting up the design boundary conditions, VAWT concepts are generated together with potential solar panel placement within the system. A final concept will be chosen keeping the research gap in mind in order to contribute to this particular field of engineering. The concept will be analysed with simulation software ANSYS Fluent and after the results and concluding remarks will be discussed.

CHAPTER 2

Background

2.1 Response time of SMA actuation

The temperature of a wire made of SMA can be increased due to Joule heating. As mentioned before, the material undergoes a phase transformation because of this temperature increase which results in relatively high actuation forces and large strains. Increasing the applied current decreases the response time (the time required to reach maximum force) of SMA. Inducing a current of 1.5 ampere and 2 ampere on a 0.48 mm diameter Nitinol wire results in a response time of 10 seconds and 5 seconds, respectively[30]. Furthermore, enlarging the diameter of an SMA wire will also result in a higher response time if the same applied current is used[61]. In addition, for improving the operational frequency of an SMA actuator, when using a spring or wire, a cooling method has to be chosen[101].

2.2 Wind power

In order to understand the principles of wind power, a derivation is made. The kinetic energy E_k consists of a certain mass of an object which carries out a transnational or rotational motion. In the case of wind, this is the undisturbed wind speed V_∞ and the mass of the air m_{air}. Hence, the kinetic energy of advancing air is determined by (1).

$$E_k = \frac{1}{2} m_{air} V_\infty^2 \tag{1}$$

Subsequently, the wind power P_{wind} is realised by differentiating the kinetic energy with respect to the time shown in (2) where $\dot{m}_{air}$ is the mass flow of the air.

$$P_{wind} = \frac{dE_k}{dt} = \frac{1}{2} \dot{m}_{air} V_\infty^2 \tag{2}$$

The mass flow of air in turn depends on the swept area A of the wind turbine blades, air density ρ_{air} and V_∞. The relationship between these variables is presented in (3).

$$\dot{m}_{air} = A \rho_{air} V_\infty \tag{3}$$

Finally, by substituting (3) into (2), the wind power which can be converted into energy is given by (4).

$$P_{wind} = \frac{1}{2} A \rho_{air} V_\infty^3 \tag{4}$$

Analysing (4), the undisturbed wind speed has the largest effect on influencing the available wind power that may be converted as the available wind power is proportional to the cubic of the undisturbed wind speed. Thus, small variations of wind speed have a large effect on the available wind power that is to be converted into electrical energy.

2.3 Power coefficient

The power coefficient C_p is defined by dividing the actual mechanical power P_m by the available wind power as can be seen in (5).

$$C_p = \frac{P_m}{P_{wind}} = \frac{P_m}{\frac{1}{2} A \rho_{air} V_\infty^3} \tag{5}$$

The amount of energy that can be extracted from an undisturbed wind stream flow is limited. This phenomenon is called the Betz coefficient which limits the maximum mechanical energy that can be converted from wind power by 59.3%[92].

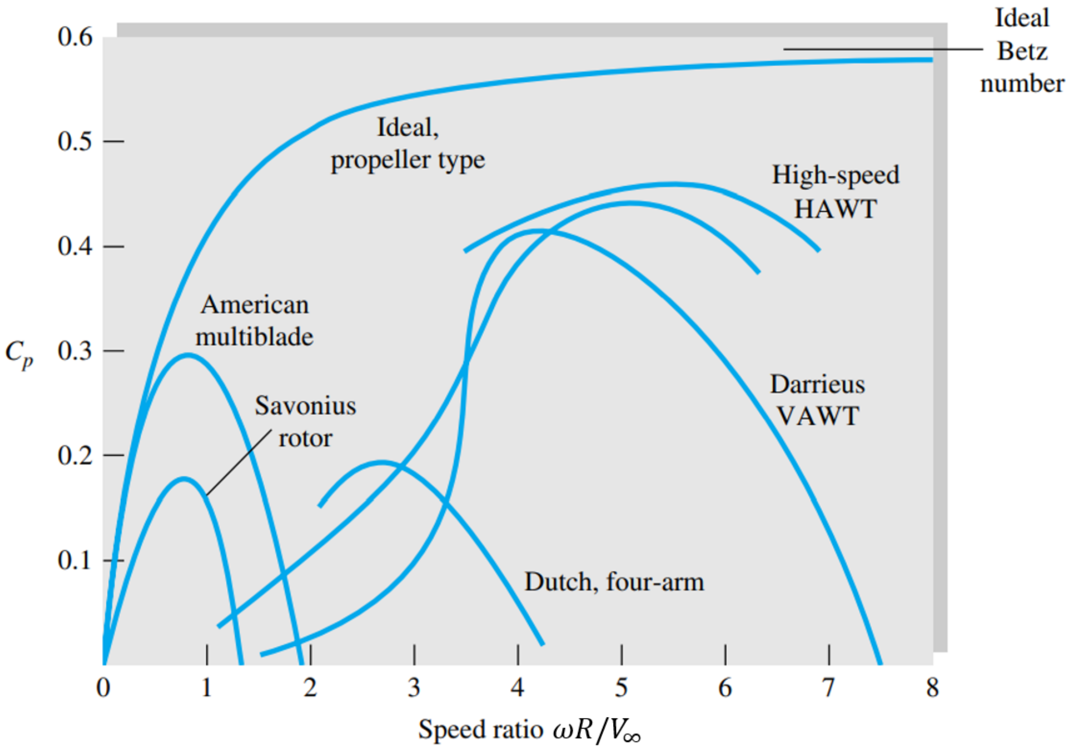

Figure 11: Power coefficient versus tip-speed ratio of various wind turbines[129]

Figure 11 shows the C_p of certain wind turbines versus the tip-speed ratio λ. The TSR is defined by (6), where ω is the angular velocity and R is the rotor radius.

$$\lambda = \frac{\omega R}{V_\infty} \tag{6}$$

2.4 History of the VAWT

Using wind as an energy source has been a challenge for many centuries. The VAWT that the Persians developed and built in the 10th century AD was used to automate irrigation and the grinding of grain[17][112]. This kind of vertical axis windmill, which is depicted in Fig. 12, is the first one known to be made by humanity. These windmills used drag forces as a consequence of the wind in order to be operational.

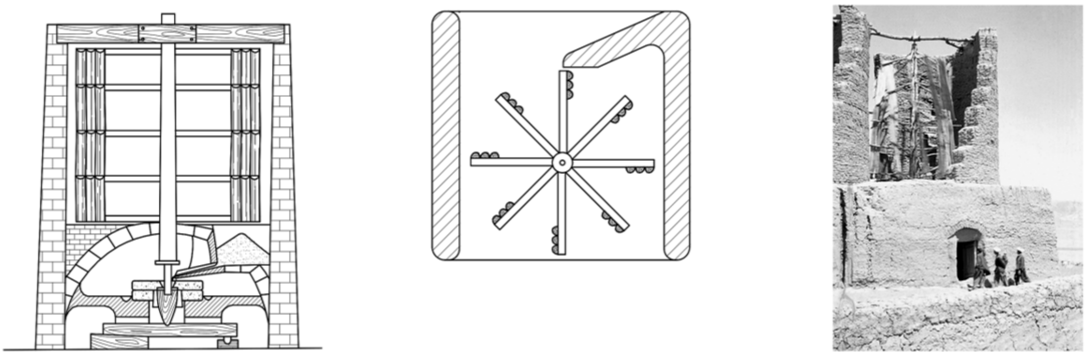
(a) Schematic front view (b) Schematic top view (c) Actual view

Figure 12: Persian windmill views[81]

The drag-type wind turbine as it is known today is called the Savonius wind turbine. This wind turbine, patented by Sigurd Johannes Savonius in 1926[58], does have low efficiency and operates at a TSR < 1[9]. The Savonius-type wind turbine suggested by Savonius is depicted in Fig. 13.

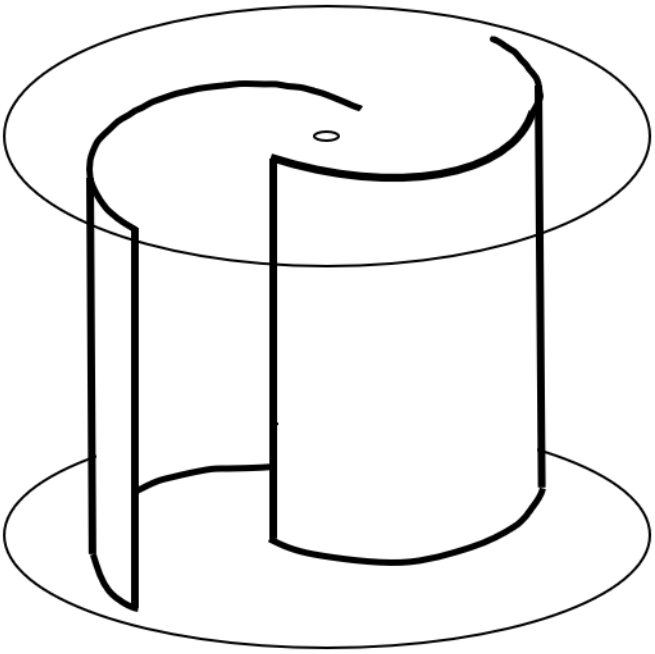

Figure 13: The Savonius type wind turbine suggested by Sigurd Johannes Savonius

Wind turbine development progressed steadily for nearly the entire 20th century, owing primarily due to advances in scientific understanding of aerodynamic lift from the aircraft industry[112]. The first lift-driven VAWT, which consisted of vertically orientated airfoil-shaped blades rotating around an axis orthogonal to the flow direction, was patented in 1931 by French aeronautical and military engineer Georges Jean Marie Darrieus[44]. The patent is shown in Fig. 14.

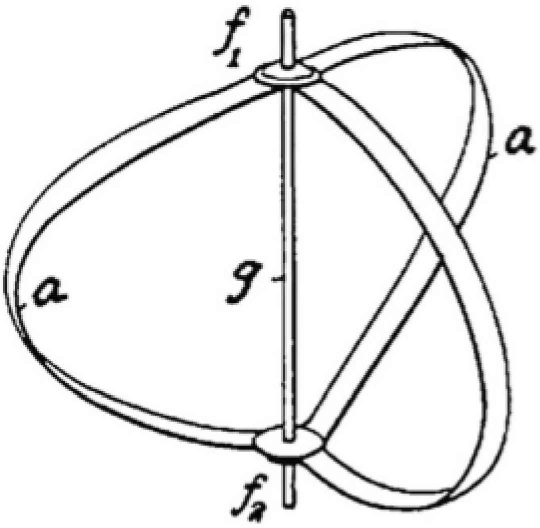

Figure 14: Darrieus's patent displaying the curved bladed wind turbine with explanations (a) blade (f_1) top hub (f_2) bottom hub (g) shaft[28]

The design principle of this curved-bladed VAWT is that the blades are formed in a Troposkein shape which has the advantage of reducing the stress in the blades[14][18]. This curved-bladed VAWT design gained more recognition after the Arab oil embargo in 1973[112] because alternative energy sources were in demand[112]. In 1988, Canada was the first country to take this design to greater heights which resulted in the world's largest VAWT that was ever built, as shown in Fig. 15. The VAWT has a swept area of 4000 m^2 with a height of 110m and a 64m diameter. The structure weighs 880 tonnes and provides a power output of 3.8 MW[108].

Figure 15: Éole, the world's largest VAWT[130]

But after this period, the interests began to move from the VAWT to the HAWT because the HAWT was regarded as the better option of the two[115]. This is also visualised in Fig. 16 as in the period between 1990 and 2005 when the publications concerning VAWTs somehow stagnated.

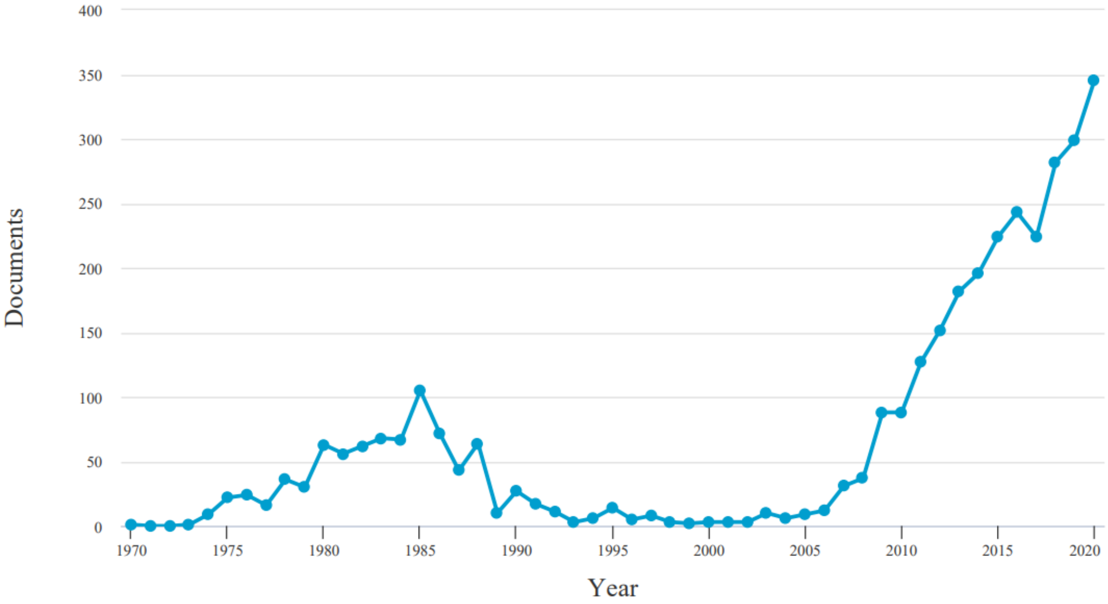

Figure 16: Published documents on the topic of VAWTs (data obtained from Scopus, keywords: Vertical axis wind turbine)

However, the little attention that the VAWT received between 1990 and 2005 resulted that small-scale VAWTs (< 10kW) being a great candidate for suburban and peri-urban areas[53][84]. Furthermore, the VAWT excels in these areas due to the fact it even performs in the highly unstable skewed wind flows and there is a low noise production because of the low TSR[72][80]. Therefore, renewed interests in scientific undertakings with respect to VAWTs followed from 2005 and on.

2.5 The state of the art VAWT

As of today VAWT technology is still gaining popularity as a result of its unique characteristics and applications. As mentioned before the two main VAWT types are called Savonius and Darrieus which use drag and lift as their aerodynamic force, respectively.

2.5.1 Savonius VAWT

The Savonius VAWT has excellent self-starting capabilities at the expense of operating at a low range of TSR and has low efficiency. However, its greatest advantage is the simplicity of the turbine, which results in high reliability[111]. A variant of the Savonius VAWT compared to the conventional one is that the Savonius turbine has a helical geometry as is depicted in Fig. 17.

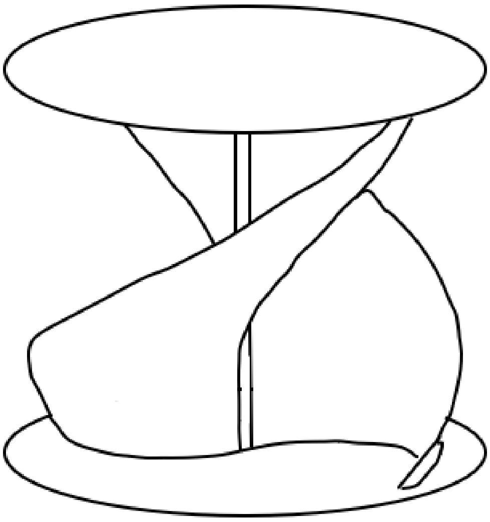

Figure 17: Schematic of a Savonius VAWT with a helical geometry

The helical Savonius turbine performs better than the conventional design considering the stability of the generation of torque and the power coefficient[64][47]. However, due to the helical shape of the blades, the manufacturing process is more complex than that of the conventional blades. As a result of much interest in renewable energy technologies, the Savonius wind turbine is also able to contribute to this. For example, to be part of a 3-in-1 wind, solar and rain harvesting system[25] as is presented in Fig. 18. As mentioned before, the Savonius wind turbine operates at a TSR < 1 and has a maximum power coefficient of 0.15. Therefore, the Savonius wind turbine is not suited for a wide variety of applications.

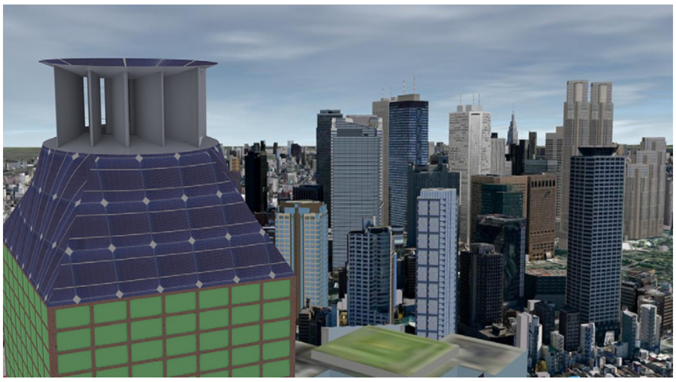

Figure 18: Savonius turbine as part of a hybrid renewable energy system[25]

2.5.2 Darrieus VAWT

The Darrieus type wind turbine on the other hand, has more variations when looking at the design. Besides the suggested curved-bladed VAWT by Georges Jean Marie Darrieus, the Darrieus VAWT also has a straight-bladed and a helical-bladed variant. These main three design options are presented in Fig. 19.

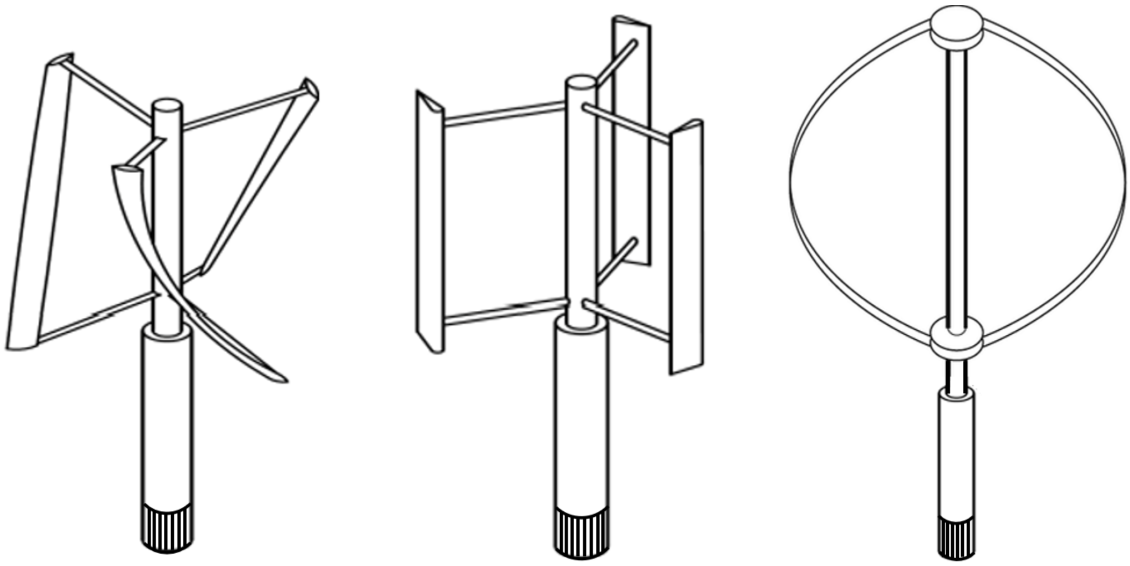

(a) Helical-bladed VAWT (b) Straight-bladed VAWT (c) Curved-bladed VAWT

Figure 19: The three main VAWT design variations

There are many different Darrieus VAWT configurations possible[86], but all have deviated from one of the three aforementioned types. A number of characteristics are compared between the three turbines and are presented in Table 2.

Table 2: VAWT configuration comparison[45]

Characteristic	**Helical-bladed**	**Straight-bladed**	**Curved-bladed**
Peak aerodynamic efficiency	**	****	***
Manufacturability and cost	*	****	**
Self-starting ability	****	**	*
Structural stress	**	*	***
Stall regulation control	*	***	*
Shaft torque ripple	***	*	*
Skewed inflow effect	Negative	Positive	Negative
Blade tip vortices created	Yes	Yes	No
Support struts required	Yes	Yes	Optional
Guy cables required	No	No	Yes

Note: A higher number of stars (*) is desirable.

It can be concluded that the SB-VAWT is generally the better option compared to the helical-bladed and the curved-bladed VAWT. From 2005, renewed interest in VAWTs resulted in new applications where the VAWT can be utilised. Offshore wind energy started to become popular in the 21st century. Usually, offshore HAWTs were installed due to their high power output. However, because the turbine of the HAWT is established far above the base structure, the construction, operation and maintenance costs prove to be challenging. This is even more true when operating offshore[8]. The VAWT on the other hand has its mechanisms installed at its base structure which is a huge advantage over the offshore HAWT. Besides the known disadvantages of the VAWT, the full potential of (offshore) VAWTs did not fully come into its own. This is because the HAWT enjoyed much more research and development as opposed to its vertical counterpart[59][36]. Nonetheless, due to the revival of VAWT technology, new concepts are evaluated as can be seen in Fig. 20 where conceptual designs for offshore purposes are depicted.

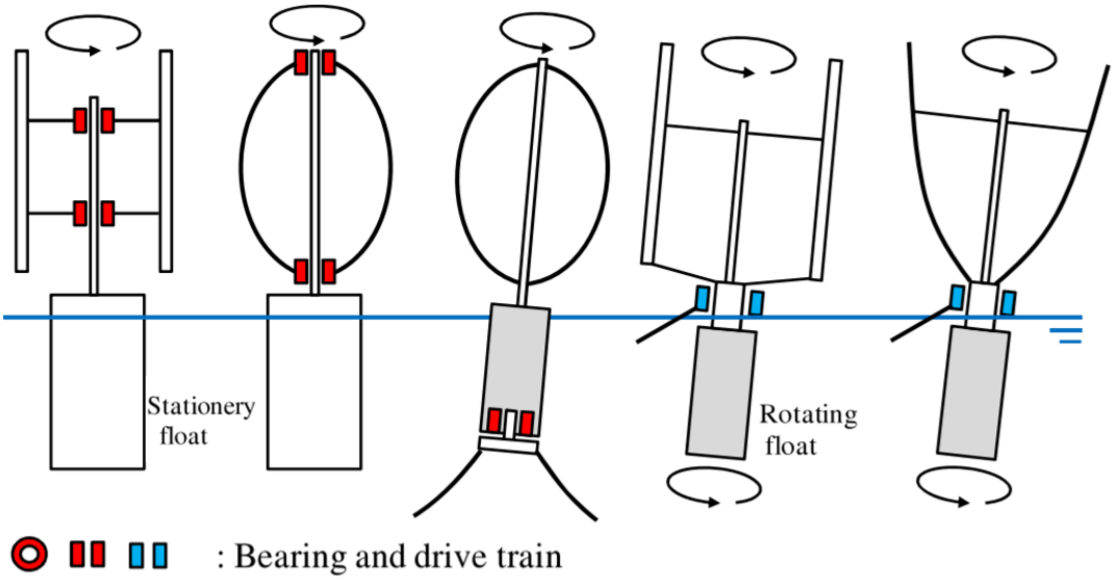

Figure 20: Conceptual designs of offshore VAWTs[8]

As of today, there are a few companies realising these offshore VAWTs. For example, in 2015 the Swedish company SeaTwirl managed to test their 30kW design which is shown in Fig. 21a. SeaTwirl is currently planning on the installation of an extensive S2x unit. This pilot installation should be finished in 2023 and will provide 1 MW[105]. The S2x VAWT is suited for locations such as wind farms, remote places and fish farms.

Another project suggested by the company Wind Power Ltd is the Aerogenerator X, illustrated in Fig. 21b. This 10 MW VAWT is generally half the height of a conventional HAWT. Due to the fact that the drivetrain of the Aerogenerator X is located at its base, the centre of gravity lies low which results in greater robustness during strong winds as opposed to HAWTs[114].

The company VertAx Wind Ltd proposed a design, seen in Fig. 21c, which is in an advanced stage. Since 2004 many prototypes have been built and tested from 15 kW up to 1 MW. According to the models, the VAWT is also expected to achieve an even higher power output of 6 MW[1]. What makes this design even more interesting, is the C-Gen technology[63]. The suggested innovation from VertAx Wind Ltd in collaboration with the University of Edinburg results in zero cogging torque. This technology massively improves the starting capabilities of the VAWT which results in enhanced annual energy production[79]. As of May 2021, VertAx Wind Ltd is still occupied with the goal of ultimately installing its large-scale offshore VAWT farm[124].

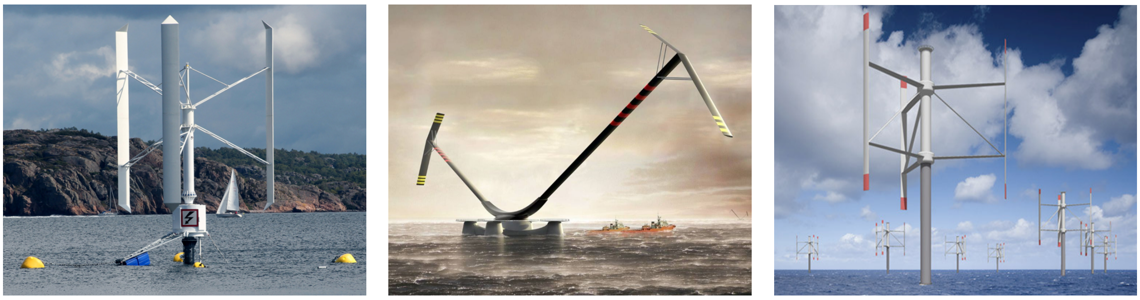

(a) S2x[105] (b) Aerogenerator X[6] (c) VertAx[1]

Figure 21: Three offshore VAWT projects currently in progress

Another unique application of the VAWT is using the wakes generated by vehicles on the highway for producing energy. Although the power coefficient peaks at 0.00464, it is still able to have a power output of 139.60 W per VAWT[121]. As can be seen in Fig. 22, the VAWT is placed at the central reservation in order to be subjected to both car lanes. This setup also benefits the power output if there much traffic without congestion.

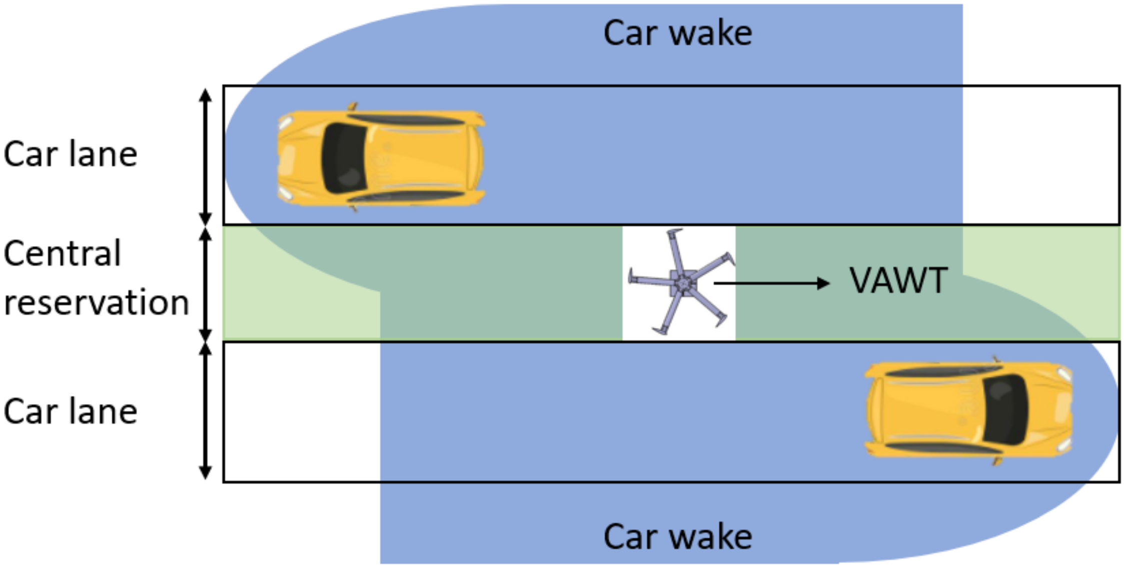

Figure 22: Schematic of a VAWT placed at the highway

Even more interesting is the possibility that the VAWT might thrive on another planet. The fact that Mars contains high wind speeds and a thin atmosphere results in quite low Reynolds numbers varying from 5000 to 80000. Therefore, the airfoils of a VAWT experience either a laminar or transitional flow. A SB-VAWT with a power output of 500 W, suggested by[65], has been considered for this scenario. On top of this, lightweight designs should be considered because of the circumstances on Mars[118]. An idea of how VAWTs are integrated on Mars is depicted in Fig. 23.

Figure 23: Illustration of a straight-bladed (left) and a curved-blades (right) VAWT on Mars

CHAPTER 3

Design methodology

The overview of the design methodology is presented in Fig. 24. The design methodology is partly inspired by the Delft design guide[123].

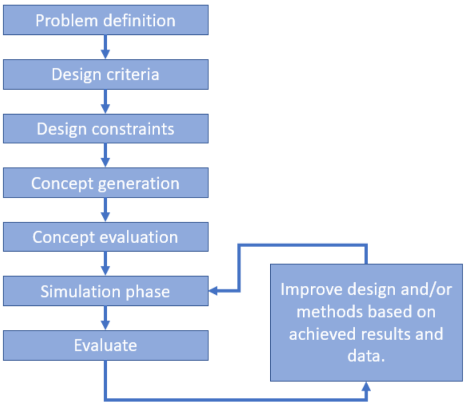

Figure 24: Design methodology

3.1 Design criteria

First of all, the design criteria are defined. The following design criteria of the power unit have to be met:

- Actuation integration
- Adaptive to wind (and solar) circumstances

3.2 Design constraints

Each design constraint will be analysed in order to support future design approaches.

- Geometry
- Viable performance model
- Availability
- Testability

3.2.1 Geometry

The height and the width of the system is limited due to the fact one should be able to test the design in a wind tunnel. Moreover, limiting the size will also reduce the costs in order to make a prototype. Last but not least, by limiting the dimensions, the building time reduces which is another advantage for creating spare parts or adjusting parts. The open jet facility (OJF) at the TU Delft provides a test section of 2.85m by 2.85m. In order to compensate for the blockage effect[57], the front area of the hybrid power unit should not exceed 5% of the cross-section of the test section[117] which is approximately 0.4 m^2.

3.2.2 Viable performance model

With the aim of predicting the performance of the VAWT, a feasible performance model should be selected. For analysing the performance of a VAWT, three models are generally used:

- Momentum-based models
- Vortex-based models
- Viscous-based models - Computational Fluid Dynamics (CFD)

Momentum-based models Momentum-based models used for the VAWT have evolved over time. Back in 1878, W. Froude suggested the blade element theory (BET) which is a mathematical procedure in order to discover the behaviour of propellers[38]. It entails dismantling a blade into several small components and calculating the forces acting on each of these small blade elements. The downside of this theory is the modelling of the induced velocity.

Because of this, the actuator disk theory of W. Rankine[93], introduced in 1865, is used to overcome this issue. The actuator disk theory implies that the rotor acts like an infinitely thin disk. Due to the undisturbed wind stream which flows around the disk, a mathematical derivation can be made. A correlation between the power output, torque, induced velocity and radius of the rotor can be found using this theory.

In 1926, H. Glauert combined the two aforementioned theories into the blade element momentum (BEM) theory[40]. The BEM theory was able to determine the local forces acting on the blade, as well as calculate the induced velocities at the blade.

It was not until 1974 when R. Templin suggested the first performance model specialised for VAWTs, Namely the single-stream tube (SST) model[119]. The SST model entails that the whole VAWT is surrounded by a single-stream tube. The flow velocity is assumed to be constant on both the downstream and upstream sides of the swept area.

A year later the SST model was improved by J. Strickland in 1975. Instead of using only one stream tube for the turbine, multiple stream tubes are considered in his suggested multiple-stream-tube (MST) model[113]. For each stream tube, the BEM theory is applied.

One of the main issues with the MST model is the fact it does not differentiate between the upwind zone and the downwind zone[78]. In 1986, B. Newman invented the double actuator disk theory[82]. By using two interference factors in this theory it is possible to calculate every velocity for every zone.

Then, in 1986, M. Paraschivoiu managed to combine the double actuator disk theory with the MST model. This results in the double multiple stream tube (DMST) model[88]. The predecessors, the SST model and MST model of the DMST model, were both not able to determine how the velocity in the upwind zone is influencing the downwind zone. The DMST model provides the solution for each individual wind zone.

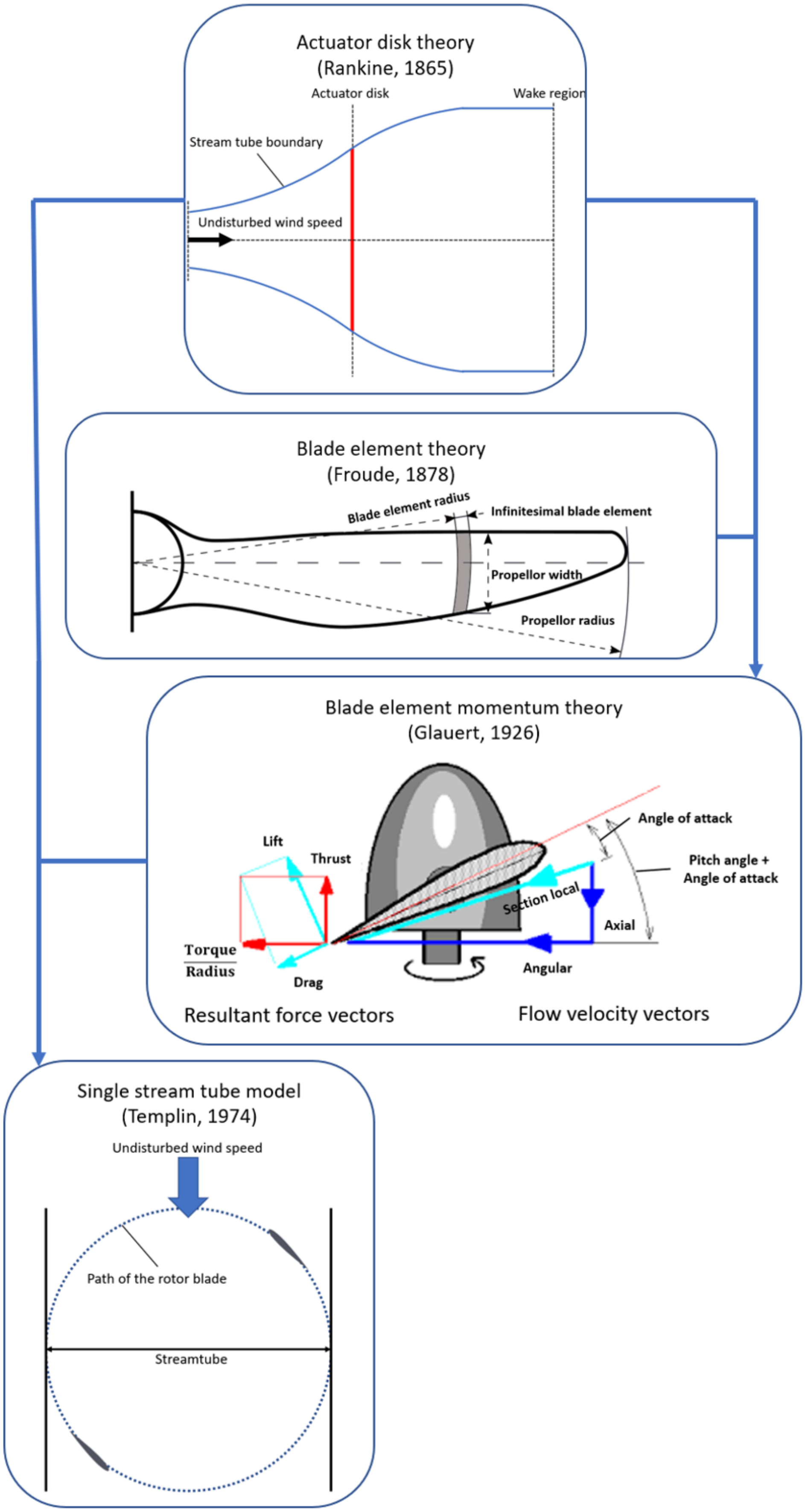

Figure 25: Evolution of momentum-based models until 1974

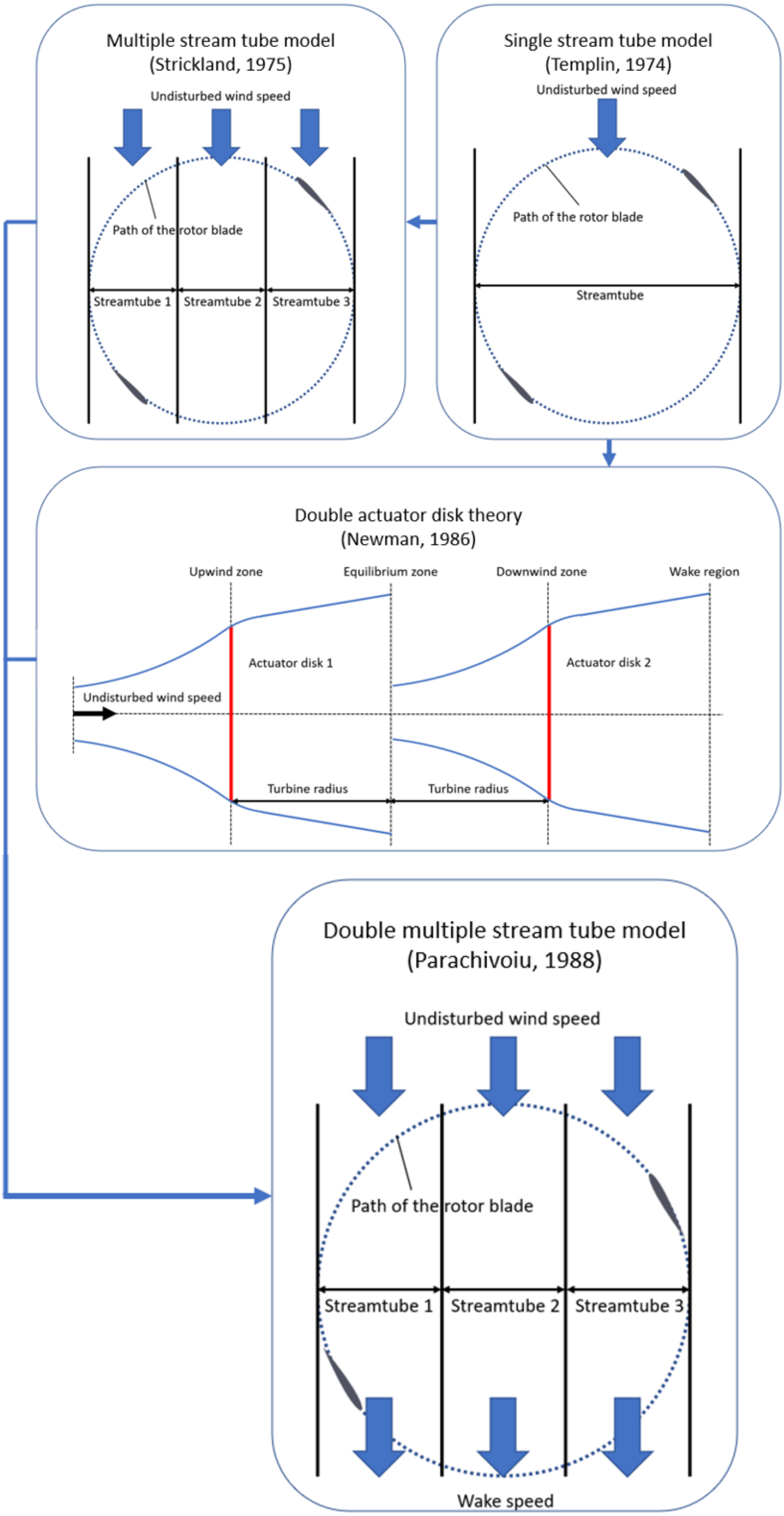

Figure 26: Evolution of momentum-based models from 1974 until 1988

Vortex-based models One of the key characteristics of vortex-based models is that they assume that the airflow in the wake is a potential flow[106]. The influence of vorticity which is present in the wake of the rotor blades is used in order to determine the velocity fields. Fig 27 presents a schematic of the vortex based model.

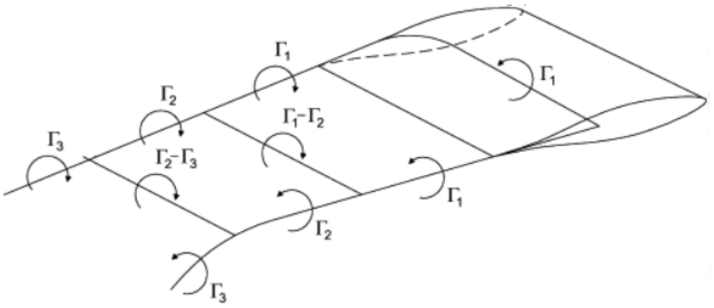

Figure 27: Vortex model schematic with vortex strength Γ for a rotor blade element[56]

Viscous-based models Viscous-based models present in the CFD domain exist out of turbulence modelling. Fig. 28 shows the available models in ANSYS Fluent[75], a prominent fluid simulation software. The Reynolds Averaged Navier-Stokes (RANS) based models are very popular and generally preferred in the industry due to their robustness[74]. Especially the standard $k-\epsilon$ model is an extensively used model for industrial applications because of its adequate accuracy for a wide range of flows[126][70]. The standard $k-\epsilon$ model is the most widely-used engineering turbulence model for industrial applications because of its robustness and reasonable accuracy for a wide range of flows.

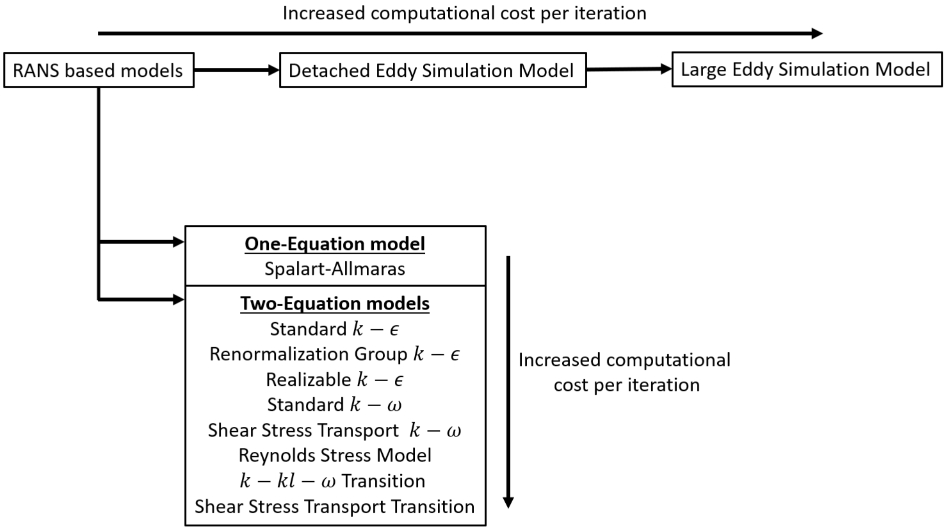

Figure 28: Turbulence models available in ANSYS Fluent

The advantages and disadvantages of the various models are presented in Table 3.

3.2.3 Availability

All the components, materials, software and hardware are essential for making the design. The TU Delft is able to provide most of the aforementioned and everything needed outside the TU Delft should also be available in a relatively short term.

3.2.4 Testability

As mentioned before, the VAWT part of the system should be tested in the open jet facility. Besides that, sensors and software are required to analyse the test results.

	Momentum-based model[19]	Vortex-based model[54]	Viscous-based model[10]
Advantages	• Obtains fast qualitative results. • Fast computation time.	• Able to accurately predict near wake velocities for more precise simulations.	• Able to compare results with experimental data. • Capable of working with different turbine solidities along with different tip-speed ratios.
Disadvantages	• Limited to solidities below 0.2. • The algorithm is not accurate for small. wind turbines at small tip speed ratios. • Neglects dynamic stall. • Neglects effect of wake interaction. • 1D simplification causes inaccuracies by neglecting span-wise velocity and 3D effects on the blade • Considers the flow as homogeneous, incompressible, steady-state flow; no frictional drag or non-rotating wake.	• High computational time • Assumes potential flow	• Additional turbulence modelling may be required to capture unsteady effects. • Computational domain is often required. • Can be computationally expensive.

Table 3: Advantages and disadvantages of momentum, vortex and viscous-based models

3.3 VAWT design parameters

3.3.1 Tip speed ratio

Recall from (6) that the TSR depends on the rotor radius, the angular velocity of the blades and the undisturbed wind stream. When the angular velocity is getting too small, the wind passes through the swept area of the turbine without affecting the blades in order to make the turbine rotate. On the other hand, if the angular velocity is too high, the rotating blades are blocking the wind flow. This results in a reduced power extraction from the wind. Also, each turbine has its optimal TSR where the power coefficient is at its maximum[91].

3.3.2 Swept area

The swept area of a wind turbine describes the area where the wind is directly passing through. The power output of a wind turbine is directly related to the swept area of the rotor blades. The swept area of a SB-VAWT is given by (7).

$$A = DH \tag{7}$$

As one can see in Fig. 29, the rotor diameter and the blade height are given by D and H, respectively. As the diameter increases, wind turbines need to be able to endure higher levels of centrifugal forces. Also, bending moments are increased across the swept area of the turbine.

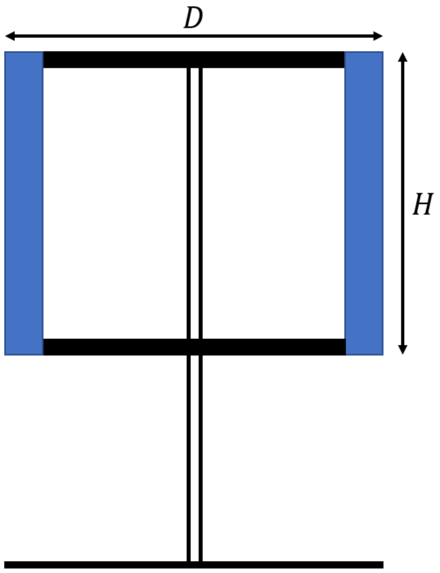

Figure 29: Swept area of a VAWT

3.3.3 Aspect ratio

The aspect ratio A_r defines the ratio between the blade height and the rotor radius is shown in (8).

$$A_r = \frac{H}{D} = \frac{H}{2R} \tag{8}$$

A lower AR results in a higher Reynolds number at the blades[20]. The local Reynolds number Re_c of a turbine blade is given by (9), where c is the chord length, W the relative wind velocity and ν the kinematic viscosity of the air.

$$Re_c = \frac{cW}{\nu} \tag{9}$$

Also, the lower the AR, the lower the rotation per minute (rpm) of the VAWT is due to the fact that the moment of inertia increases while the radius increases. Two VAWTs with the same swept area but with different AR are depicted in Fig. 30.

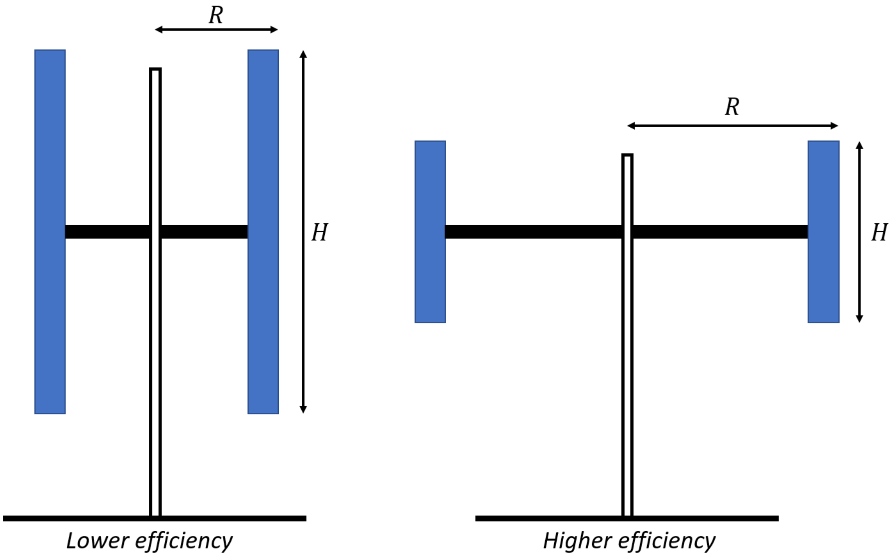

Figure 30: Two VAWTs with the same swept area but a different aspect ratio

3.3.4 Strut-blade ratio and configuration

The number of struts connected to a wind turbine blade and the way the struts are arranged has an impact on how the VAWT performs. The arrangement where the struts are perpendicular to the tower and the blades is presented in Fig. 31a. This configuration has the advantage that the only two forces that are transferred through the strut are compression and tension. The other configuration, depicted in Fig. 31b, has the struts arranged at an angle which results in an extra bending moment at the tower of the VAWT. However, placing the struts at an angle leads to a lower centre of gravity and a reduction of the tower size. The most important difference between the two configurations is that horizontal struts have a T-joint for connecting the strut to the tower and the blades which results in less interference drag than when that is not the case[46][32].


(a)

(b)

Figure 31: **(a)** Struts connected perpendicular to the tower and blades with the bending moment graph shown **(b)** Struts connected at an angle to the tower and blades with the bending moment graph shown.

Another important aspect to consider is how many struts are used to support a blade. For straight blades VAWTs there are three common support strut configurations which are presented in Fig. 32. Both the squared-supported and the overhang-supported configurations generate more parasitic drag than the cantilever-supported configuration due to the fact more struts generate more parasitic drag[55]. However, opting for the cantilever-support results in higher bending moments across the rotor blade. The placement of the support struts has a huge influence on the bending moment acting on the rotor blade. To minimise the bending moment across the rotor blade, the struts should be placed at 21% from the length of the rotor blade with respect to each of the blade tips[7][43].

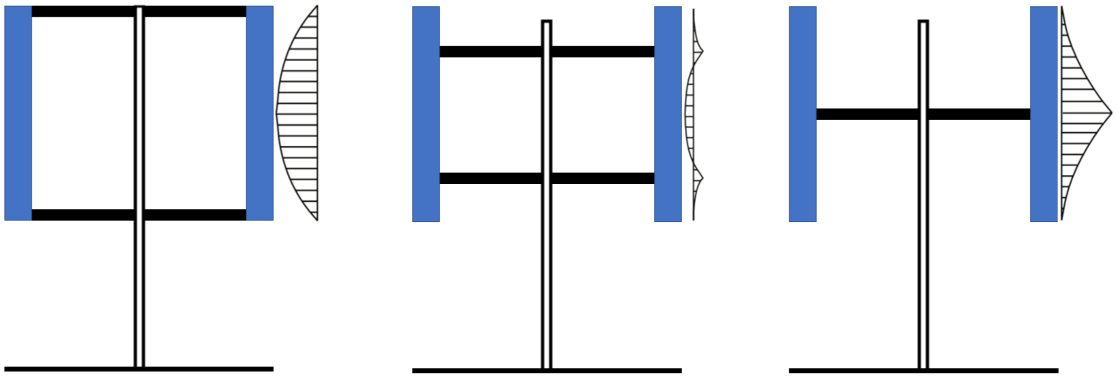
(a) Squared-supported

(b) Overhang-supported

(c) Cantilever-supported

Figure 32: Three different support strut configurations with their representative bending moment graphs.

3.3.5 Turbine solidity

The solidity of a wind turbine is defined by dividing the total area of all rotor blades by the swept area. For a Darrieus type VAWT, the solidity S is described by (10), where N is the number of blades.

$$S = \frac{NcH}{DH} = \frac{Nc}{D} = \frac{Nc}{2R} \tag{10}$$

Increasing the solidity of a VAWT increases the self-starting capability but at the expense of operating in a rather wide range of TSR. Additionally, the peak of the power coefficient is less than when the solidity is lower[76]. Low solidity is therefore not desirable when one wants to avoid low torque due to early stalling low lift[33]. For design purposes, the TSR is of great importance and is also dependent on solidity. Because of this, a thorough study has been executed and finds a new correlation between the optimal TSR λ_{opt} and solidity[95] which is given by (11). For medium to low wind speed conditions, it is a viable tool for wind turbine design purposes.

$$\lambda_{opt} = 2.693S^{-0.329} - 1.605 \tag{11}$$

Hence, a trade-off has to be made when solidity is considered as low solidity gives a lower coefficient of power over a large TSR range whereas high solidity results in a higher coefficient of power in a shorter range of TSR. Also, the number of blades should not be too large as it results in a largely dispersed wake which is unsuitable for deploying multiple VAWTs together[90].

3.3.6 Airfoil type

The airfoil type of the rotor blades is generally defined by the standard of the National Advisory Committee for Aeronautics (NACA). These so-called NACA airfoils have been thoroughly tested and because of that, a numerical designation for each type of airfoil has been formulated[2]. Each type of airfoil is defined by NACA followed by 4 digits:

- The first digit is the percentage of the maximum camber of the chord length.
- The second digit is the location of the maximum camber divided by ten.
- The last two digits display the maximum thickness as a percentage of the total chord length.

For example. Fig. 33 contains the plot of a NACA 2412 airfoil. Therefore, the maximum camber is 2% which is located at $x = 0.4$ due to the second digit. The last two digits display the maximum thickness of the chord which is 12% of 1.

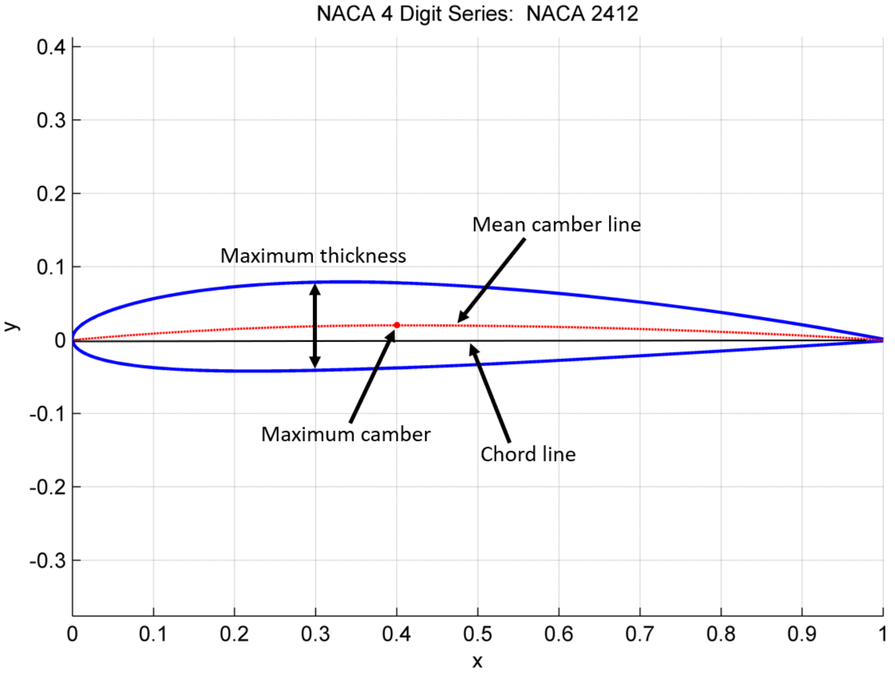

Figure 33: Plot of the asymmetrical airfoil NACA2412

These geometrical features have a significant influence on the performance of the VAWT. Lift, drag and the stall angle depend on the thickness and camber of the airfoil, excluding Reynolds number[71]. Additionally, the location of the maximum camber and thickness of the airfoil also contribute to its performance. For increased self-starting capabilities, opting for an asymmetrical airfoil over a symmetrical airfoil proves to be desirable[73][49]. On the other hand, when considering only symmetrical airfoils, the most promising airfoil starting at low wind speed is the NACA 0021[83][109]. Especially when TSR < 3, NACA 0021 should be chosen[27] whereas TSR > 5 a lower thickness for a symmetrical airfoil should be preferred[99].

3.3.7 Pitch angle

Recall that ϕ is the angle between the relative wind velocity and the tangential velocity of the rotor blade. Furthermore, both the angle of attack (AoA) and relative wind velocity are a function of the azimuth angle θ which vary as the blades are rotating. When the rotor blades are fixed, then the AoA is equal to ϕ, but not when a pitch angle β is introduced as can be seen in Fig. 34.

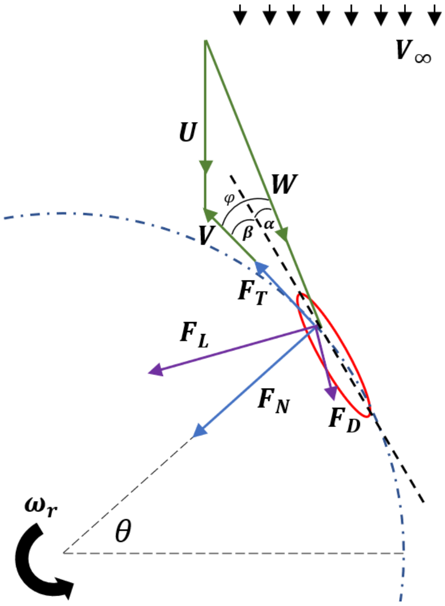

Figure 34: Forces and velocities acting on an outward pitched rotor blade

When a blade points outwards (toe-out) with respect to its trajectory, there is a negative pitch angle. The pitch angle is positive when it points inwards (toe-in) with respect to its trajectory. The toe-out, fixed and toe-in positions of the rotor blade are depicted in Fig. 35.

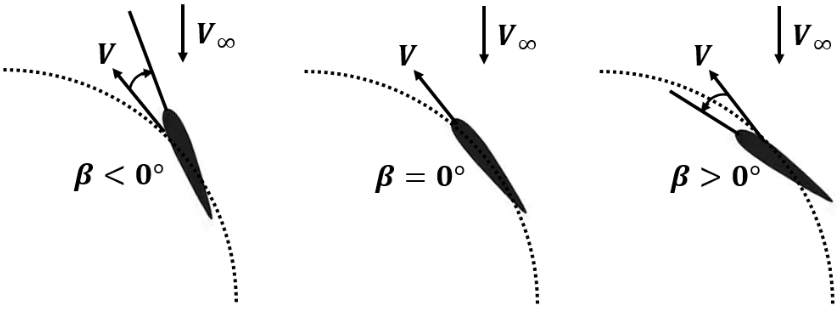

Figure 35: Three different possible pitch angles

Thus, the pitch angle is given by (12). Needless to say, the pitch angle influences the power coefficient positively and negatively depending if the rotor blade is in an upwind or downwind region.

$$\beta = \alpha - \phi \tag{12}$$

Moreover, the AoA is dependent on the TSR and the azimuth angle as is shown by (13) in the case of a fixed blade ($\beta = 0°$).

$$\alpha = tan^{-1}\left(\frac{cos(\theta)}{sin(\theta) + \lambda}\right) \tag{13}$$

Adjusting the pitch angle for every AoA proves to be complex for modelling, controlling and manufacturing[4]. However, pitch control systems improve self-starting capabilities, better efficiency and increased range of operations[66][42]. If a small but fixed negative pitch angle is chosen for every AoA, the VAWT performs better or worse depending on upwind and downwind regions. Yet the turbine performs better than when the pitch angle is zero[94][24][23].

3.4 Key performance indicators

A key performance indicator (KPI) of the VAWT defines how well the VAWT performs in a certain area. Four KPIs for the VAWT are defined.

3.4.1 Operational range

Provided that the wind speed strongly varies, the VAWT should be operational in a wide range of TSR while avoiding the power coefficient to drop too sharply before it reaches zero. In order to operate at a wide variety of wind speeds, the starting torque of the turbine should be minimised. Adjusting the mass moment of inertia of a VAWT does not have a noticeable effect on the starting torque and its final speed[21]. Thus, the torque coefficient, should be as high as possible. Furthermore, increasing λ_{max} also results in a higher operational range.

3.4.2 Peak efficiency

While limited by the number of Betz, the power coefficient determines the ratio of how much electrical power actually is produced divided by the total wind power that is generated by the wind turbine. The peak of the power coefficient takes place at the optimum tip-speed ratio λ_{opt}.

3.4.3 Average power coefficient

The average power coefficient C_{apc} is found by (14), which indicates the best overall performance of the VAWT.

$$C_{apc} = \frac{\int_0^{\lambda_{max}} C_p(\lambda)\, d\lambda}{\lambda_{max}} \tag{14}$$

The maximum TSR λ_{max} is where the wind turbine is still able to generate power which is clarified in Fig. 36 together with the APC curve.

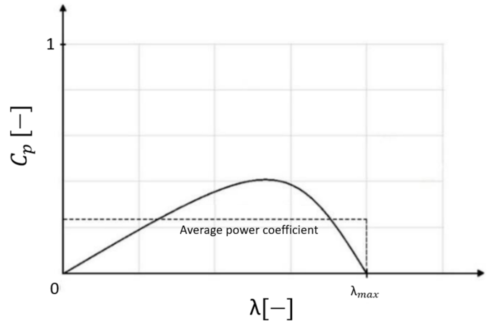

Figure 36: Example of a $C_p(\lambda)$ diagram with the average power coefficient

3.4.4 Absolute power output

The last KPI is the absolute power output of the VAWT. For example, a VAWT might have a higher peak efficiency but a lower absolute power output. One might opt for a VAWT which has a higher absolute power output and a lower peak efficiency depending on the situation.

3.4.5 Key performance indicator analysis

There are many factors which influences the KPIs. For the SB-VAWT, many technical adjustments or design aspects have an impact on certain aforementioned KPIs. A summary of which technical adjustment or design aspect influences the KPIs of the SB-VAWT is given in Table 4

Strategy	Operational range	Peak efficiency	Average power coefficient	Absolute power output	source
Gurney flap	+	+	+	+	[134]
Linkage system		+	+	+	[26]
J-shaped airfoil	-	+			[22]
Increased solidity	-	+			[103]
Decreased solidity	+	-			[103]

Table 4: Effects on key performance indicators

Furthermore, the airfoil could be asymmetrical or symmetrical. Moreover, the thickness of the airfoil can be increased or decreased. The geometry of the airfoil does have an impact on the $C_p(\lambda)$ curve as is shown in Fig. 37. Overall the airfoil should not be too thick and making it asymmetrical does not result in huge changes when the two first digits are kept between 00 and 65. High digit symmetrical NACA00xx airfoils manage produce a high power output in low speed zones (TSR<3) whereas low-digit symmetrical NACA00xx airfoils produces a higher power output in a high speed range (TSR>5)[99].

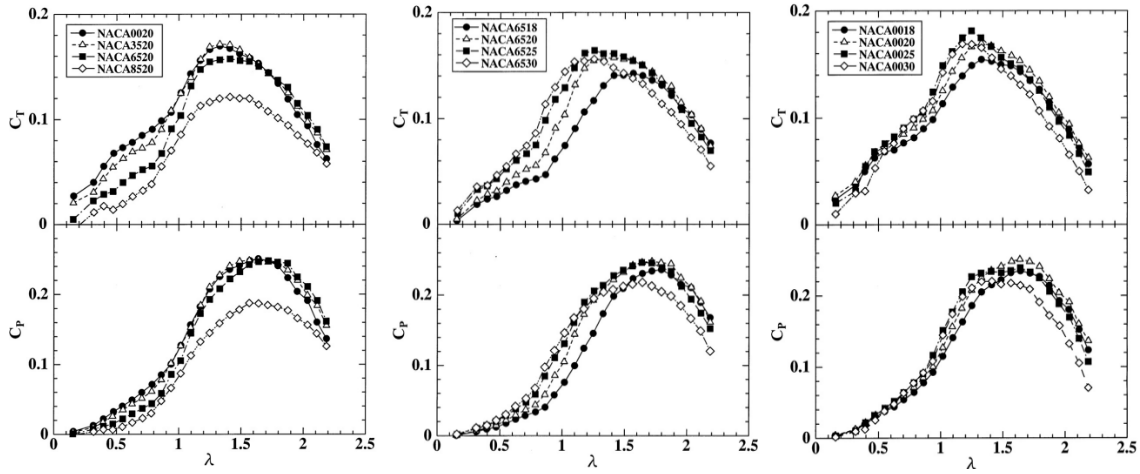

Figure 37: Airfoil geometry effects on the coefficient of power and the coefficient of torque[131]

3.5 Concept generation

To develop conceptual designs, a morphological chart has been made. Moreover, the coordinate system used for the concepts is elucidated in Fig. 38.

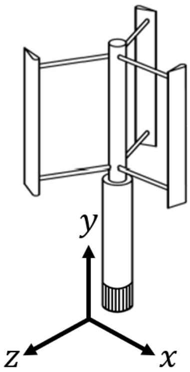

Figure 38: Coordinate system adopted for the conceptual designs

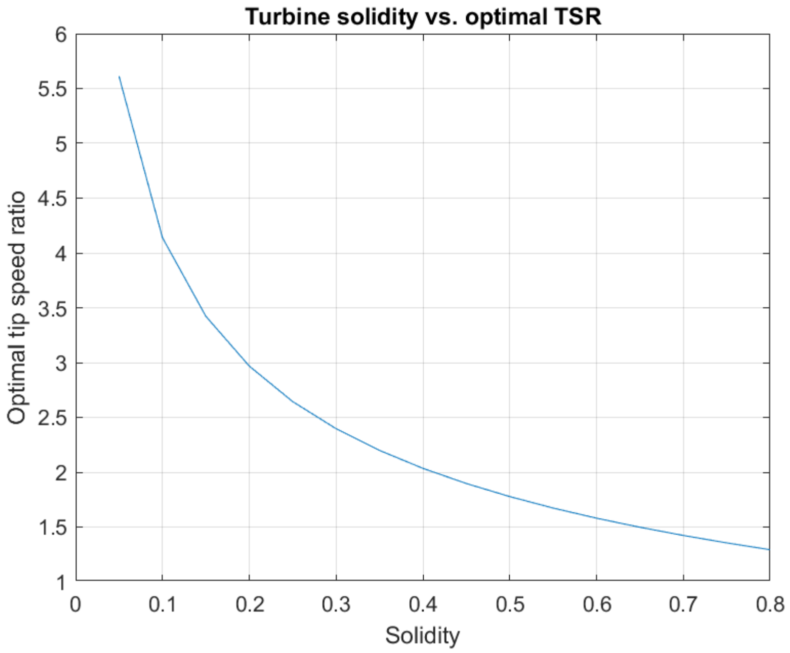

Figure 39: Turbine solidity vs. optimal tip-speed ratio

Certain design parameters are fixed due to design constraints or are left out because it has already been confirmed which option is more suitable. For appropriate testing conditions, the swept area is constrained by approximately $0.4m^2$. Hence the maximum width is set by $0.6m$ and also the height is limited by $0.6m$. Furthermore, (8) shows that a lower A_r is desirable. Therefore, every design has a fixed AR. This fixed A_r of 1.5 is the quotient of $0.4m$ blade height and $0.6m$ rotor radius. The morphological chart with its functions and options is presented in Table 5. Moreover,

Table 5: Morphological chart for the adaptive smart material system

Function	Option 1	Option 2	Option 3	Option 4
Number of rotor blades	2	3	4	
Strut-blade ratio	1	2		
Turbine solidity	Average ($S = 0.5$)	High ($S = 0.8$)		
SMA actuation	Rotor blade rotates around x- or z-axis	Rotor blade rotates around y-axis		
NACA airfoil geometry	Symmetrical 00xx	Asymmetrical 24xx	Asymmetrical 44xx	
NACA airfoil chord thickness	xx18	xx21		
Solar panel structure	Fixed	Flexible		
Solar panel tracking method	Chronological	Active	Manual	None

By using the morphological chart, five concepts will be generated and discussed. All concepts are constructed in the 3D computer-aided design (CAD) software programme SolidWorks. Furthermore, recall that there is a relation between the optimal TSR and turbine solidity which is given by (11). This is also shown in Fig. 39 The morphological chart contains three fixed values for the solidity. With the solidity as a function of the optimal TSR, the chord length of each rotor blade can be calculated for every concept. This is true because (10) shows that the only variable that is not present in the morphological chart or held as a constant, is the chord length.

3.5.1 Concept 1

The first concept will be explained in more detail as it contains similar characteristics which other concepts also possess. First of all, the gearbox and the generator of the VAWT are integrated within the cube. The fixed solar panel is positioned on top of the structure and is chronologically actuated. The chronological single-axis tracking method results in an improved efficiency of the solar panel up to 25%[100]. The visual representation of the first concept is presented in Fig. 40 whereas its functions and options are shown in Table 6.

Table 6: Functions and options regarding concept 1

Function	Option
Number of rotor blades	2
Strut-blade ratio	1
Turbine solidity	Average ($S = 0.5$)
SMA actuation	Rotor blade rotates around y-axis
NACA airfoil geometry	Symmetrical 00xx
NACA airfoil chord thickness	xx18
Solar panel structure	Fixed
Solar panel tracking method	Chronological

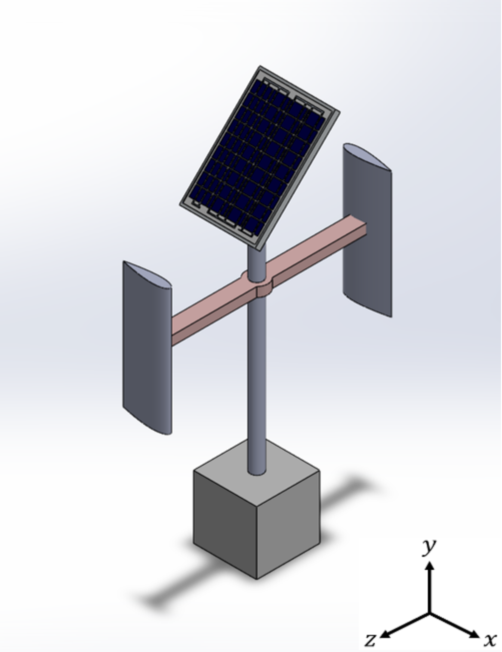

Figure 40: Concept 1

Furthermore, the SMA actuation for the first concept implies that the rotor blades rotate around the $y-$axis. Fig. 41 shows two scenarios of the top view of the first concept. When the wind direction is known, the rotor blade which receives the wind in the upwind region points outward whereas the rotor blade in the downwind region points inwards. This is made possible due to initiating SMA actuation which are located on the struts.

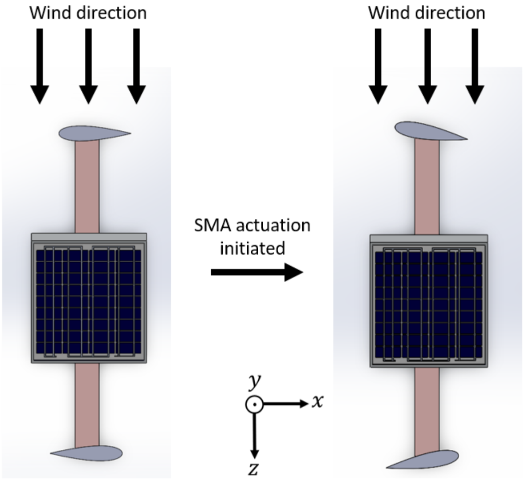

Figure 41: Top view of the neutral position and with the SMA actuation initiated

3.5.2 Concept 2

The characteristics of the second concept are shown in Table 7 and the CAD model itself is presented in Fig. 42. The second concept has a fixed solar panel, which is locked to the rod. Each rotor blade at both ends of the support strut is divided into two parts. The two parts are connected to a rotary SMA actuator.

Table 7: Functions and options regarding concept 2

Function	Option
Number of rotor blades	2
Strut-blade ratio	1
Turbine solidity	Average ($S = 0.5$)
SMA actuation	Rotor blade rotates around x- or z-axis
NACA airfoil geometry	Symmetrical 00xx
NACA airfoil chord thickness	xx21
Solar panel structure	Fixed
Solar panel tracking method	None

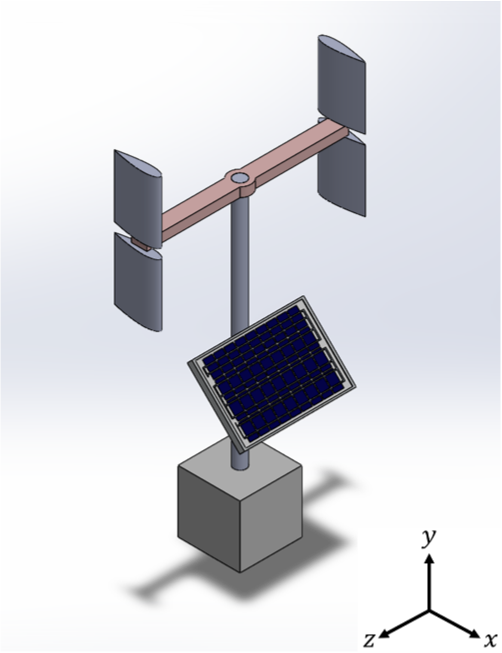

Figure 42: Concept 2

If SMA actuation is established, the rotor blades are rotating outward with respect to the support strut as can be seen in Fig. 43. This arrangement increases the self-starting capabilities[5].

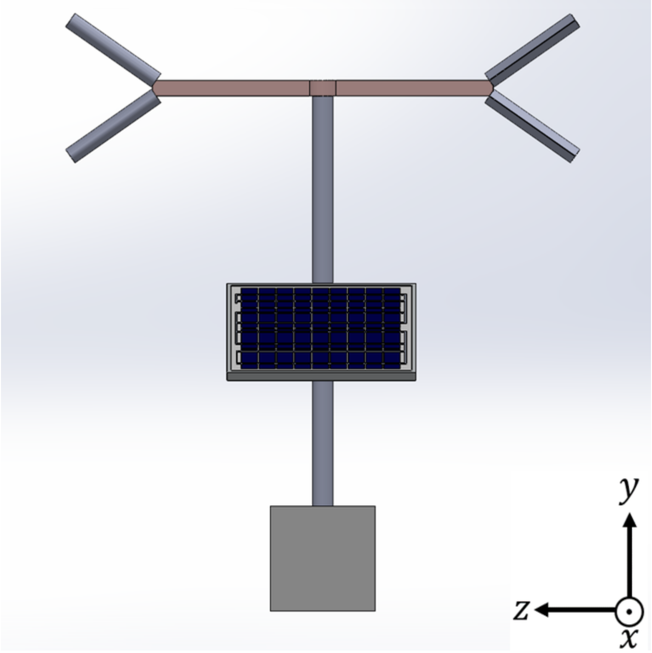

Figure 43: Front view of concept 2

3.5.3 Concept 3

As can be seen in Fig. 44 and Table 8, the turbine exists out of four rotor blades supported by two struts. The dual solar panels contain LDR sensors to make active solar tracking possible. Moreover, the same method of SMA actuating is present here regarding the first concept. However, this concept has two additional rotor blades.

Table 8: Functions and options regarding concept 3

Function	Option
Number of rotor blades	4
Strut-blade ratio	2
Turbine solidity	High ($S = 0.8$)
SMA actuation	Rotor blade rotates around y-axis
NACA airfoil geometry	Asymmetrical 44xx
NACA airfoil chord thickness	xx15
Solar panel structure	Fixed
Solar panel tracking method	Active

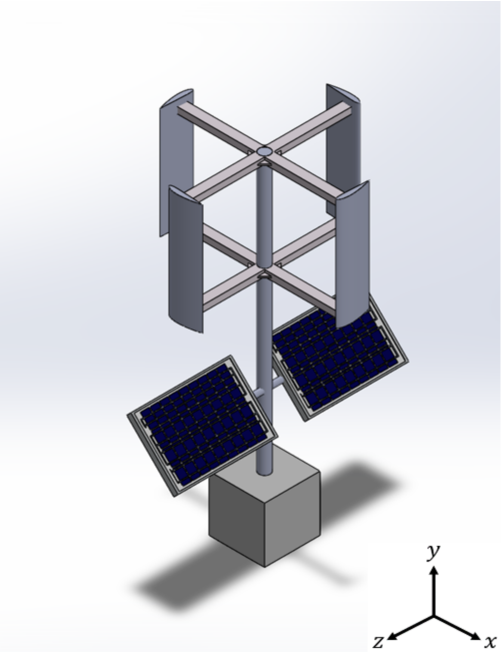

Figure 44: Concept 3

3.5.4 Concept 4

Concept number four includes an umbrella-like solar panel which consists of a flexible (thin-filmed) solar panel. Furthermore, the SMA actuation is the same as in concept 1 except concept 4 has one rotor blade more.

Table 9: Functions and options regarding concept 4

Function	Option
Number of rotor blades	3
Strut-blade ratio	2
Turbine solidity	Average ($S = 0.5$)
SMA actuation	Rotor blade rotates around y-axis
NACA airfoil geometry	Asymmetrical 24xx
NACA airfoil chord thickness	xx18
Solar panel structure	Flexible
Solar panel tracking method	None

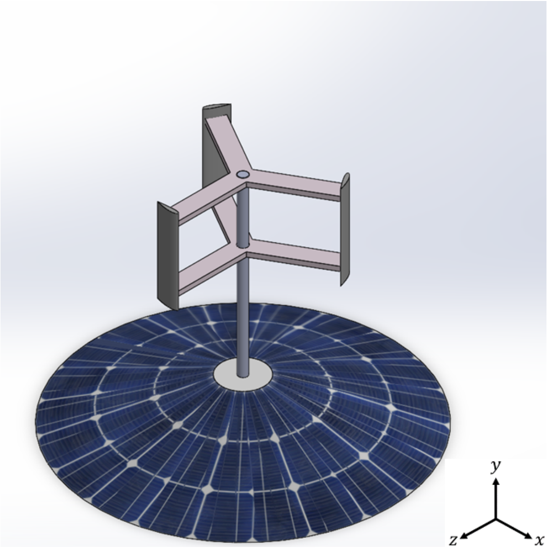

Figure 45: Concept 4

3.5.5 Concept 5

The characteristics of the fifth concept are presented in Table 10 and the visualisation is displayed in Fig. 46. The structure of the solar panel is fixed and there is no tracking method integrated into this concept.

Table 10: Functions and options regarding concept 5

Function	Option
Number of rotor blades	2
Strut-blade ratio	1
Turbine solidity	Average ($S = 0.5$)
SMA actuation	Rotor blade rotates around x- or z-axis
NACA airfoil geometry	Symmetrical 00xx
NACA airfoil chord thickness	xx21
Solar panel structure	Fixed
Solar panel tracking method	None

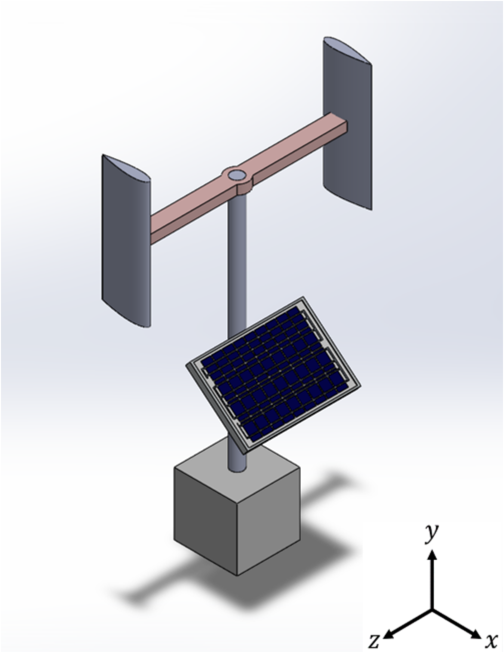

Figure 46: Concept 5

The SMA actuation in this concept results in both rotor blades pointing outward, creating a V-shape as can be seen in Fig. 47. This shape might increase the self-starting capabilities of the VAWT.

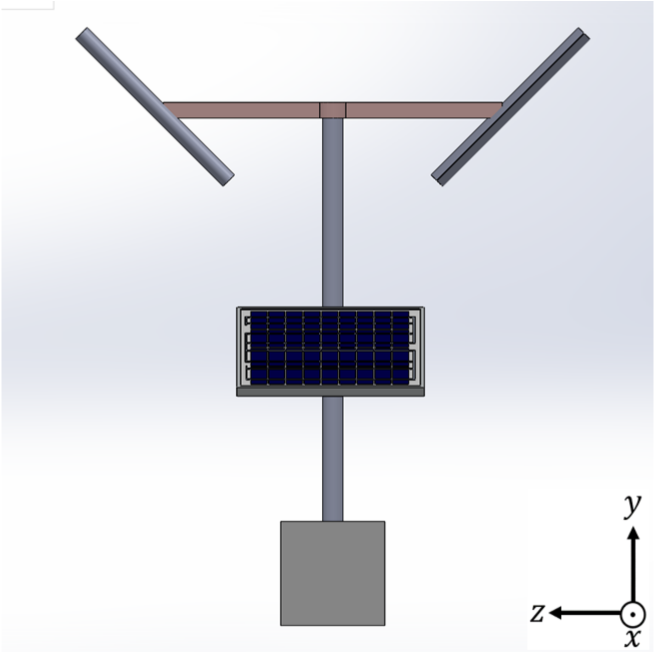

Figure 47: Front view of concept 5

3.5.6 Concept 6

Concept 6 has the same SMA actuation mechanism as the first concept but also has one rotor blade more. This concept contains many solar panels which can be manually adjusted. For example, if one correctly adjusts the solar panels monthly, 17% more efficiency is gained[34]. However, because of the VAWT, shadow flicker occurs. Therefore, the true efficiency gained by adjusting the solar panel manual may be lower.

Table 11: Functions and options regarding concept 6

Function	Option
Number of rotor blades	3
Strut-blade ratio	2
Turbine solidity	High ($S = 0.8$)
SMA actuation	Rotor blade rotates around y-axis
NACA airfoil geometry	Symmetrical 00xx
NACA airfoil chord thickness	xx18
Solar panel structure	Fixed
Solar panel tracking method	Manual

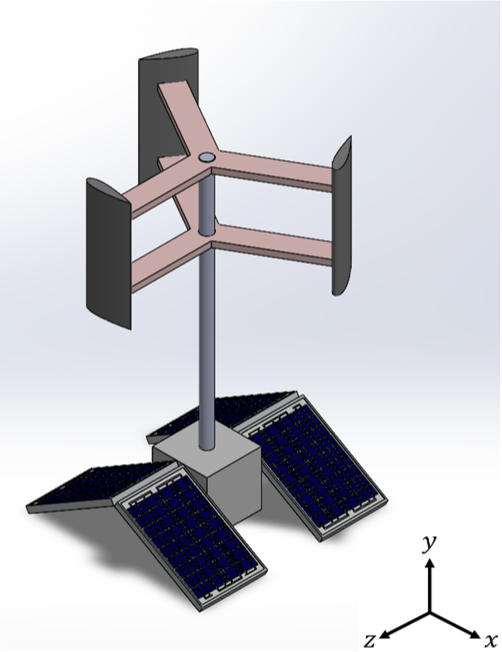

Figure 48: Concept 6

3.6 Concept evaluation

In pursuance of choosing the most suitable concept, a decision matrix has been established as can be seen in Table 12. The assembly time represents how much time it takes to assemble the concepts concerning their components. The material cost speaks for itself. Manufacturability represents how easy the components are produced. The noise emission of the concept determines how much aerodynamic noise is created due to the flow of air over the rotor blades. The lower the TSR, the lower the aerodynamic noise is from wind turbines[39][77].

Table 12: Decision matrix

Criteria	Weight	Concept 1	Concept 2	Concept 3	Concept 4	Concept 5	Concept 6
Assembly time	0.2	3	3	2	2	3	2
Material cost	0.1	3	3	2	2	3	2
Manufacturability	0.3	4	3	2	3	4	3
Noise emission	0.3	3	3	4	3	3	4
Durability	0.1	2	2	4	3	2	3
Total score	1	3.2	2.9	2.8	2.7	3.2	3

Scale	1	Poor
	2	Unsatisfactory
	3	Satisfactory
	4	Very satisfactory
	5	Excellent

As two concepts have the same score, a decision has to be made between the two designs. Concept 1 is more complex since one rotor blade has to point inward whereas the other rotor blade has to point outward. Moreover, the direction of the wind is required to point the rotor blades in the correct position. For concept 2, the direction of the wind is not necessary when morphing the rotor blades. Last but not least, optimising pitch angles regarding rotor blades has already shown that it improves the self-starting capabilities of the VAWT[42][133][67]. However, concept 2 morphs into a V-shape which is not well explored yet in the field of VAWTs regarding self-starting capabilities and overall performance which was observed by [122]. Other developed and undeveloped VAWTs are illustrated in Fig. 49 and the undeveloped V-VAWT is highlighted.

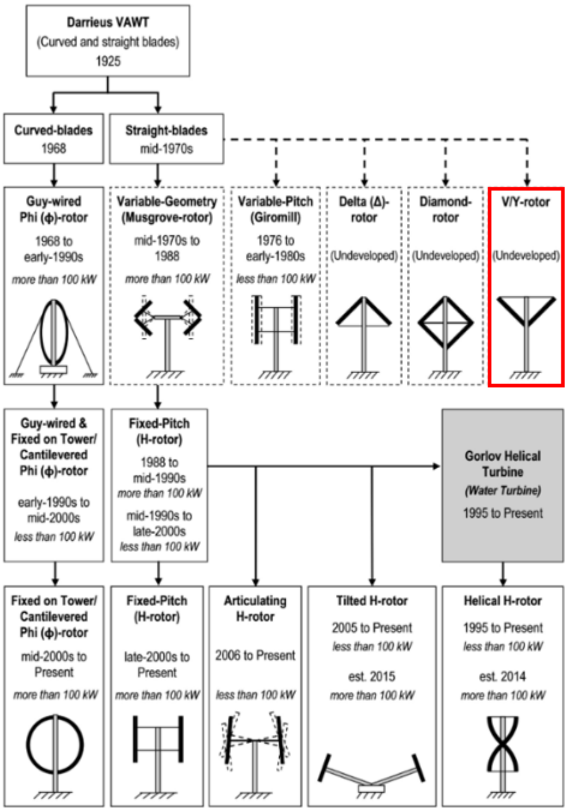

Figure 49: Timeline of various vertical axis wind turbine configurations[122]

Hence, concept 2 will be chosen as the final design considering it contributes more to the field of wind turbines.

3.7 Final concept expectations

The surface area of the V-VAWT is 0.173m as opposed to the surface area of the SB-VAWT which is 0.24m. The difference in surface area is noticeable in Fig. 50. A lower surface area results in the turbine can extract less wind energy.

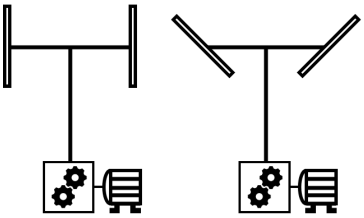

Figure 50: Schematic front view of SB-VAWT and the V-VAWT with gearbox and generator

In addition, the aspect ratio is analysed. The V-VAWT has a lower aspect ratio compared to the SB-VAWT. As mentioned before, a lower aspect ratio results in higher efficiency. Assuming a rotor angle of 45 degrees, the V-VAWT has a lower surface area compared to the SB-VAWT. The expectation is that the SB-VAWT has a better starting compared to the V-VAWT due to its higher surface area. However, the V-VAWT should have a higher efficiency in a certain TSR range or at a specific TSR. Due to the complex geometry of the NACA 0021 rotor blades and the incoming turbulent wind, numerical analysis with the means of CFD is necessary for solving the behaviour of the turbine. Only then the expectations can be confirmed.

CHAPTER 4

Simulation phase

In this chapter, the CAD model will be utilised in ANSYS Fluent to simulate and analyse the performance of the VAWT. Both the neutral state and the actuated state will be covered during the simulations. ANSYS Fluent uses five steps in total for the simulation:

1. Geometry
2. Mesh
3. Setup
4. Solution
5. Results

In this chapter, the first four steps are considered whereas the fifth step will be discussed in the next chapter as the results will be examined more extensively. The VAWT will be simulated in an environment that matches the dimensions of the OJF which is a low-speed wind tunnel located at the Delft University of Technology. A schematic of the OJF is shown in Fig. 51.

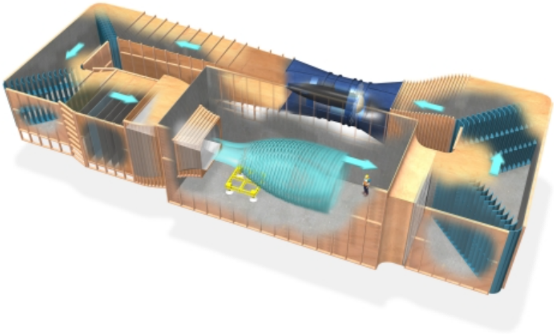

Figure 51: Schematic of the open jet facility[87]

4.1 Step 1: Geometry

The geometry of the wind tunnel is defined by expressing the dimensions in terms of the rotor radius R. The top view of the CAD model, which is imported in ANSYS Fluent, is visualised in Fig. 52.

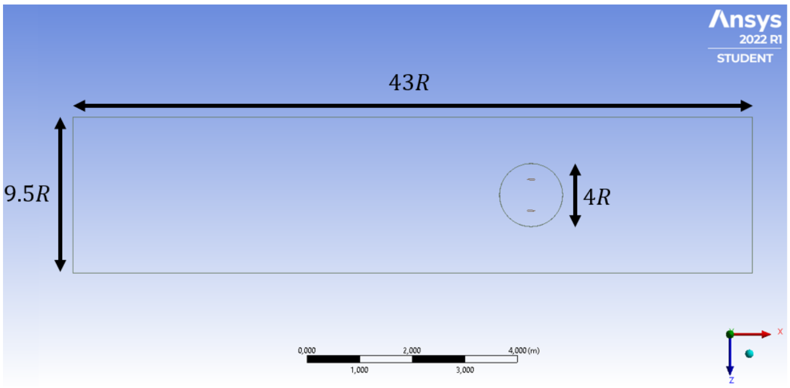

Figure 52: Top view of the geometry dimensions expressed in terms of the radius R

The CAD model is divided into two regions: an exterior part and an interior. The exterior part is represented as the stationary zone whereas the interior part is defined by a rotating zone. A 3D view of the CAD model is depicted in 53.

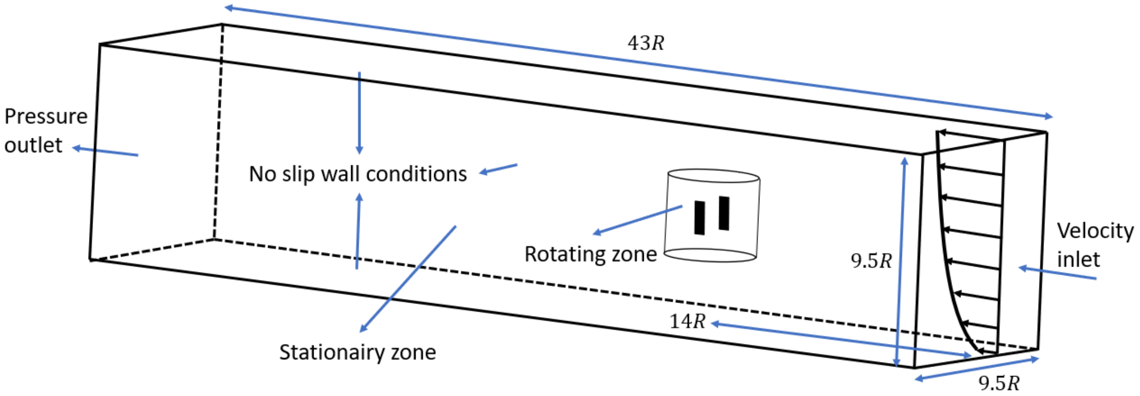

Figure 53: 3D view of the geometry dimensions expressed in terms of the radius R

Furthermore, the rotating zone contains the VAWT of which the characteristics are shown in Table 13. Only the two rotor blades are modelled.

Number of blades	2
Turbine radius (m)	0.30
Rotor blade height (m)	0.40
Chord length (m)	0.15
Rotor blade airfoil	NACA 0021

Table 13: Overview of the characteristics of the vertical axis wind turbine

4.2 Step 2: Mesh

After setting up the right geometry for the VAWT, an appropriate mesh has to be chosen. The ANSYS Fluent version used limits the number of cells/nodes by a maximum of 512,000. When a CAD model is being meshed, the model is divided into cells, nodes, faces and edges. For example, Fig. 54 shows a simple 3D computational grid with the aforementioned.

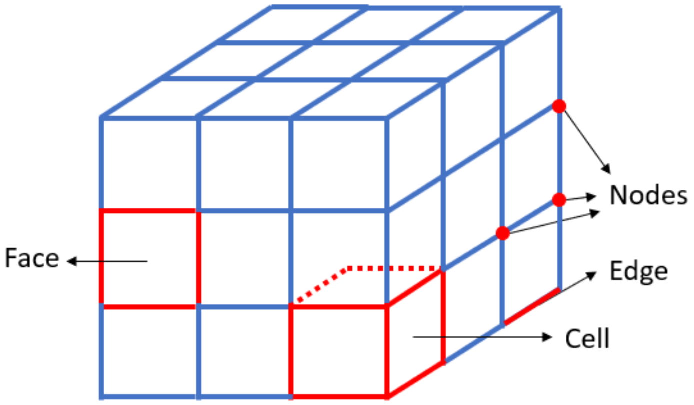

Figure 54: Simple 3D computational grid

The rotating zone, containing the rotor blades, is a cylinder in which the mesh is unstructured. The mesh of the cylinder consists of prisms and hexahedrons. The unstructured mesh grid of the stationary zone also consists of prisms and hexahedrons. The unstructured meshes of the zones are presented in Fig. 55.

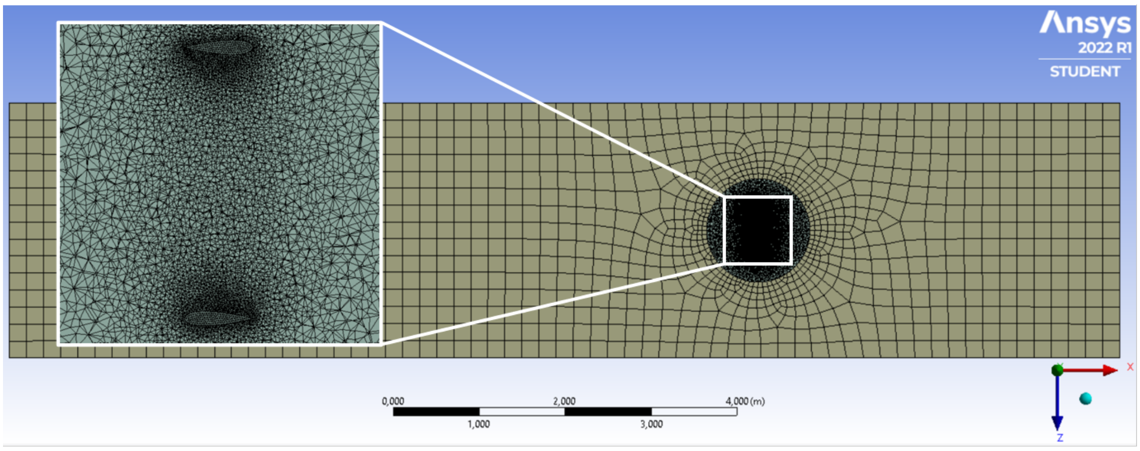

Figure 55: Unstructured mesh grid of the stationary and rotating zone

The region surrounding the rotor blades contains a mesh that exists out of tetrahedrons and prisms. Furthermore, inflation layers are integrated into the mesh.

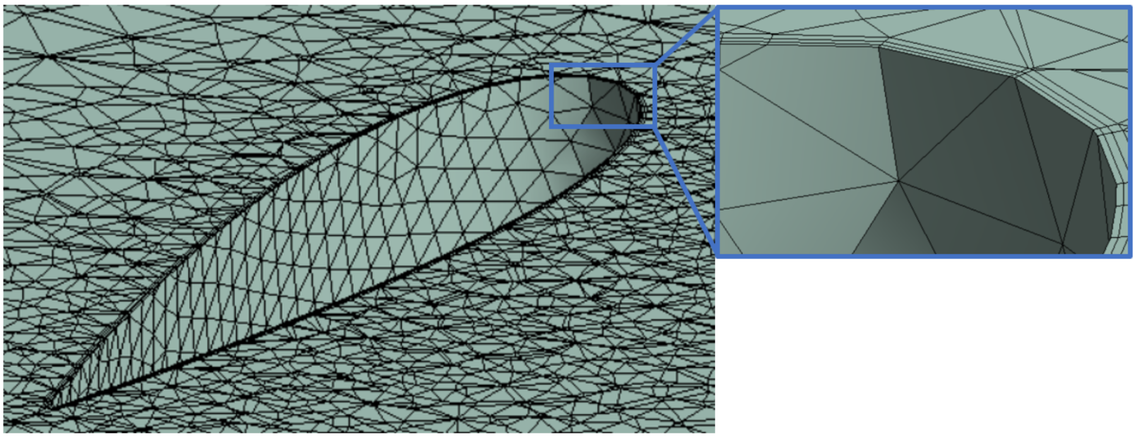

Figure 56: Unstructured mesh grid and inflation layer surrounding the rotor blades

After running the simulations with this mesh, the calculation time what immense. Therefore, the geometry and the mesh were adjusted so that the number of cells and nodes was decreased. The beam has been substituted by a cube as a stationary domain. The cylinder is replaced by a sphere instead of a rotating domain. The new geometry is visualised as a wireframe in Fig. 57.

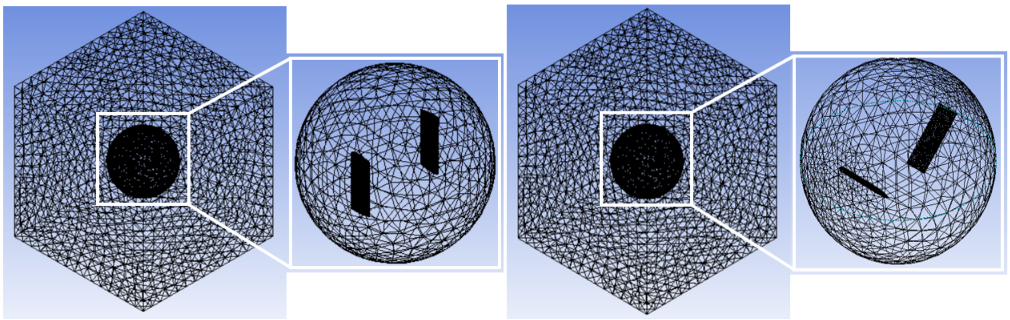

Figure 57: SB-VAWT mesh (left) and V-VAWT mesh (right)

The rotor blades were also adjusted by increasing the inflation layer number to five which can be seen in Fig. 58.

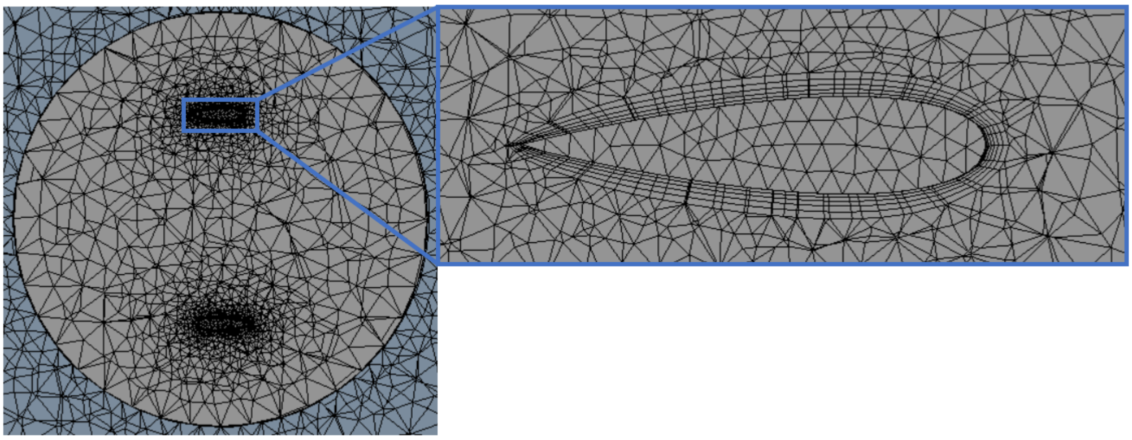

Figure 58: Intersection of the rotating domain

4.3 Step 3: Setup

The student version of ANSYS Fluent can utilise up to three cores of the central processing unit. Furthermore, the double-precision option is enabled. The boundary conditions are defined in Table 14.

Inlet	Velocity function:
Sliding mesh method	$2(1-\exp^{\frac{-Time}{0.1}})$
Sliding mesh method	$3(1-\exp^{\frac{-Time}{0.1}})$
Sliding mesh method	$6(1-\exp^{\frac{-Time}{0.1}})$
Dynamic mesh method	$10(1-\exp^{\frac{-Time}{0.1}})$
Outlet	Atmospheric pressure
Walls	No-slip
Turbulence model	SST $k-\omega$
Solver	Transient, pressure-based
Pressure-velocity coupling algorithm	SIMPLE

Table 14: Boundary conditions and parameters

Moreover, the $k-\omega$ SST turbulence model has been chosen for the calculations. The $k-\omega$ SST turbulence has good near wall behaviour as well as far field accuracy. After the model and the boundary conditions are defined, the dynamic mesh method (DMM) is enabled. Dynamic meshing is excellent for this scenario as the domain boundaries of the inner rotating part are adjusted over time. Thus, the computational grid can change its shape over time in order to adjust to the changing conditions. Besides the DMM, the sliding mesh method (SMM) is also used for the lower wind speeds for relatively low computational time and accurate results.

4.4 Step 4: Solution

The pressure-velocity coupling is used as a solution method for the simulations. The Semi-Implicit Method for Pressure Linked Equations algorithm is used. The time step size Δt is defined by (15), where C is the average cell size and V_{int} the velocity of the outer rim of the rotating domain. Therefore, the time step size is set to be 0.002 seconds is used for the DMM. The time step size for the SMM is not the same for every simulation. The rpm of the VAWT depends on the incoming undisturbed wind speed and the according TSR. The time step size depends on the angular velocity and has to be calculated keeping in mind that every rotation consists out of 360 degrees. Thus, the time step is chosen accordingly so that the turbine rotates one degree during one time step.

For every simulation using the SMM, ten rotations are considered.

$$\Delta t = \frac{C}{V_{int}} \tag{15}$$

4.5 Model verification

To verify the simulation model, the angular velocity is analysed. The velocity inlet is varied with 5, 7.5 and 10 as values for the terminal velocity. Recall that the terminal velocity of 10 is also present in Table 14. In order to analyse the angular velocity, the following function is used: $\frac{\lambda V_{\infty}}{R}$. During the first time steps, the TSR will be very low as the turbine barely rotates. The turbine radius is constant but the undisturbed wind speed will be varied. Hence, the expectations are that the angular velocity will behave accordingly due to the different undisturbed wind speeds. The velocity inlet function reaches its terminal velocity after approximately 300 time steps of 0.002 seconds. The inlet velocity function has been varied with four terminal velocities: 2.5, 5, 7.5 and 10. Each velocity function reaches its terminal velocity after approximately 0.6 seconds which is depicted in Fig. 59.

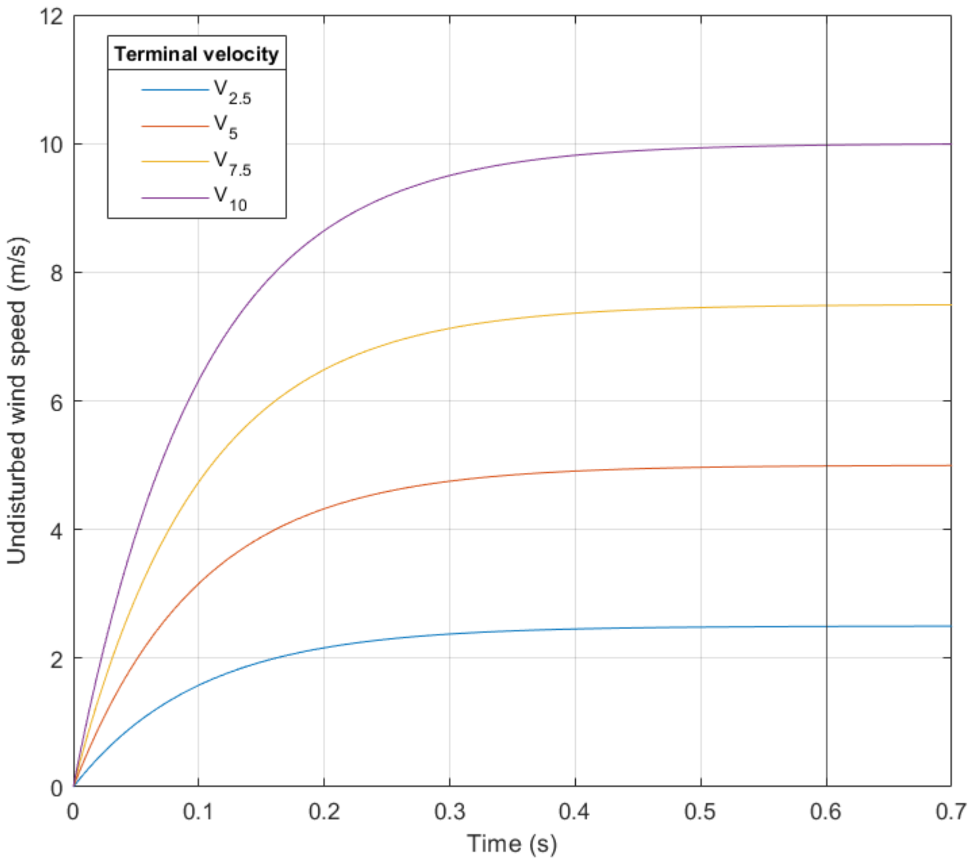

Figure 59: Undisturbed wind speed functions as the inlet boundary condition

What also can be concluded from the functions and the graphs, is that the velocity function with 10 as terminal velocity, also has the greatest acceleration. Due to this, it is also expected that the angular velocity does increase with each function. After carrying out four simulations, the results are presented in Table 15.

Inlet velocity function [m/s]	ω [rpm]
$2.5(1-\exp^{\frac{-Time}{0.1}})$	0.0002077997002440194
$5(1-\exp^{\frac{-Time}{0.1}})$	0.0008223377517424524
$7.5(1-\exp^{\frac{-Time}{0.1}})$	0.0013824814232066270
$10(1-\exp^{\frac{-Time}{0.1}})$	0.0024218306255837280

Table 15: Wind turbine angular velocity at $t = 0.6s$

As expected, if the terminal velocity increases, the angular velocity also increases.

4.6 Model validation

To validate the simulation model, the data of a real experiment by Swalwell et al. is used[116]. A NACA 0021 airfoil is used at a Reynolds number of $3.5 \cdot 10^5$. The data was obtained due to the pressure taps present on the airfoil. The airfoil was subjected to three different turbulence flow intensity I of 0.6%, 4% and 7%. Recall that the Reynolds number of an airfoil with a certain chord length is calculated by (9). For the validation, the following parameters, presented in Table 16, have been used for maintaining a Re_c of $3.5 \cdot 10^5$.

Parameter	value/function
Inlet velocity function [m/s]	$35(1-\exp^{\frac{-Time}{0.1}})$
Kinematic viscosity of air [$Pa \cdot s$]	$1.7894 \cdot 10^{-5}$
Turbulence intensity [-]	7%
Chord length [m]	0.15

Table 16: Parameters used for model validation

After running the simulation, the airfoil is analysed. The contour plot of the pressure acting on the airfoil is depicted in Fig. 60.

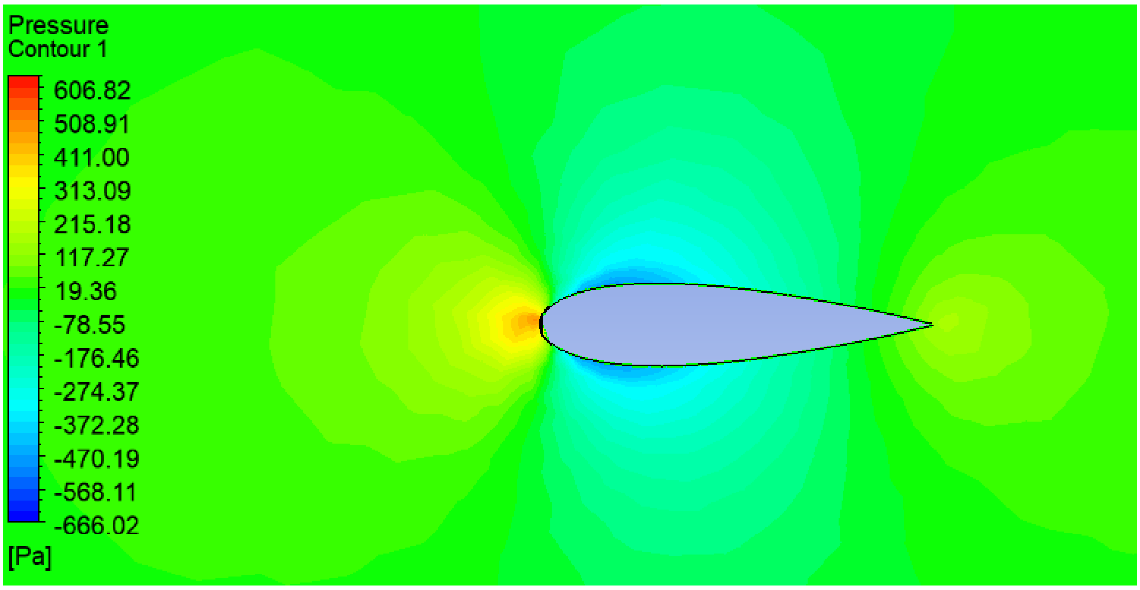

Figure 60: Pressure contour plot acting on the rotor blade

With the contour plot of the pressure known, the data is extracted in order to obtain the coefficient of pressure. The coefficient of pressure is given by (16) where P_∞ is the static pressure.

$$C_{pressure} = \frac{P - P_\infty}{\frac{1}{2}\rho_{air} V_\infty^2} \tag{16}$$

After extracting the data from ANSYS Fluent, the obtained data is joined with the experimental findings of Swalwell et al. The pressure coefficient versus distance x over chord length c is visualised in Fig. 61

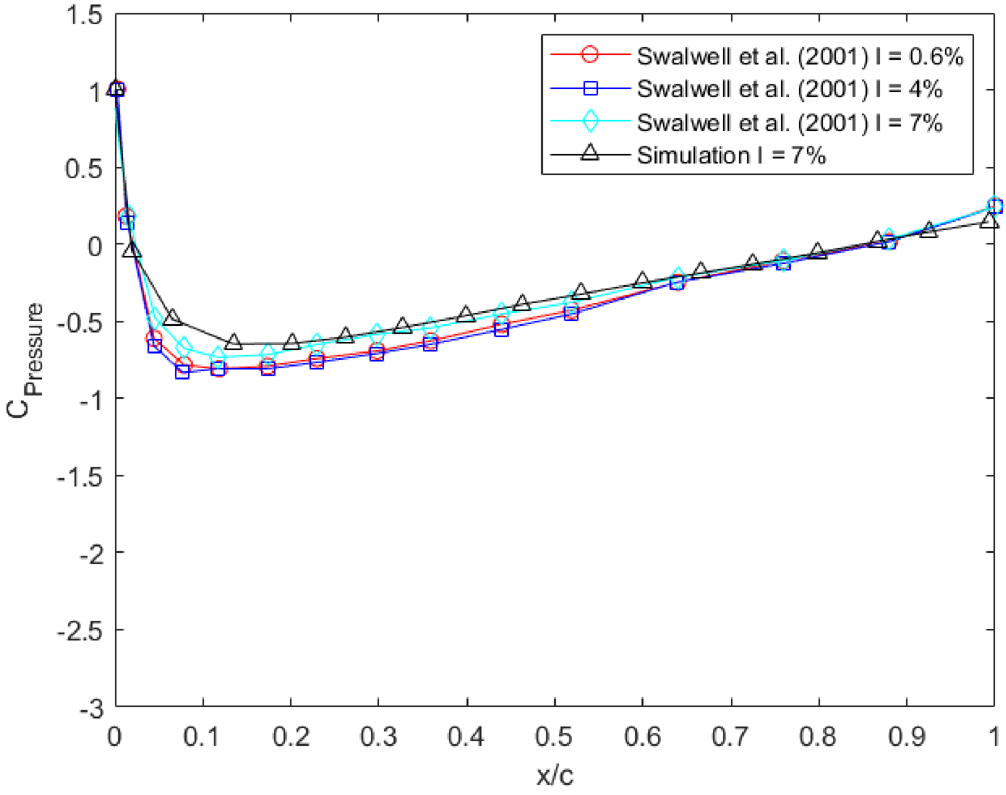

Figure 61: Experimental data from Swalwell et al. (2001) combined with simulation data

The simulation data does indeed come close to the experimental data from Swalwell et al. Therefore, the simulation model is validated. The largest deviation found between the experimental data and the simulation data is 9.3%.

CHAPTER 5

Results

Both the SB-VAWT and the V-VAWT are simulated. Each simulation took roughly 15,000 time steps to complete with ten iterations per step size with a step size of 0.002 seconds. That means that the first 30 seconds are simulated for both cases. Fig. 62 shows the angular velocity versus the time of the VAWTs. Both VAWTs have an initial angular velocity of zero before the undisturbed wind speed arrives at 0.1 seconds.

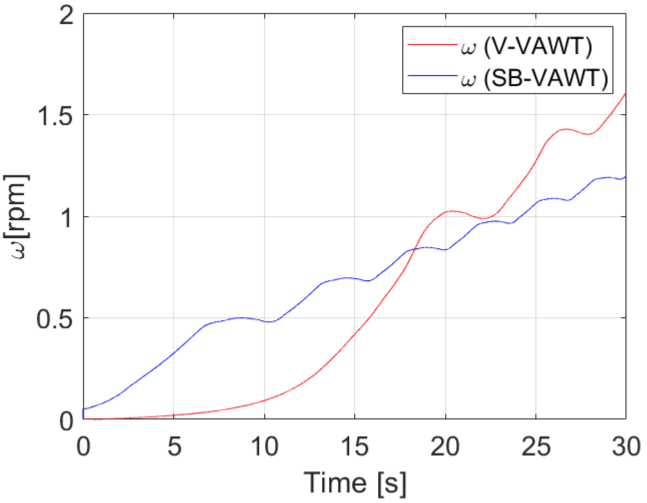

Figure 62: Angular velocity versus time at $V_\infty = 10$ m/s

After DMM, the SMM was used for the other simulations. The coefficient of lift versus the azimuth angle is plotted in Fig. 63 during an undisturbed wind speed of 2 m/s. Moreover, the coefficients of power and torque during an undisturbed wind speed of 2 m/s are depicted in Fig. 64.

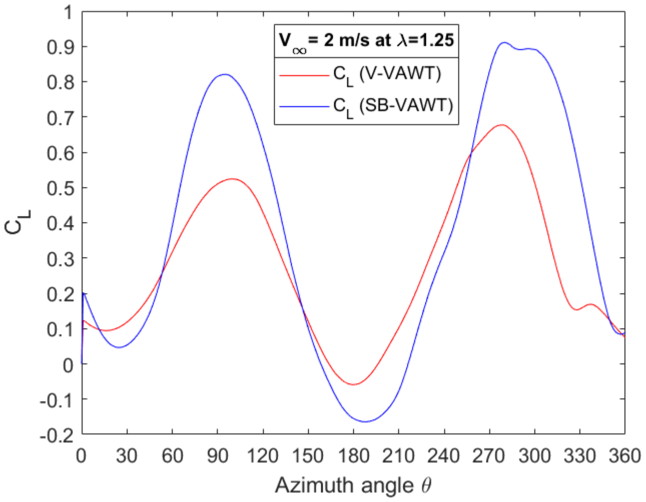

Figure 63: Coefficient lift versus azimuth angle at $V_\infty = 2$ m/s

After simulating the first cases, the inlet velocity was increased from 2 m/s to 3 m/s. The coefficient of torque and the coefficient of power were again plotted against the TSR which is illustrated in Fig. 65.

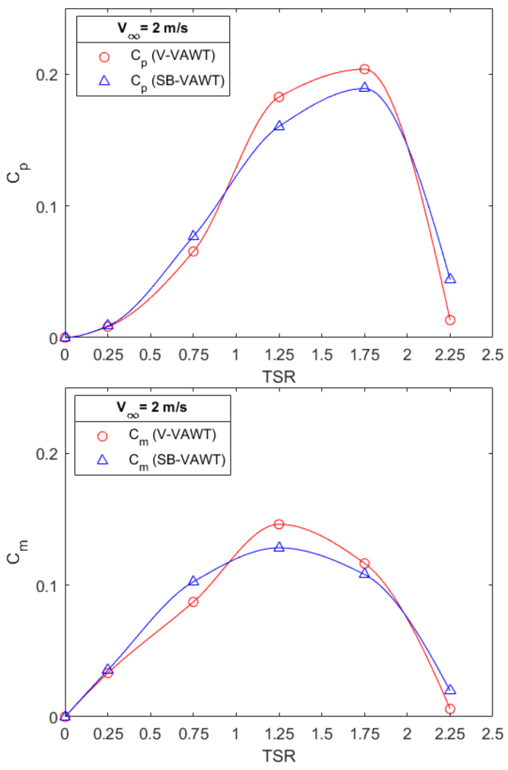

Figure 64: Coefficient of power and coefficient of torque versus TSR at $V_\infty = 2$ m/s

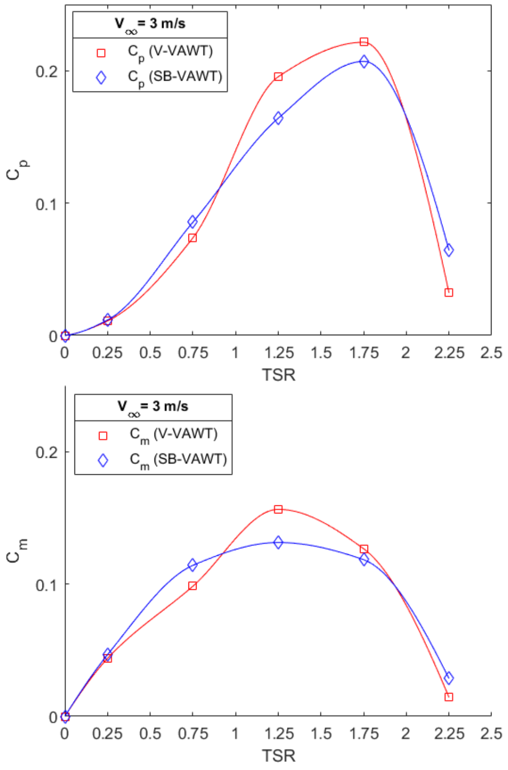

Figure 65: Coefficient of power and coefficient of torque versus TSR at $V_\infty = 3$ m/s

Furthermore, the results of the KPIs are presented in Table 17. The $C_p(\lambda)$ curves do not intersect at λ_{max}. Therefore, linear interpolation is used for obtaining λ_{max}. For the absolute power output, only the case where TSR equals 1.25 is considered. This is due to the fact that the difference between the coefficient of power and torque is the largest at that point regarding the two turbines.

		$V_\infty = 2$m/s		$V_\infty = 3$ m/s	
		SB-VAWT	V-VAWT	SB-VAWT	V-VAWT
KPI	Peak efficiency	0.189	0.204	0.207	0.222
	Average power coefficient	0.1011	0.1032	0.1106	0.1144
	Operational range	0<TSR<2.354	0<TSR<2.271	0<TSR<2.397	0<TSR<2.309
	Absolute power output	1.88 W	1.55 W	2.90 W	2.49 W

Table 17: Key performance indicator results

After the considering the wind speeds of 2, 3 and 10 m/s for both turbines, the model will be further validated by comparing the SB-VAWT to experimental and analytical data during a wind speed of 6 m/s. First, the DMST model provided by the software of QBlade is used. Secondly, the experimental data from Yamada et al. (2011) is observed. The results of the CFD, analytical and experimental data is presented in Fig. 66.

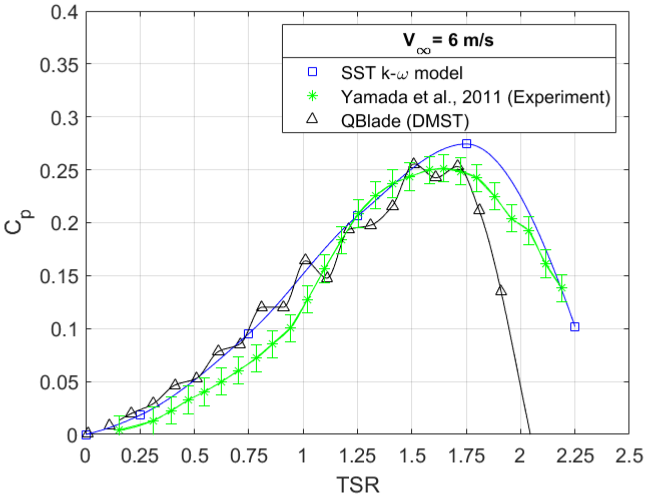

Figure 66: SB-VAWT data comparison

CHAPTER 6

Conclusion

The main research question was as follows:

"Does integrating actuation in a vertical axis wind turbine increase the maximum energy harvesting using the wind as an external stimulus?"

After defining the design criteria and constraints, the KPIs were identified. Thereafter, the CFD model software (ANSYS Fluent) and a matching turbulence model (SST $k-\omega$) were chosen. The results indicated that integrating actuation for increased energy harvesting using the wind as an external stimulus did not have a desirable effect on morphing the SB-VAWT into a V-VAWT under an angle of 45 degrees. For the energy transition to take place, the focus is now shifting faster to renewable energy sources. The VAWT is a potential candidate for also playing a role in this energy transition due to its unique characteristics compared to the already widely used HAWT. For example, the VAWT has its gearbox and generator located at the bottom of the turbine which makes installation and maintenance more convenient. They are also omnidirectional regarding the wind direction and are suitable for (sub)urban areas. The SB-VAWT proves to be the most potent candidate of the Darrieus (lift-based) VAWTs. Moreover, the SB-VAWT has superior self-starting capabilities over the V-VAWT considering the DMM with an inlet wind speed of 10 m/s. Furthermore, the average coefficient of lift of the SB-VAWT is higher than that of the V-VAWT. This was done by the SMM with an incoming wind speed of 2 m/s. However, the V-VAWT has a higher power coefficient approximately when $1<\text{TSR}<2$ (in which also the optimal TSR lies). But if the absolute power output is considered in that region, the V-VAWT performs worse than the SB-VAWT. This is also the case when the inlet wind speed is 3 m/s. The average power coefficient of the two turbines is very similar during an inlet wind speed of 2 and 3 m/s. The last KPI, the operational range, is also in favour of the SB-VAWT. Little research has been done on (variants of) the V-VAWT. Therefore, the SB-VAWT was further validated using experimental data from Yamada et al. (2011) and by utilising the analytical DMST model from the QBlade software with an inlet wind speed of 6 m/s. This work shows that morphing the rotor blades has significant effects on the KPIs. The V-VAWT is not a shape that should be preferred when morphing the rotor blades. Further research should be looking into other shapes in which the SB-VAWT can be changed. In addition, this work did not consider a force analysis such as the impact of centrifugal forces on both turbines. A thorough mechanical analyse should be made for investigating the consequences of these forces. If there is a promising shape for (temporarily) increasing the overall performance of the SB-VAWT, one should also make a trade-off between the structural reliability and the increased overall performance of the VAWT. Moreover, the extra energy due to actuation should also be taken into consideration. The VAWT suggested in this work has excellent dimensions in order to be tested in the OJF located at the TU Delft or similar wind tunnels. The mesh is also able to be improved even further. It is possible to add an additional region for each separate rotor blade. Likewise, a study can also look into the least amount of nodes and cells that are acquired for obtaining consistent results. Thereafter, a less computational demanding turbulence model might come available that suits the CFD model. In other words, an optimum can be found concerning the mesh size and the turbulence model. Lastly, for utilising the energy one can harvest from one square meter, it can be beneficial to include solar panels (with a tracking system). This will result in a hybrid power unit that can be connected to an inverter. For actuation, it might be interesting to look into SMA as SMA actuators do not have many parts and have a relatively large power density compared to conventional actuators.

CHAPTER A

Scientific paper

Morphing a Straight-bladed Vertical Axis Wind Turbine Design: CFD-Based Analysis

Thijs Eijkhout
Maritime and Transport Technology
Delft University of Technology
Delft, Netherlands
T.J.M.Eijkhout@student.tudelft.nl

***Abstract*—Wind turbines have proven to be an essential part for the green energy mix. However, the focus was mainly on the horizontal axis wind turbines whereas the vertical axis wind turbine did not receive that amount of attention. In this work a straight-bladed vertical axis wind turbine (SB-VAWT) is explored which can temporary adjusts its rotor blades in order to increase its overall performance. Also, shape memory alloy (SMA) as an actuator is shortly investigated as a potential addition to the wind turbine. After generating and evaluating several concepts, the vertical axis wind turbine shaped in a V (V-VAWT) was still undeveloped and proves to be a potential candidate. There is a relationship between the turbine solidity and the optimal TSR which directly affects the coefficient of power. For design purposes, this is an excellent instrument to utilise. The overall performance of the V-VAWT and the SB-VAWT were compared using computational fluid dynamics (CFD) software from ANSYS Fluent. The SB-VAWT and the V-VAWT have the same solidity. Both the dynamic mesh and sliding mesh methods were executed with mainly the standard k-ϵ turbulence model. The results indicated that the SB-VAWT performs better regarding the starting capabilities whereas the V-VAWT performs better at the optimal tip-speed ratio (TSR). However, the V-VAWT does not have a higher absolute power output compared to the SB-VAWT at every TSR. The SB-VAWT is overall the better candidate considering the peak efficiency, average power coefficient, absolute power output and operational range. Therefore, it is not desirable to morph the SB-VAWT into a V-VAWT.**

***Index terms* - vertical axis wind turbine, VAWT, CFD, actuation, structural adaption**

I. Introduction

For decreasing the dependence on grey energy, alternative sustainable energy sources are the obvious direction society has to take. Wind and solar are the main renewable energy sources used for the energy transition. For example, the capacity of offshore wind farms has increased from 4.117 MW in 2011 to 18.814 MW in 2017 [1]. These wind farms exist mainly of one type of wind turbine, namely the horizontal axis wind turbine (HAWT). Besides the HAWT, there is the less popular vertical axis wind turbine (VAWT). Both the turbines extract their energy from the incoming wind, but they are very different in many ways. Besides that, they both have their advantages and disadvantages. The HAWT enjoyed a surge in interest after the oil crisis. Thus, the HAWT received technological development whereas the VAWT gained little attention in order to be improved. That changed when many countries were phasing out their grey energy sources such as natural gas and (lignite) coal. With renewed interests in the design of the VAWT, the VAWT gained more resources for further improving its design and performance. The HAWT is suited for high-volume production but requires a lot of space. Furthermore, turbine control is required for optimal operation whereas the installation and maintenance are rather complex. Installing and maintaining a HAWT is challenging as the gearbox and the generator are located tens of meters high in the hub of the wind turbine. The VAWT is omnidirectional regarding the incoming wind. Besides that, VAWTs are able to operate in turbulent wind conditions. Furthermore, they have a low cut-in speed which makes them potential candidates for urban areas. Moreover, its gearbox and generator are located close to the ground which facilitates maintenance. The main disadvantage of the Darrieus VAWT is that the self-starting capabilities are poor. The Savonius VAWT does not experience self-starting issues as the turbine is drag based whereas the Darrieus wind turbine is lift based. The abbreviation VAWT in this work refers to the straight-bladed Darrieus VAWT. In recent years, many suggestions have been done on improving the performance of the VAWT. For example, experiments with linkage systems have been carried out. The linkage system, shown in Fig. 1, shows that the angle of attack is varied in the upwind and the downwind region. As a result of this, the efficiency is increased compared to the situation where rotor blades are fixed [2]. Additionally, the rotor blade itself could also be adjusted for enhancing the performance of the VAWT. For instance, the gurney flap and the J-airfoil are depicted in Fig. 2 and Fig. 3, respectively. Depending on

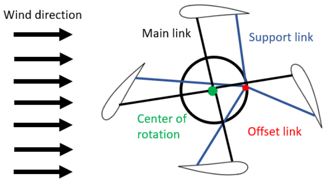

Fig. 1: Linkage system

Fig. 2: Airfoil with a gurney flap

Fig. 3: J-shaped airfoil

the location of the airfoil, the gurney flap is able to reduce aerodynamic loads and able to increase the coefficient of power [2] [3]. The J-airfoil is able to experience drag and lift simultaneously due to its concave area resulting in increased self-starting capabilities [4]. Lastly, the shape of the VAWT could also be changed. For instance, Fig. 4 shows how an SB-VAWT is adjusted by placing the rotor blades under an angle. Inclining the rotor blades under a 45-degree angle, the VAWT has better self-starting capabilities [5]. Thus, the geometry of the VAWT has an impact on the overall performance. This was also mentioned in [6] where different VAWT geometries were considered. The V-rotor, highlighted in red in Fig 5, is considered undeveloped. There are not many studies which have investigated the potential of the V-rotor. Besides that, temporarily morphing the VAWT into another geometry might also be beneficial for the overall performance. In this work, a new innovation will be analysed by integrating actuation in an SB-VAWT for morphing and/or moving the rotor blades for increasing its overall performance. First of all, a VAWT design will be proposed. After that, a CFD analysis will be conducted using ANSYS Fluent.

II. VAWT DESIGN

The design criteria for a newly suggested VAWT read as follows:

- Adaptive to wind circumstances
- Actuation integration

In addition, the design constraints are defined by:

- Geometry
- Testability
- Availability
- Viable performance model

The geometry of the design should not be too large in order to test the wind turbine in a wind tunnel. Moreover, the software has to be available for choosing the performance model. In this scenario, ANSYS Fluent is used. After generating multiple concepts, the V-VAWT is chosen as the final design. By implementing two linear actuators on the support struts, the blades are able to rotate around the pivot point transforming the SB-VAWT into the V-VAWT. Shape memory alloy (SMA) is a suitable candidate as SMA actuators have a very high power density [8]. Therefore, an SMA actuator can be relatively smaller than its conventional counterparts. Also, the airfoil chosen for the two rotor blades is the NACA 0021. The NACA 0021 has good starting capabilities and performs well when the TSR is lower than three [9]. The diameter D is 0.6m whereas the blade height H is defined as 0.4m. The chord length c is 0.15m which results in a VAWT with solidity S of 0.5. The solidity is given by (1), where N is the number of blades. A schematic of the VAWT is presented in Fig. 6 together with the gearbox and the generator.

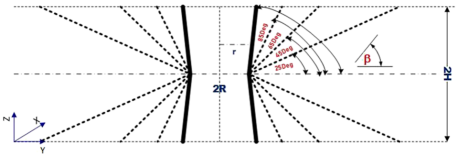

Fig. 4: Geometrical configurations [5]

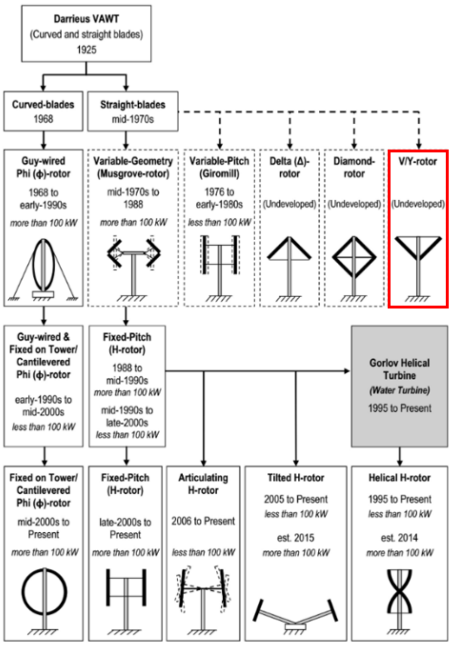

Fig. 5: Development of different geometries [6]

$$S = \frac{Nc}{D} \tag{1}$$

Each key performance indicator (KPI) reads as follows:

- Peak efficiency
- Average power coefficient
- Operational range
- Absolute power output

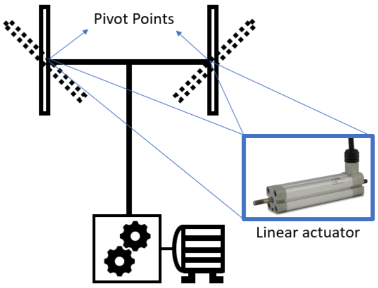

Fig. 6: Final concept

The peak efficiency is defined by the highest coefficient of power operating at an optimal TSR. The coefficient of power is given by (2).

$$C_p = \frac{P_m}{\frac{1}{2}\rho A V_\infty^3} \tag{2}$$

Here, P_m is the mechanical power the VAWT produces, ρ the density of air, A the surface area of the VAWT and V_∞ the undisturbed wind speed. The operational range is defined by the amount of TSR the VAWT is able to operate. The TSR λ is given by (3), where ω is the angular velocity and R is the turbine radius.

$$\lambda = \frac{\omega R}{V_\infty} \tag{3}$$

Furthermore, a relationship was found between the optimal TSR λ_{opt} and the turbine solidity S [11]. This relationship, given by (4), was suited for this VAWT design.

$$\lambda_{opt} = 2.693 S^{-0.329} - 1.605 \tag{4}$$

III. CFD Analysis

During the CFD simulations, both the SB-VAWT and the V-VAWT were investigated at different wind speeds. First of all, two computer-aided design (CAD) models were made. The outer part consists of a cube which is a stationary zone. Within the cube, there resides a sphere which contains the rotor blades. The inner part functions as the rotating part. Both meshes are shown in Fig. 7. For the CFD analysis two methods are used; namely the dynamic mesh method (DMM) and the sliding mesh method (SMM). The simulations were carried out with different undisturbed wind velocities. Moreover, the VAWTs rotate ten times during the simulations for receiving reliable results. The $k-\omega$ SST turbulence model was also used due to the fact it has good near-wall behaviour as well as far-field accuracy [10]. The parameters and boundary conditions used during the simulations are shown in Table I. The inlet velocity functions were defined as an expression to avoid very large peaks during the beginning of the simulations. Five inflation layers, illustrated in Fig. 8, were also introduced at the rotor blades in order to coop with the velocity gradients. An overview of the no-slip walls, inlet, outlet and rotating zone is illustrated in Fig. 9.

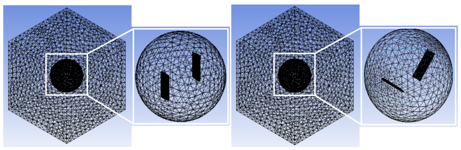

Fig. 7: SB-VAWT mesh (left) and V-VAWT mesh (right)

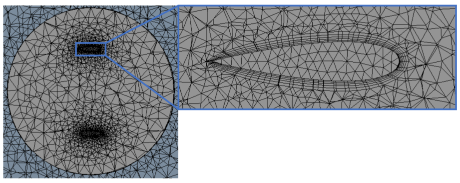

Fig. 8: Inflation layers at the rotor blades

Inlet	Velocity function:
Sliding mesh method	$2(1-\exp^{\frac{-Time}{0.1}})$
Sliding mesh method	$3(1-\exp^{\frac{-Time}{0.1}})$
Sliding mesh method	$6(1-\exp^{\frac{-Time}{0.1}})$
Dynamic mesh method	$10(1-\exp^{\frac{-Time}{0.1}})$
Outlet	Atmospheric pressure
Walls	No-slip
Turbulence model	SST $k-\omega$
Solver	Transient, pressure-based
Pressure-velocity coupling algorithm	SIMPLE

TABLE I: Boundary conditions and parameters

The SMM was used for calculating the coefficient of power and the coefficient of torque C_m at five different TSRs which are presented in Table II. The relationship between the coefficient of power and the coefficient of torque is given by (5). The dynamic mesh method is only used during a terminal inlet velocity function of 10 m/s. A relatively high undisturbed wind speed quickly identifies the dynamic behaviour of both turbines from a standstill.

$$Cp = \lambda Cm \tag{5}$$

λ [-]	0.25	0.75	1.25	1.75	2.25

TABLE II: Tip-speed ratio overview

IV. Results

First of all, the results of the DMM are illustrated in Fig. 10. Moreover, for the SMM simulations, the coefficient of lift plotted against the azimuth angle is depicted in Fig 11. The

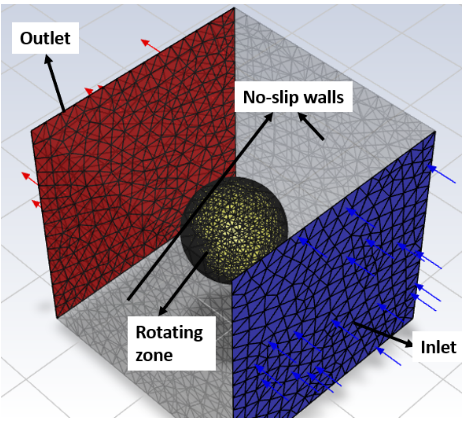

Fig. 9: Computational domain

according plots for the coefficient of power and the coefficient of torque are presented in Fig. 12 and Fig. 13. Furthermore, the results of the KPIs are defined in Table III. The $C_p(\lambda)$ curves do not intersect the TSR-axis. Therefore, a linear extrapolation has been carried out for obtaining the operational range. The absolute power output is only considered at a TSR of 1.25 because there the difference is the greatest between the two turbines. Besides that, the SB-VAWT is also simulated using $V_\infty = 6$ m/s. The experiment of Yamada et al. in 2011 used the same parameters except for the airfoil. Yamada et al. used the NACA 0020 which will be used for validation purposes. The NACA 0020 and the NACA 0021 have very similar characteristics. Moreover, QBlade software is also used for validation. QBlade uses the analytical double-stream-tube

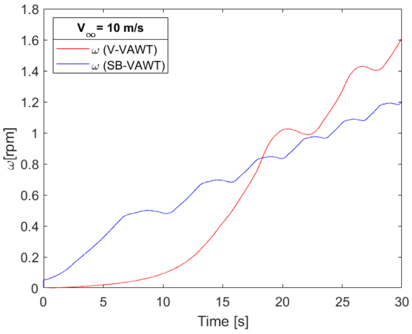

Fig. 10: Angular velocity versus time

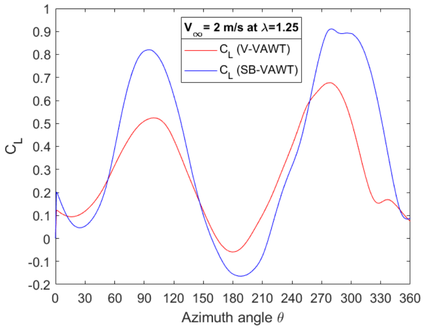

Fig. 11: Coefficient of lift versus azimuth angle

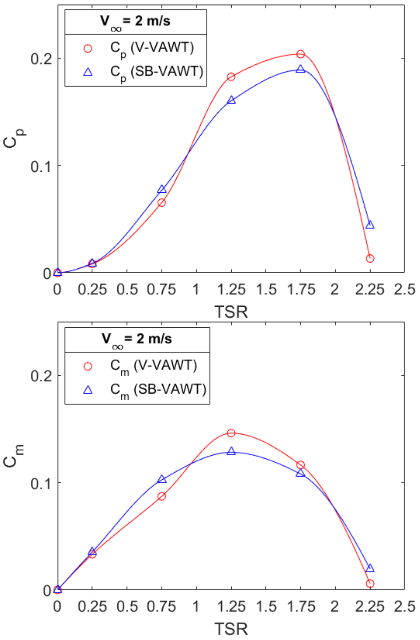

Fig. 12: Power coefficient and torque coefficient versus time

		$V_\infty = 2$m/s		$V_\infty = 3$ m/s	
		SB-VAWT	V-VAWT	SB-VAWT	V-VAWT
KPI	Peak efficiency	0.189	0.204	0.207	0.222
	Average power coefficient	0.1011	0.1032	0.1106	0.1144
	Operational range	0<TSR<2.354	0<TSR<2.271	0<TSR<2.397	0<TSR<2.309
	Absolute power output at TSR= 1.25	1.88 W	1.55 W	2.90 W	2.49 W

TABLE III: Key performance indicator results

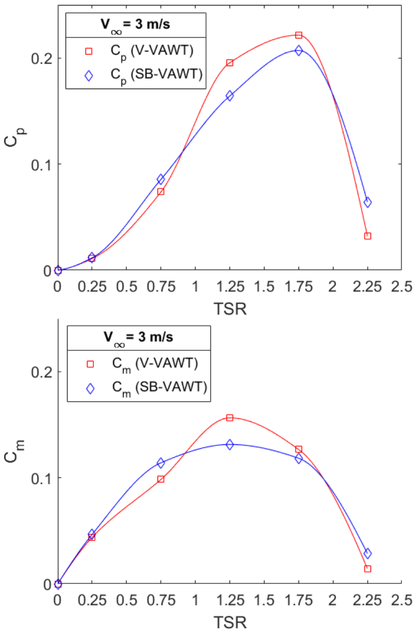

Fig. 13: Coefficient of power and coefficient of torque versus time

model (DMST). The results of the validation process are presented in Fig. 14.

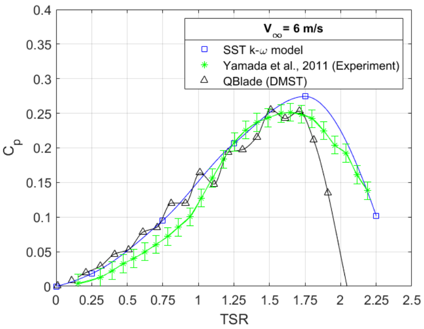

Fig. 14: SB-VAWT data comparison

V. Conclusion

(1) The applied DMM with $V_\infty = 10$ m/s shows that the SB-VAWT has better self-starting capabilities compared to the V-VAWT, but the V-VAWT is able to take over the SB-VAWT considering the angular velocity.
(2) The SB-VAWT experiences more lift overall compared to the V-VAWT.
(3) The V-VAWT has a higher coefficient of power and a higher coefficient of torque between a TSR of approximately 1 and 2 as opposed to the SB-VAWT.
(4) The V-VAWT has a smaller operational range than the SB-VAWT.
(5) The SB-VAWT has a higher absolute power output at every TSR in comparison with the V-VAWT.
(6) The DMST model has similar results compared to the SST $k-\omega$ model expect after at a TSR of approximately 1.75

Thus, the V-VAWT does indeed have a higher coefficient of power at the optimal TSR than the SB-VAWT. However, the absolute power output of the V-VAWT lies lower at the optimal TSR. Therefore, the V-VAWT is not desirable as opposed to the SB-VAWT. The SB-VAWT is overall the better option and actuating the rotor blades temporarily into a V-shape is not recommended.

References

[1] M. A. Majid ”Wind energy programme in India: Emerging energy alternatives for sustainable growth,” Energy and Environment (2019), Vol. 30.

[2] C. Xisto, J. Páscoa, and M. Trancossi ”Numerical analysis of design parameters with strong influence on the aerodynamic efficiency of a small-scale self-pitch VAWT,” In ASME International Mechanical Engineering Congress and Exposition (2015), Vol. 57342.

[3] H. Zhu, W. Hao, C. Li, and Q. Ding, ”Numerical study of effect of solidity on vertical axis wind turbine with Gurney flap,” In Journal of Wind Engineering and Industrial Aerodynamics (2019),” 186, 17-31.

[4] H. Zhu *et al*., ”Effect of geometric parameters of Gurney flap on performance enhancement of straight-bladed vertical axis wind turbine,” In Renewable Energy (2021), 165, pp 464-480.

[5] M. Zamani, M. Maghrebi, and S. R. Varedi, ”Starting torque improvement using J-shaped straight-bladed Darrieus vertical axis wind turbine by means of numerical simulation,” In Renewable Energy (2016), Vol. 95, pp 109-126.

[6] H.Abusannuga, and M. Özkaymak, ”The effect of geometry variants on the performance of VAWT-rotor with incline-straight blades,”In AIP Advances 11 (2021).

[7] W. Tjiu *et al*. ”Darrieus vertical axis wind turbine for power generation I: Assessment of Darrieus VAWT configurations,” Renewable energy (2015), Vol. 75, pp 50-67.

[8] W. Tjiu *et al*. ”Darrieus vertical axis wind turbine for power generation I: Assessment of Darrieus VAWT configurations,” Renewable energy (2015), Vol. 75, pp 50-67.

[9] A. Nespoli *et al*. ”The high potential of shape memory alloys in developing miniature mechanical devices: A review on shape memory alloy mini-actuators,” Sensors and Actuators A: Physical (2010), Vol. 158, pp 149-160

[10] S. C. Roh and S. H. Kang, ”Effects of a blade profile, the Reynolds number, and the solidity on the performance of a straight bladed vertical axis wind turbine,” Journal of Mechanical Science and Technology (2013), Vol. 27, pp 3299-3307.

[11] D. Adanta, I. R. Fattah and N.M. Muhammed ”Comparison of standard k-epsilon and SST k-omega turbulence model for breastshot waterwheel simulation,” Journal of Mechanical Science and Engineering (2010), Vol. 7, pp 39-44

[12] A. Rezaeiha, H. Montazeri and B. Blocken ”Towards optimal aerodynamic design of vertical axis wind turbines: Impact of solidity and number of blades,” in Energy, Vol. 165, pp 1129-1148

CHAPTER B

ANSYS Fluent screenshots

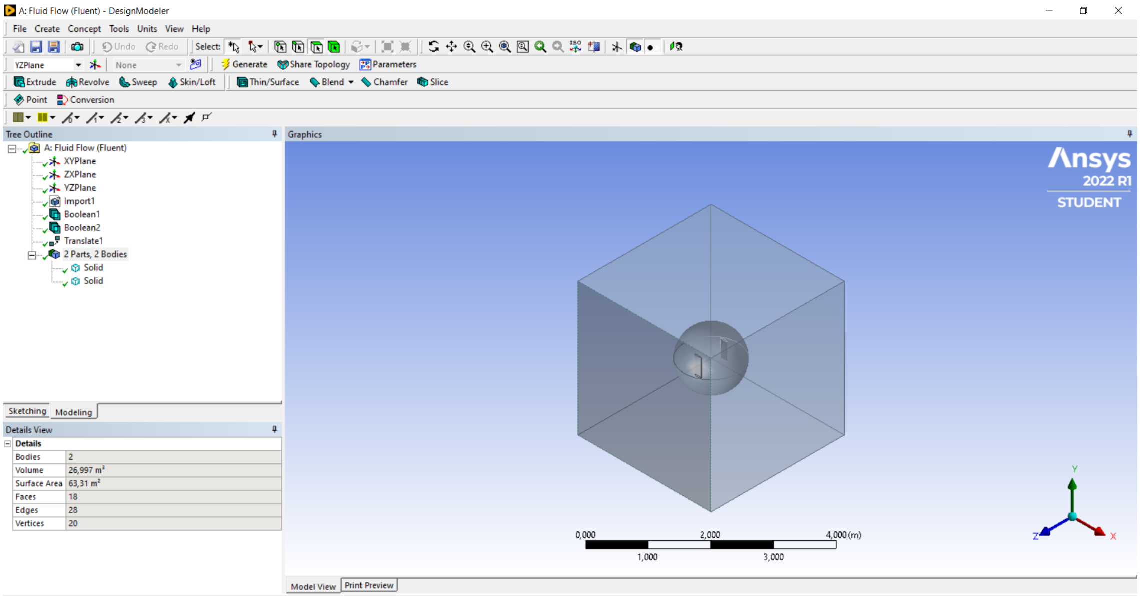

Details	
Bodies	2
Volume	26,997 m³
Surface Area	63,31 m²
Faces	18
Edges	28
Vertices	20

Figure 67: CAD model SB-VAWT

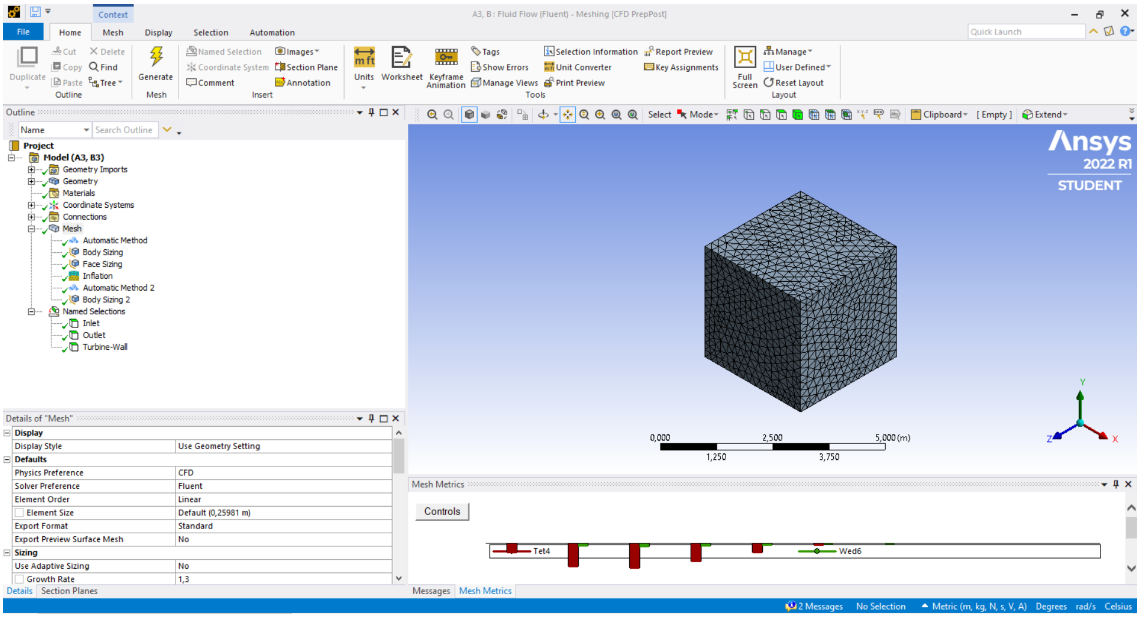

Details of "Mesh"

Display	
Display Style	Use Geometry Setting
Defaults	
Physics Preference	CFD
Solver Preference	Fluent
Element Order	Linear
☐ Element Size	Default (0,25981 m)
Export Format	Standard
Export Preview Surface Mesh	No
Sizing	
Use Adaptive Sizing	No
☐ Growth Rate	1,3

Figure 68: General mesh settings

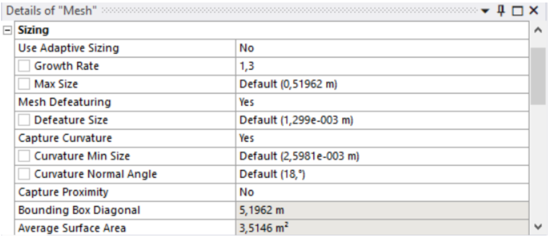

Details of "Mesh"

Sizing	
Use Adaptive Sizing	No
☐ Growth Rate	1,3
☐ Max Size	Default (0,51962 m)
Mesh Defeaturing	Yes
☐ Defeature Size	Default (1,299e-003 m)
Capture Curvature	Yes
☐ Curvature Min Size	Default (2,5981e-003 m)
☐ Curvature Normal Angle	Default (18,°)
Capture Proximity	No
Bounding Box Diagonal	5,1962 m
Average Surface Area	3,5146 m²

Figure 69: Mesh sizing settings

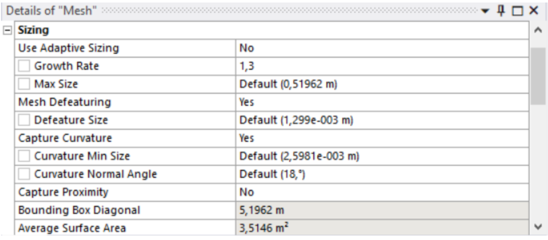

Details of "Mesh"

Sizing	
Use Adaptive Sizing	No
☐ Growth Rate	1,3
☐ Max Size	Default (0,51962 m)
Mesh Defeaturing	Yes
☐ Defeature Size	Default (1,299e-003 m)
Capture Curvature	Yes
☐ Curvature Min Size	Default (2,5981e-003 m)
☐ Curvature Normal Angle	Default (18,°)
Capture Proximity	No
Bounding Box Diagonal	5,1962 m
Average Surface Area	3,5146 m²

Figure 70: Mesh quality settings

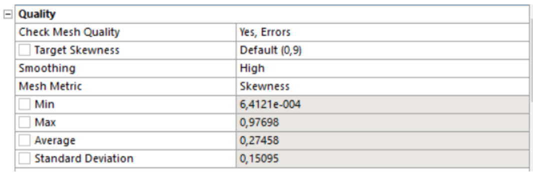

Quality	
Check Mesh Quality	Yes, Errors
☐ Target Skewness	Default (0,9)
Smoothing	High
Mesh Metric	Skewness
☐ Min	6,4121e-004
☐ Max	0,97698
☐ Average	0,27458
☐ Standard Deviation	0,15095

Figure 71: Inflation layer settings

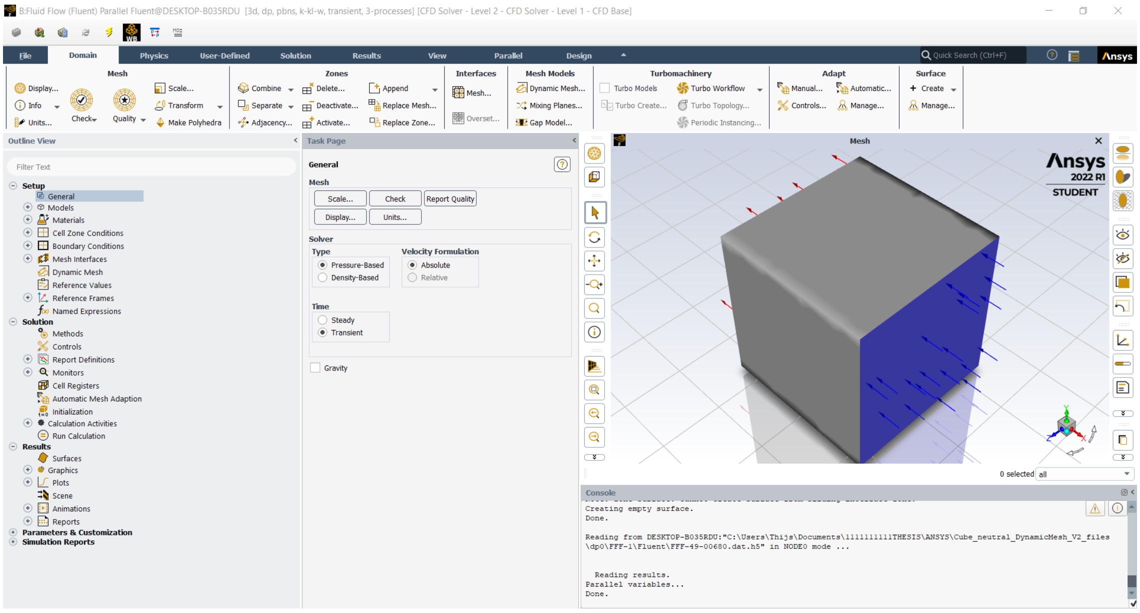

B:Fluid Flow (Fluent) Parallel Fluent@DESKTOP-B035RDU [3d, dp, pbns, k-kl-w, transient, 3-processes] [CFD Solver - Level 2 - CFD Solver - Level 1 - CFD Base]

Task Page

General

Mesh

Solver

Type: ● Pressure-Based ○ Density-Based

Velocity Formulation: ● Absolute ○ Relative

Time: ○ Steady ● Transient

☐ Gravity

Console

```
Creating empty surface.
Done.

Reading from DESKTOP-B035RDU:"C:\Users\Thijs\Documents\111111111THESIS\ANSYS\Cube_neutral_DynamicMesh_V2_files
\dp0\FFF-1\Fluent\FFF-49-00680.dat.h5" in NODE0 mode ...


  Reading results.
Parallel variables...
Done.
```

Figure 72: General solution settings

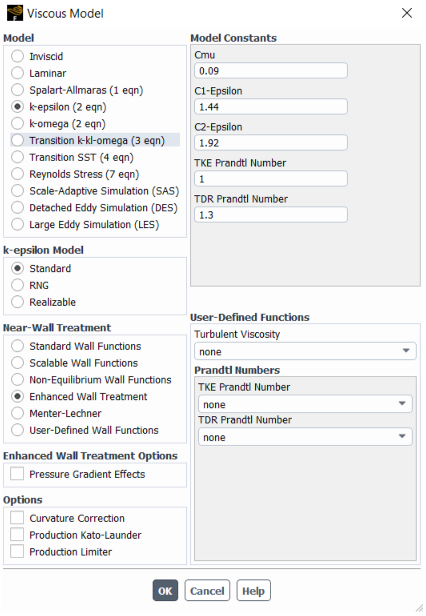

Viscous Model

Model
○ Inviscid
○ Laminar
○ Spalart-Allmaras (1 eqn)
● k-epsilon (2 eqn)
○ k-omega (2 eqn)
○ Transition k-kl-omega (3 eqn)
○ Transition SST (4 eqn)
○ Reynolds Stress (7 eqn)
○ Scale-Adaptive Simulation (SAS)
○ Detached Eddy Simulation (DES)
○ Large Eddy Simulation (LES)

k-epsilon Model
● Standard
○ RNG
○ Realizable

Near-Wall Treatment
○ Standard Wall Functions
○ Scalable Wall Functions
○ Non-Equilibrium Wall Functions
● Enhanced Wall Treatment
○ Menter-Lechner
○ User-Defined Wall Functions

Enhanced Wall Treatment Options
☐ Pressure Gradient Effects

Options
☐ Curvature Correction
☐ Production Kato-Launder
☐ Production Limiter

Model Constants
Cmu: 0.09
C1-Epsilon: 1.44
C2-Epsilon: 1.92
TKE Prandtl Number: 1
TDR Prandtl Number: 1.3

User-Defined Functions
Turbulent Viscosity: none

Prandtl Numbers
TKE Prandtl Number: none
TDR Prandtl Number: none

Figure 73: $k-\epsilon$ turbulence model

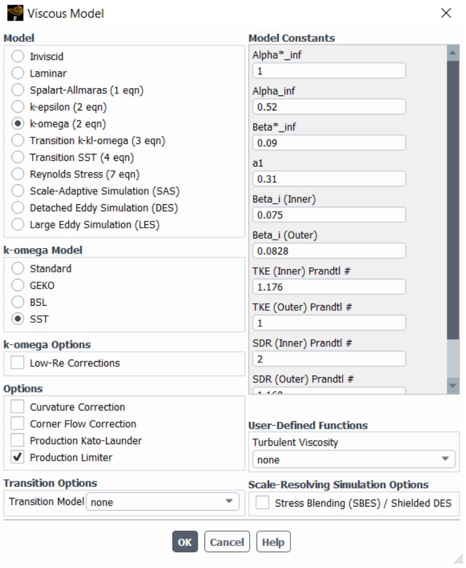

Viscous Model

Model
○ Inviscid
○ Laminar
○ Spalart-Allmaras (1 eqn)
○ k-epsilon (2 eqn)
● k-omega (2 eqn)
○ Transition k-kl-omega (3 eqn)
○ Transition SST (4 eqn)
○ Reynolds Stress (7 eqn)
○ Scale-Adaptive Simulation (SAS)
○ Detached Eddy Simulation (DES)
○ Large Eddy Simulation (LES)

k-omega Model
○ Standard
○ GEKO
○ BSL
● SST

k-omega Options
☐ Low-Re Corrections

Options
☐ Curvature Correction
☐ Corner Flow Correction
☐ Production Kato-Launder
☑ Production Limiter

Transition Options
Transition Model: none

Model Constants
Alpha*_inf: 1
Alpha_inf: 0.52
Beta*_inf: 0.09
a1: 0.31
Beta_i (Inner): 0.075
Beta_i (Outer): 0.0828
TKE (Inner) Prandtl #: 1.176
TKE (Outer) Prandtl #: 1
SDR (Inner) Prandtl #: 2
SDR (Outer) Prandtl #

User-Defined Functions
Turbulent Viscosity: none

Scale-Resolving Simulation Options
☐ Stress Blending (SBES) / Shielded DES

Figure 74: $k-\omega$ turbulence model

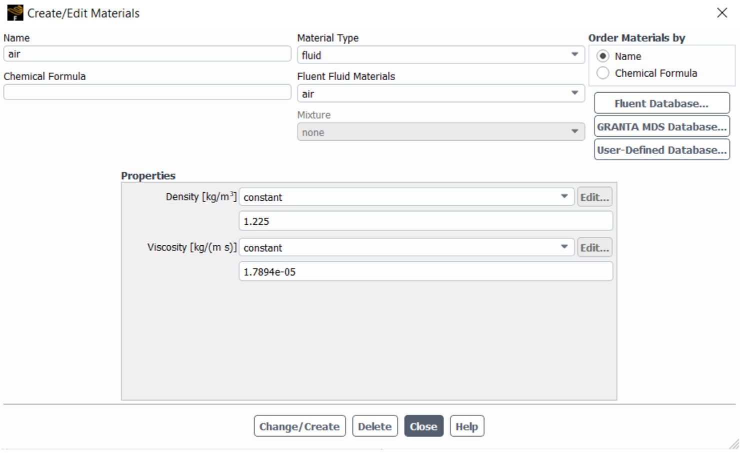

Name: air

Chemical Formula:

Material Type: fluid

Fluent Fluid Materials: air

Mixture: none

Order Materials by: ● Name ○ Chemical Formula

Properties

Density [kg/m^3]: constant

1.225

Viscosity [kg/(m s)]: constant

1.7894e-05

Figure 75: Fluid settings

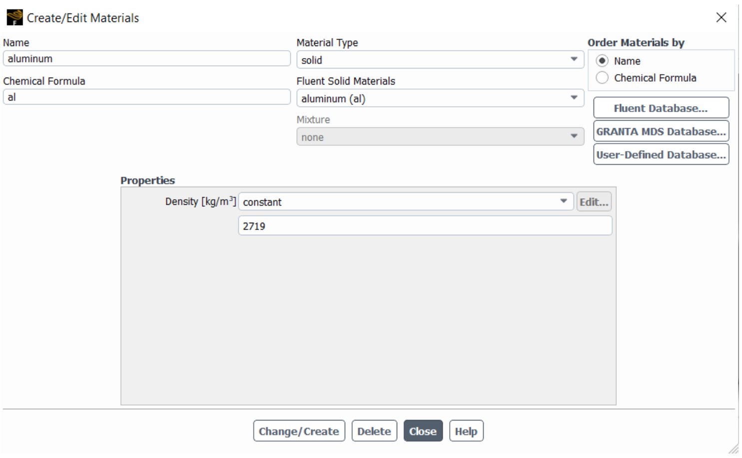

Name: aluminum

Chemical Formula: al

Material Type: solid

Fluent Solid Materials: aluminum (al)

Mixture: none

Order Materials by: ● Name ○ Chemical Formula

Properties

Density [kg/m^3]: constant

2719

Figure 76: Solid settings

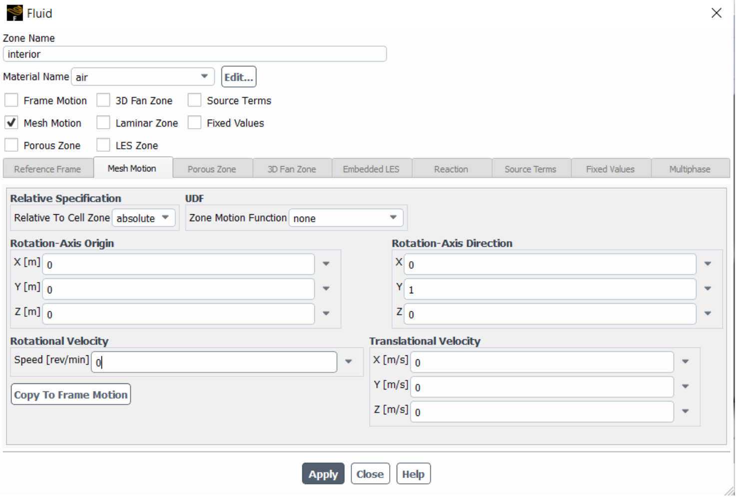

Zone Name: interior

Material Name: air

☐ Frame Motion ☐ 3D Fan Zone ☐ Source Terms

☑ Mesh Motion ☐ Laminar Zone ☐ Fixed Values

☐ Porous Zone ☐ LES Zone

Relative Specification

Relative To Cell Zone: absolute

UDF

Zone Motion Function: none

Rotation-Axis Origin

X [m] 0

Y [m] 0

Z [m] 0

Rotation-Axis Direction

X 0

Y 1

Z 0

Rotational Velocity

Speed [rev/min] 0

Translational Velocity

X [m/s] 0

Y [m/s] 0

Z [m/s] 0

Figure 77: Sliding mesh interior settings

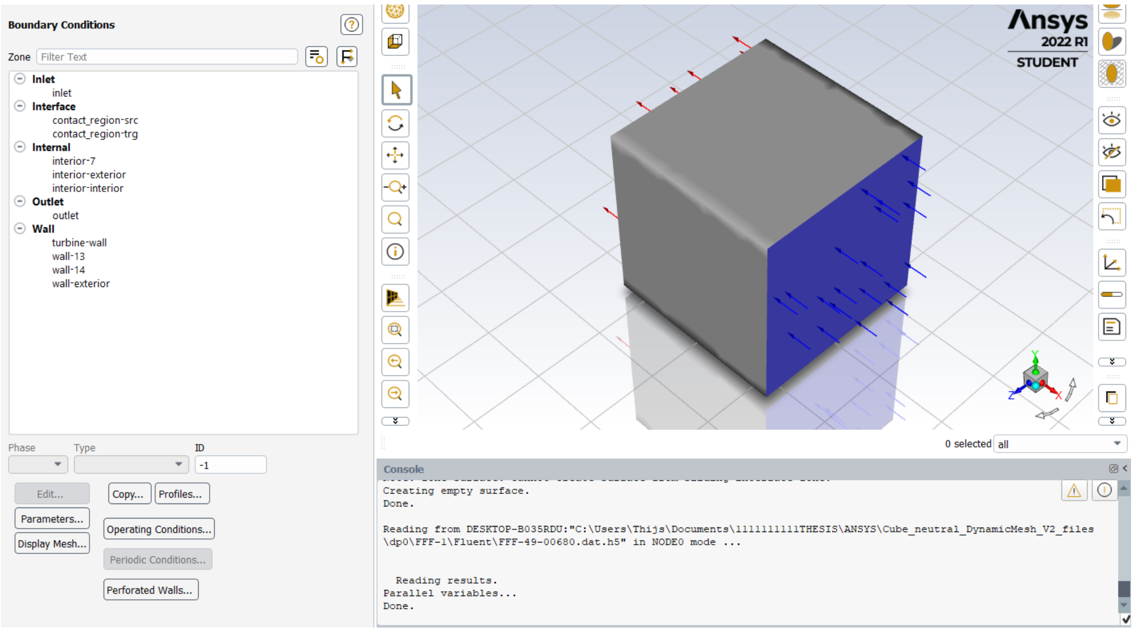

Boundary Conditions

Zone

- Inlet
  - inlet
- Interface
  - contact_region-src
  - contact_region-trg
- Internal
  - interior-7
  - interior-exterior
  - interior-interior
- Outlet
  - outlet
- Wall
  - turbine-wall
  - wall-13
  - wall-14
  - wall-exterior

ID: -1

0 selected: all

```
Creating empty surface.
Done.

Reading from DESKTOP-B035RDU:"C:\Users\Thijs\Documents\111111111THESIS\ANSYS\Cube_neutral_DynamicMesh_V2_files
\dp0\FFF-1\Fluent\FFF-49-00680.dat.h5" in NODE0 mode ...


  Reading results.
Parallel variables...
Done.
```

Figure 78: Boundary conditions per zone

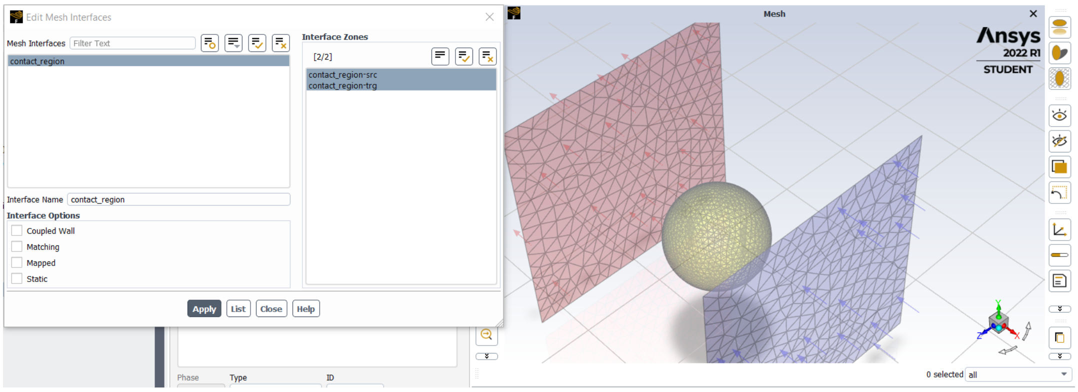

Edit Mesh Interfaces

Mesh Interfaces: contact_region

Interface Zones [2/2]: contact_region-src, contact_region-trg

Interface Name: contact_region

Interface Options

☐ Coupled Wall
☐ Matching
☐ Mapped
☐ Static

Figure 79: Contact region highlighted in yellow

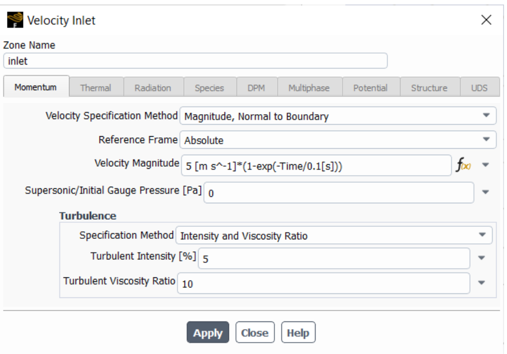

Velocity Inlet

Zone Name: inlet

Momentum

Velocity Specification Method: Magnitude, Normal to Boundary

Reference Frame: Absolute

Velocity Magnitude: 5 [m s^-1]*(1-exp(-Time/0.1[s]))

Supersonic/Initial Gauge Pressure [Pa]: 0

Turbulence

Specification Method: Intensity and Viscosity Ratio

Turbulent Intensity [%]: 5

Turbulent Viscosity Ratio: 10

Figure 80: Inlet settings

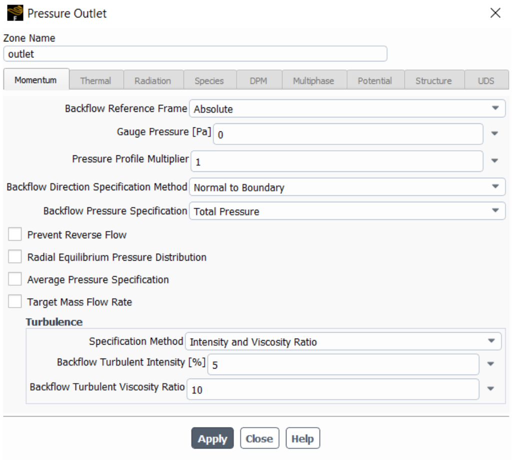
Pressure Outlet

Zone Name: outlet

Backflow Reference Frame: Absolute
Gauge Pressure [Pa]: 0
Pressure Profile Multiplier: 1
Backflow Direction Specification Method: Normal to Boundary
Backflow Pressure Specification: Total Pressure

☐ Prevent Reverse Flow
☐ Radial Equilibrium Pressure Distribution
☐ Average Pressure Specification
☐ Target Mass Flow Rate

Turbulence
Specification Method: Intensity and Viscosity Ratio
Backflow Turbulent Intensity [%]: 5
Backflow Turbulent Viscosity Ratio: 10

Figure 81: Outlet settings

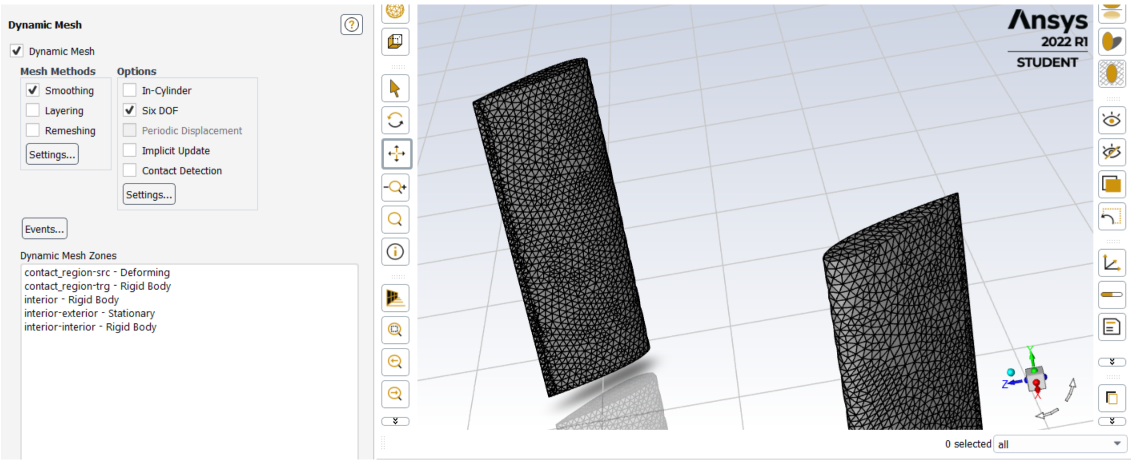
Dynamic Mesh

☑ Dynamic Mesh

Mesh Methods
☑ Smoothing
☐ Layering
☐ Remeshing

Options
☐ In-Cylinder
☑ Six DOF
☐ Periodic Displacement
☐ Implicit Update
☐ Contact Detection

Dynamic Mesh Zones
contact_region-src - Deforming
contact_region-trg - Rigid Body
interior - Rigid Body
interior-exterior - Stationary
interior-interior - Rigid Body

Figure 82: Dynamic mesh settings

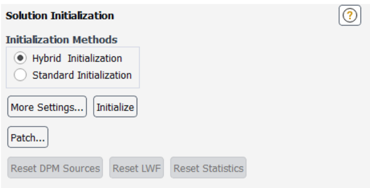
Solution Initialization

Initialization Methods
● Hybrid Initialization
○ Standard Initialization

Figure 83: Initialisation settings

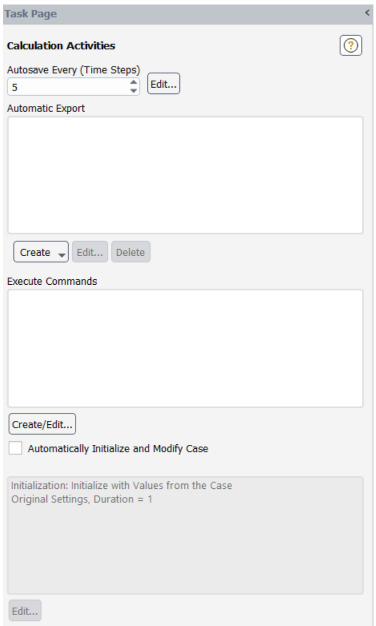

Autosave Every (Time Steps): 5

☐ Automatically Initialize and Modify Case

Initialization: Initialize with Values from the Case
Original Settings, Duration = 1

Figure 84: Calculation activities

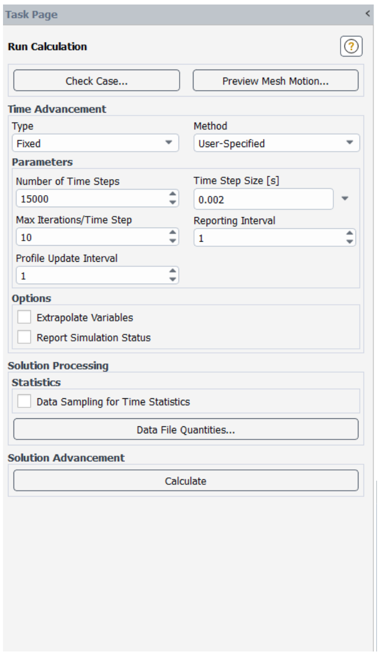

Type: Fixed
Method: User-Specified
Number of Time Steps: 15000
Time Step Size [s]: 0.002
Max Iterations/Time Step: 10
Reporting Interval: 1
Profile Update Interval: 1

☐ Extrapolate Variables
☐ Report Simulation Status
☐ Data Sampling for Time Statistics

Figure 85: Run calculation settings

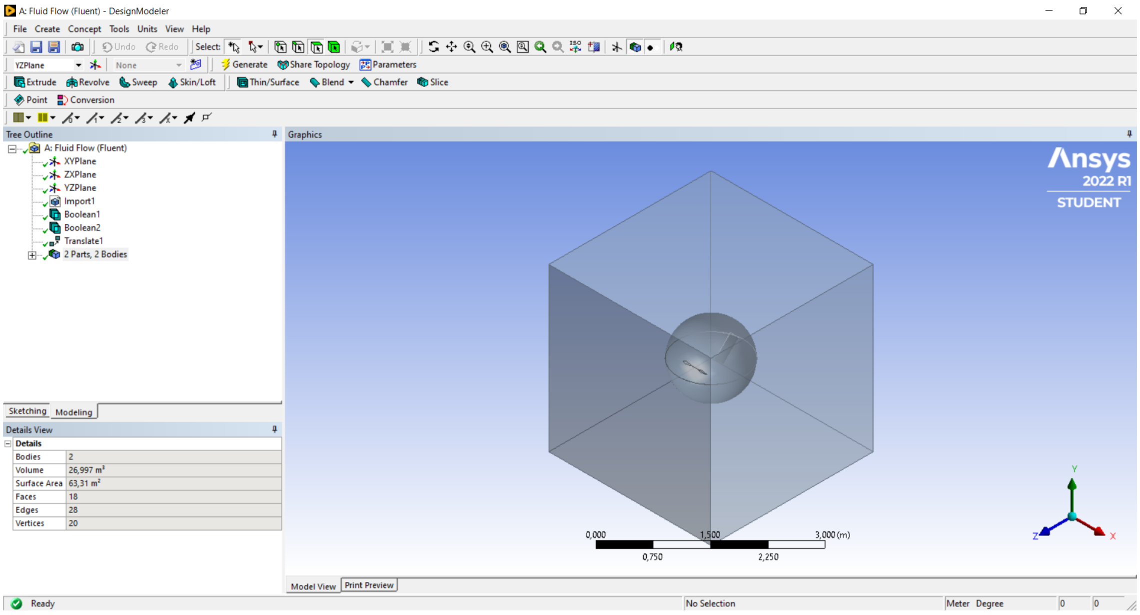

Details View

Details	
Bodies	2
Volume	26,997 m³
Surface Area	63,31 m²
Faces	18
Edges	28
Vertices	20

Figure 86: CAD model V-VAWT

CHAPTER C

Matlab codes

```
close all
clear all
%Matlab code Thijs Eijkhout - 4385993
%Morphing a Straight-bladed Vertical Axis Wind Turbine Design: CFD Based Analysis
%%
%Dynamic mesh method
O_n = readmatrix('DataFile.xlsx','range','M3:M15003'); %omega [rpm] SB-VAWT
Omega_n = transpose (O_n);
lambda_n=linspace(0,30,15001);
O_a = readmatrix('DataFile.xlsx','range','L3:L15003'); %omega [rpm] V-VAWT
Omega_a = transpose (O_a);
lambda_a=linspace(0,30,15001);
figure(1);
plot(lambda_a, Omega_a, 'r', lambda_n,Omega_n, 'b');
title(legend, 'V_{\infty}= 10 m/s');
ax = gca;
ax.FontSize = 12;
xlabel('Time [s]');
ylabel('\omega[rpm]');
legend('\omega (V-VAWT)','\omega (SB-VAWT)');
%%
%Terminal velocity functions.
Time=linspace(0,1,500);
V_1=2.5*(1-exp(-Time/0.1));
V_2=5*(1-exp(-Time/0.1));
V_3=7.5*(1-exp(-Time/0.1));
V_4=10*(1-exp(-Time/0.1));
plot(Time, V_1, Time, V_2, Time, V_3, Time, V_4);
```

```
xline(0.6)
hold off
legend('V_{2.5}','V_{5}','V_{7.5}','V_{10}')
title(legend,'Terminal velocity')
xlabel('Time (s)');
ylabel('Undisturbed wind speed (m/s)');
grid on
ylim([0 12]);
xlim([0 0.7]);
%%
%Swalwell et al. (2001) experimental data and simulation data for static validation.
RX = readmatrix('DataFile.xlsx','range','A29:A43');
RY = readmatrix('DataFile.xlsx','range','B29:B43');
ZX = readmatrix('DataFile.xlsx','range','C29:C43');
ZY = readmatrix('DataFile.xlsx','range','D29:D43');
CX = readmatrix('DataFile.xlsx','range','E29:E43');
CY = readmatrix('DataFile.xlsx','range','F29:F43');
BX = readmatrix('DataFile.xlsx','range','H29:H45');
BY = readmatrix('DataFile.xlsx','range','G29:G45');
plot(RX, RY,'r-o',ZX,ZY,'b-s',CX,CY,'c-d',BX,BY,'k-^');
legend('Swalwell et al. (2001) I = 0.6%','Swalwell et al. (2001) I = 4%','Swalwell et al. (2001) I = 7%','Simulation I = 7%')
hold on
xlabel('x/c');
ylabel('C_{Pressure}');
hold on
ylim([-3 1.5]);
xlim([0 1]);
%%
%Solidity vs optimal TSR function
S=0:0.05:0.8;
L=2.693*S.^(-0.329)-1.605;
plot(S,L)
grid on
xlabel('Solidity')
ylabel('Optimal tip speed ratio')
title('Turbine solidity vs. optimal TSR')
%%
%Results dynamic validation SB-VAWT
%Yamada et al. (2011) experimental data
YX = readmatrix('DataFile.xlsx','range','A51:A76');
YY = readmatrix('DataFile.xlsx','range','B51:B76');
YXi =linspace(min(YX), max(YX), 300); %nterpolation Vector
YYi = interp1(YX, YY, YXi, 'pchip');
%Qblade DMST data
QX = readmatrix('DataFile.xlsx','range','C51:C70');
QY = readmatrix('DataFile.xlsx','range','D51:D70');
QXi =linspace(min(YX), max(YX), 300); %Interpolation Vector
QYi = interp1(QX, QY, QXi, 'pchip');
%SST k-omega model data
OX = readmatrix('DataFile.xlsx','range','A19:A24');
OY = readmatrix('DataFile.xlsx','range','I19:I24');
OXi =linspace(min(OX), max(OX), 300); %Interpolation Vector
OYi = interp1(OX, OY, OXi, 'pchip');
plot(OX,OY,'bs');
hold on
plot(YX,YY, 'g*');
```

```
hold on
plot(QX,QY, 'k^');
hold on
plot(OXi,OYi,'-b');
hold on
plot(YXi,YYi, '-g');
hold on
plot(QXi,QYi, '-k');
hold on
err = 0.013*ones(size(YY));
errorbar(YX,YY,err, 'g')
legend('SST k-\omega model','Yamada et al., 2011 (Experiment)', 'QBlade (DMST)');
title(legend, 'V_{\infty}= 6 m/s');
ax = gca;
ax.FontSize = 12;
grid on
xlabel('TSR');
ylabel('C_{p}');
ylim([0 0.4]);
xlim([0 2.5]);
xticks(0:0.25:2.5);
%%
%WIND SPEED 2 m/s
%Coefficient of power
Cp_V = readmatrix('DataFile.xlsx','range','H3:H8');
Cp_SB = readmatrix('DataFile.xlsx','range','I3:I8');
TSR = readmatrix('DataFile.xlsx','range','J3:J8');
TSRi =linspace(min(TSR), max(TSR), 300); %Interpolation Vector
Cpi_V = interp1(TSR, Cp_V, TSRi, 'pchip');
Cpi_SB = interp1(TSR, Cp_SB, TSRi, 'pchip');
t = tiledlayout(2,1);
t.TileSpacing = 'tight';
nexttile
plot(TSR,Cp_V,'ro');
hold on
plot(TSR,Cp_SB,'b^');
hold on
plot(TSRi,Cpi_V,'-r');
hold on
plot(TSRi,Cpi_SB,'-b');
hold on
legend('C_p (V-VAWT)','C_p (SB-VAWT)');
title(legend, 'V_{\infty}= 2 m/s');
ax = gca;
ax.FontSize = 12;
xlabel('TSR')
xlim([0,2.5]);
xticks(0:(2.5/10):2.5);
ylabel('C_{p}')
ylim([0,0.25]);
yticks(0:0.1:0.2);
set(gcf,'Position',[100 100 100 100])
nexttile
%Coefficient of torque
Cm_V = readmatrix('DataFile.xlsx','range','E3:E8');
Cm_SB = readmatrix('DataFile.xlsx','range','F3:F8');
TSR = readmatrix('DataFile.xlsx','range','J3:J8');
```

```
TSRi =linspace(min(TSR), max(TSR), 300); %Interpolation Vector
Cmi_V = interp1(TSR, Cm_V, TSRi, 'pchip');
Cmi_SB = interp1(TSR, Cm_SB, TSRi, 'pchip');
plot(TSR,Cm_V,'ro');
hold on
plot(TSR,Cm_SB,'b^');
hold on
plot(TSRi,Cmi_V,'-r');
hold on
plot(TSRi,Cmi_SB,'-b');
hold on
legend('C_m (V-VAWT)','C_m (SB-VAWT)');
title(legend, 'V_{\infty}= 2 m/s');
ax = gca;
ax.FontSize = 12;
xlabel('TSR')
xlim([0,2.5]);
xticks(0:(2.5/10):2.5);
ylabel('C_{m}')
ylim([0,0.25]);
yticks(0:0.1:0.2);
set(gcf,'Position',[100 100 100 100])
%Average power coefficient
APC_SB = trapz(TSR, Cp_SB)/2.25;
APC_V = trapz(TSR, Cp_V)/2.25;
%%
%Coefficient of lift V-VAWT & SB-VAWT at 2 m/s and TSR=1.25
CL_V= readmatrix('DataFile.xlsx','range','A79:A439');
CL_SB= readmatrix('DataFile.xlsx','range','B79:B439');
Theta= readmatrix('DataFile.xlsx','range','C79:C439');
plot(Theta,CL_V,'r', Theta, CL_SB,'b');
legend('C_L (V-VAWT)','C_L (SB-VAWT)');
title(legend, 'V_{\infty}= 2 m/s at \lambda=1.25');
ax = gca;
ax.FontSize = 12;
xlabel('Azimuth angle \theta')
xlim([0,360]);
xticks(0:30:360);
ylabel('C_{L}')
ylim([-0.2,1]);
yticks(-0.2:0.1:1);
%%
%WIND SPEED 3 m/s
%Coefficient of power
Cp_V = readmatrix('DataFile.xlsx','range','H11:H16');
Cp_SB = readmatrix('DataFile.xlsx','range','I11:I16');
TSR = readmatrix('DataFile.xlsx','range','J3:J8');
TSRi =linspace(min(TSR), max(TSR), 300); %Interpolation Vector
Cpi_V = interp1(TSR, Cp_V, TSRi, 'pchip');
Cpi_SB = interp1(TSR, Cp_SB, TSRi, 'pchip');
t = tiledlayout(2,1);
t.TileSpacing = 'tight';
nexttile
plot(TSR,Cp_V,'rs');
hold on
plot(TSR,Cp_SB,'bd');
hold on
plot(TSRi,Cpi_V,'-r');
```

```
hold on
plot(TSRi,Cpi_SB,'-b');
hold on
legend('C_p (V-VAWT)','C_p (SB-VAWT)');
title(legend, 'V_{\infty}= 3 m/s');
ax = gca;
ax.FontSize = 12;
xlabel('TSR')
xlim([0,2.5]);
xticks(0:(2.5/10):2.5);
ylabel('C_{p}')
ylim([0,0.25]);
yticks(0:0.1:0.2);
set(gcf,'Position',[100 100 100 100])
nexttile
hold on
%Coefficient of torque
Cm_V = readmatrix('DataFile.xlsx','range','E11:E16');
Cm_SB = readmatrix('DataFile.xlsx','range','F11:F16');
TSR = readmatrix('DataFile.xlsx','range','J3:J8');
TSRi =linspace(min(TSR), max(TSR), 300); %Interpolation Vector
Cmi_V = interp1(TSR, Cm_V, TSRi, 'pchip');
Cmi_SB = interp1(TSR, Cm_SB, TSRi, 'pchip');
plot(TSR,Cm_V,'rs');
hold on
plot(TSR,Cm_SB,'bd');
hold on
plot(TSRi,Cmi_V,'-r');
hold on
plot(TSRi,Cmi_SB,'-b');
hold on
legend('C_m (V-VAWT)','C_m (SB-VAWT)');
title(legend, 'V_{\infty}= 3 m/s');
ax = gca;
ax.FontSize = 12;
xlabel('TSR')
xlim([0,2.5]);
xticks(0:(2.5/10):2.5);
ylabel('C_{m}')
ylim([0,0.25]);
yticks(0:0.1:0.2);
set(gcf,'Position',[100 100 100 100])
%Average power coefficient
APC_SB = trapz(TSR, Cp_SB)/2.25;
APC_V = trapz(TSR, Cp_V)/2.25;
%%
%WIND SPEED 6 m/s
%Coefficient of power
Cp_SB = readmatrix('CmCpTSR.xlsx','range','I19:I24');
TSR = readmatrix('CmCpTSR.xlsx','range','J3:J8');
TSRi =linspace(min(TSR), max(TSR), 300); %Interpolation Vector
Cpi_SB = interp1(TSR, Cp_SB, TSRi, 'pchip');
plot(TSR,Cp_SB,'bd');
hold on
plot(TSRi,Cpi_SB,'-b');
hold on
legend('C_p (V-VAWT)');
title(legend, 'V_{\infty}= 6 m/s');
```

```
ax = gca;
ax.FontSize = 12;
xlabel('TSR')
xlim([0,2.5]);
xticks(0:(2.5/10):2.5);
ylabel('C_{p}')
ylim([0,0.25]);
yticks(0:0.1:0.2);
set(gcf,'Position',[100 100 100 100]);
```

CHAPTER D

QBlade screenshots

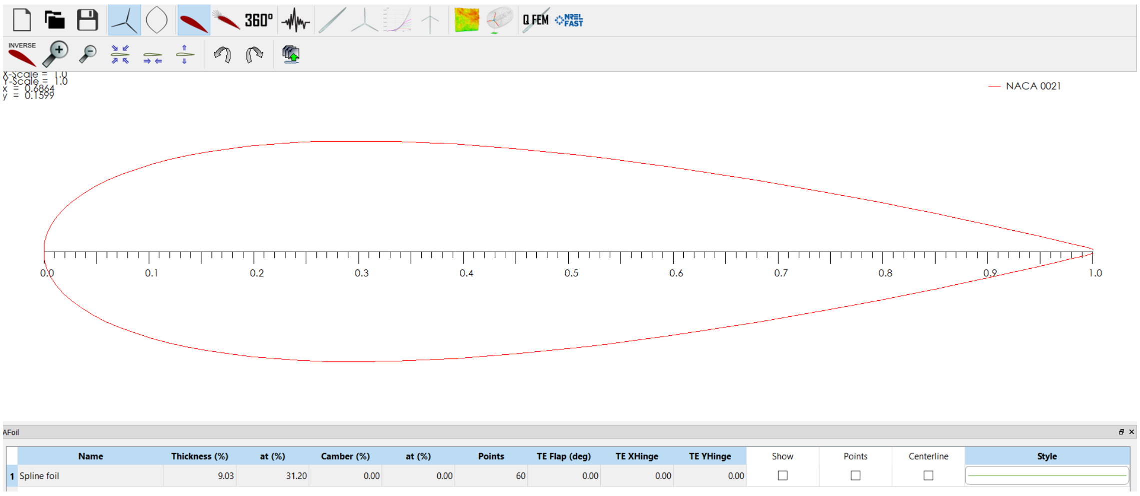

	Name	Thickness (%)	at (%)	Camber (%)	at (%)	Points	TE Flap (deg)	TE XHinge	TE YHinge	Show	Points	Centerline	Style
1	Spline foil	9.03	31.20	0.00	0.00	60	0.00	0.00	0.00	☐	☐	☐	

Figure 87: NACA 0021 parameters

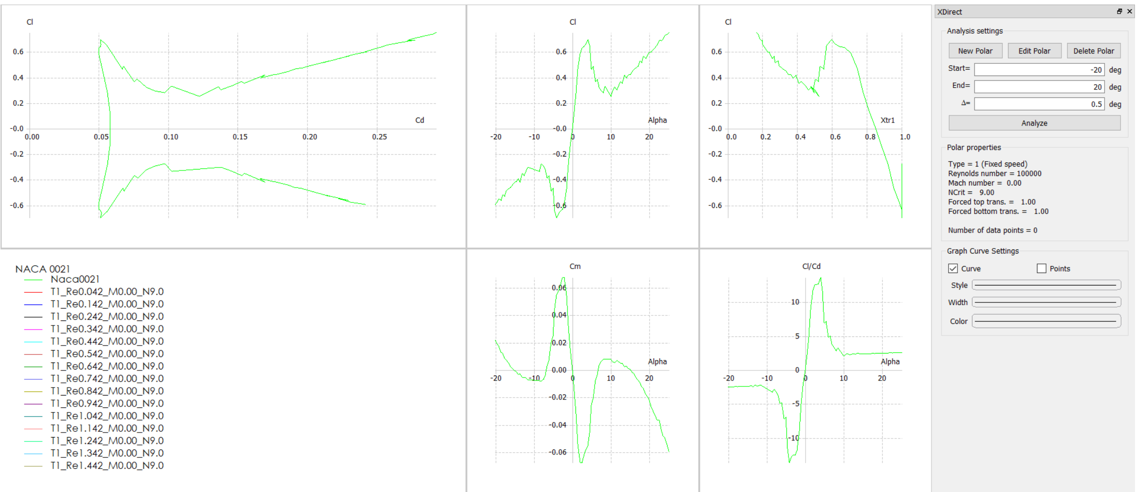

Start= -20 deg
End= 20 deg
Δ= 0.5 deg

Polar properties

Type = 1 (Fixed speed)
Reynolds number = 100000
Mach number = 0.00
NCrit = 9.00
Forced top trans. = 1.00
Forced bottom trans. = 1.00

Number of data points = 0

☑ Curve ☐ Points

Figure 88: NACA 0021 data

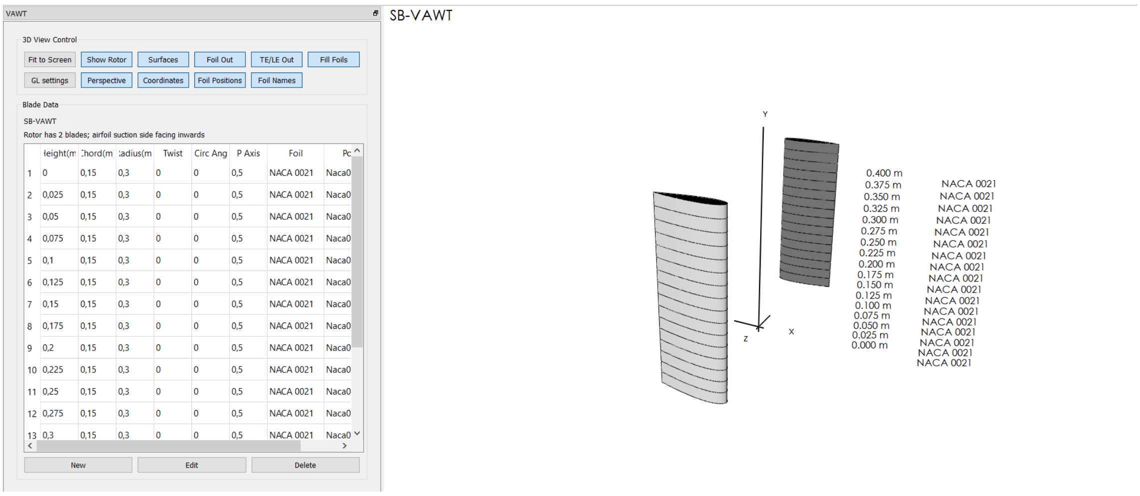

Blade Data

SB-VAWT

Rotor has 2 blades; airfoil suction side facing inwards

	‌Height(m	Chord(m	Radius(m	Twist	Circ Ang	P Axis	Foil	Pc
1	0	0,15	0,3	0	0	0,5	NACA 0021	Naca0
2	0,025	0,15	0,3	0	0	0,5	NACA 0021	Naca0
3	0,05	0,15	0,3	0	0	0,5	NACA 0021	Naca0
4	0,075	0,15	0,3	0	0	0,5	NACA 0021	Naca0
5	0,1	0,15	0,3	0	0	0,5	NACA 0021	Naca0
6	0,125	0,15	0,3	0	0	0,5	NACA 0021	Naca0
7	0,15	0,15	0,3	0	0	0,5	NACA 0021	Naca0
8	0,175	0,15	0,3	0	0	0,5	NACA 0021	Naca0
9	0,2	0,15	0,3	0	0	0,5	NACA 0021	Naca0
10	0,225	0,15	0,3	0	0	0,5	NACA 0021	Naca0
11	0,25	0,15	0,3	0	0	0,5	NACA 0021	Naca0
12	0,275	0,15	0,3	0	0	0,5	NACA 0021	Naca0
13	0,3	0,15	0,3	0	0	0,5	NACA 0021	Naca0

Figure 89: SB-VAWT CAD model

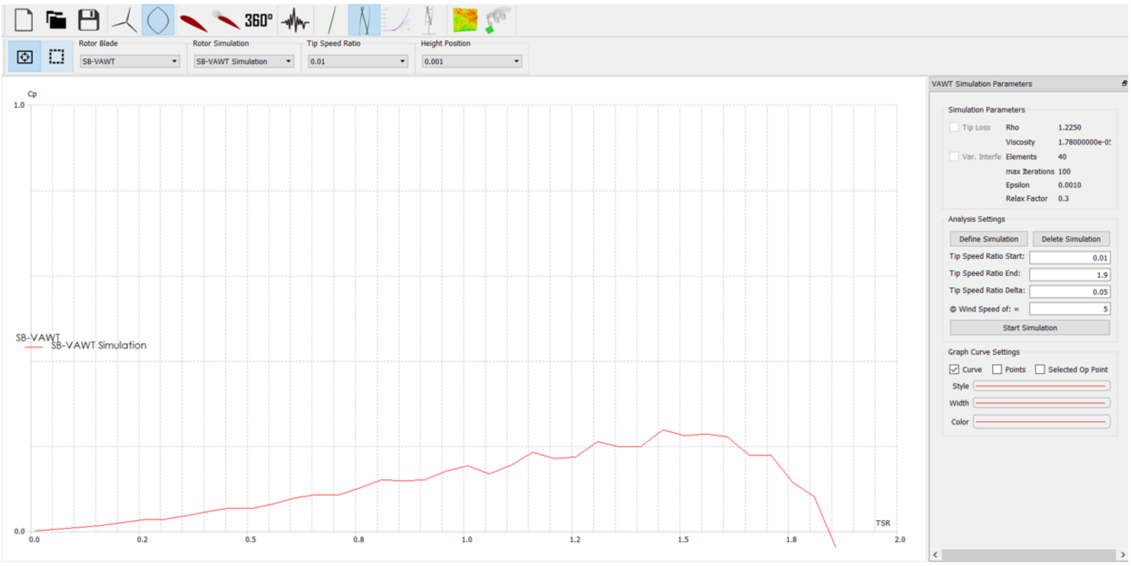

Rotor Blade: SB-VAWT

Rotor Simulation: SB-VAWT Simulation

Tip Speed Ratio: 0.01

Height Position: 0.001

Simulation Parameters

☐ Tip Loss

☐ Var. Interfe

Rho 1.2250

Viscosity 1.78000000e-0

Elements 40

max Iterations 100

Epsilon 0.0010

Relax Factor 0.3

Analysis Settings

Tip Speed Ratio Start: 0.01

Tip Speed Ratio End: 1.9

Tip Speed Ratio Delta: 0.05

@ Wind Speed of: = 5

Graph Curve Settings

☑ Curve ☐ Points ☐ Selected Op Point

Figure 90: SB-VAWT $C_p(\lambda)$ graph

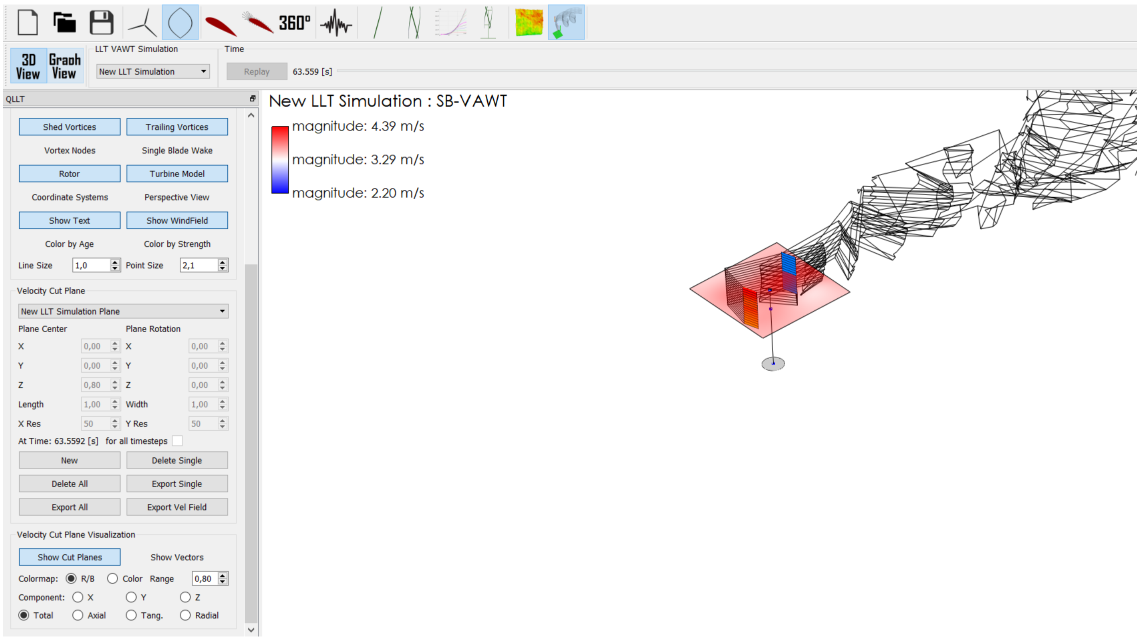

LLT VAWT Simulation: New LLT Simulation

Time: 63.559 [s]

Line Size 1,0
Point Size 2,1

Velocity Cut Plane: New LLT Simulation Plane

Plane Center: X 0,00; Y 0,00; Z 0,80
Plane Rotation: X 0,00; Y 0,00; Z 0,00
Length 1,00
Width 1,00
X Res 50
Y Res 50
At Time: 63.5592 [s] for all timesteps ☐

Velocity Cut Plane Visualization

Colormap: ● R/B ○ Color Range 0,80
Component: ○ X ○ Y ○ Z
● Total ○ Axial ○ Tang. ○ Radial

New LLT Simulation : SB-VAWT

magnitude: 4.39 m/s
magnitude: 3.29 m/s
magnitude: 2.20 m/s

Figure 91: SB-VAWT simulation

References

[1] *A change in orientation*. URL: `https://www.vertaxwind.com/`. (accessed: 15.01.2022).

[2] Ira H Abbott, Albert E Von Doenhoff, and Louis Stivers Jr. *Summary of airfoil data*. Tech. rep. 1945.

[3] Ramez Abdallah et al. “Estimating the optimum tilt angles for south-facing surfaces in Palestine”. In: *Energies* 13.3 (2020), p. 623.

[4] Gebreel Abdalrahman, William Melek, and Fue-Sang Lien. “Pitch angle control for a small-scale Darrieus vertical axis wind turbine with straight blades (H-Type VAWT)”. In: *Renewable energy* 114 (2017), pp. 1353–1362.

[5] Hashem Abusannuga and Mehmet Özkaymak. “The effect of geometry variants on the performance of VAWT-rotor with incline-straight blades”. In: *AIP Advances* 11.4 (2021), p. 045307.

[6] *Aerogenerator X*. URL: `https://grimshaw.global/projects/aerogenerator-x/`. (accessed: 15.01.2022).

[7] Mojtaba Ahmadi-Baloutaki, Rupp Carriveau, and David SK Ting. “Straight-bladed vertical axis wind turbine rotor design guide based on aerodynamic performance and loading analysis”. In: *Proceedings of the Institution of Mechanical Engineers, Part A: Journal of Power and Energy* 228.7 (2014), pp. 742–759.

[8] Hiromichi Akimoto, Kenji Tanaka, and Kiyoshi Uzawa. “Floating axis wind turbines for offshore power generation—a conceptual study”. In: *Environmental Research Letters* 6.4 (2011), p. 044017.

[9] Mohammed Hadi Ali et al. “Experimental comparison study for Savonius wind turbine of two & three blades at low wind speed”. In: *International Journal of Modern Engineering Research (IJMER)* 3.5 (2013), pp. 2978–2986.

[10] KM Almohammadi et al. “Computational fluid dynamics (CFD) mesh independency techniques for a straight blade vertical axis wind turbine”. In: *Energy* 58 (2013), pp. 483–493.

[11] AR Amelia et al. “Technologies of solar tracking systems: A review”. In: *IOP Conference Series: Materials Science and Engineering*. Vol. 767. 1. IOP Publishing. 2020, p. 012052.

[12] Roberto Lacal Arantegui and Arnulf Jäger-Waldau. “Photovoltaics and wind status in the European Union after the Paris Agreement”. In: *Renewable and Sustainable Energy Reviews* 81 (2018), pp. 2460–2471.

[13] Luis Arturo Soriano, Wen Yu, and Jose de Jesus Rubio. “Modeling and control of wind turbine”. In: *Mathematical Problems in Engineering* 2013 (2013).

[14] Thomas D Ashwill and Timothy M Leonard. *Developments in blade shape design for a Darrieus vertical axis wind turbine.* Citeseer, 1986.

[15] S Aziz and S Hassan. “On improving the efficiency of a solar panel tracking system”. In: *Procedia Manufacturing* 7 (2017), pp. 218–224.

[16] Nader Barsoum et al. “Fabrication of dual-axis solar tracking controller project”. In: *Intelligent Control and Automation* 2.02 (2011), p. 57.

[17] Ben F Blackwell et al. “Engineering development status of the Darrieus wind turbine”. In: *Journal of Energy* 1.1 (1977), pp. 50–64.

[18] BF Blackwell and GE Reis. *Blade shape for a tropskien type of vertical-axis wind turbine.* Tech. rep. Sandia Labs., Albuquerque, NM (USA), 1977.

[19] Michael Borg, Andrew Shires, and Maurizio Collu. “Offshore floating vertical axis wind turbines, dynamics modelling state of the art. Part I: Aerodynamics”. In: *Renewable and Sustainable Energy Reviews* 39 (2014), pp. 1214–1225.

[20] S Brusca, R Lanzafame, and M Messina. “Design of a vertical-axis wind turbine: how the aspect ratio affects the turbine’s performance”. In: *International Journal of Energy and Environmental Engineering* 5.4 (2014), pp. 333–340.

[21] Yunus Celik et al. “Aerodynamic investigation of the start-up process of H-type vertical axis wind turbines using CFD”. In: *Journal of Wind Engineering and Industrial Aerodynamics* 204 (2020), p. 104252.

[22] Yunus Celik et al. “Design and aerodynamic performance analyses of the self-starting H-type VAWT having J-shaped aerofoils considering various design parameters using CFD”. In: *Energy* 251 (2022), p. 123881.

[23] S Chandramouli et al. “Numerical analysis of effect of pitch angle on a small scale vertical axis wind turbine”. In: *International Journal of Renewable Energy Research (IJRER)* 4.4 (2014), pp. 929–935.

[24] Weiyong Chen and CY Zhou. “Application of numercal simulation to obtain the optimization pitch angle for VAWT”. In: *2009 World Non-Grid-Connected Wind Power and Energy Conference.* IEEE. 2009, pp. 1–5.

[25] WT Chong et al. “Performance investigation of a power augmented vertical axis wind turbine for urban high-rise application”. In: *Renewable Energy* 51 (2013), pp. 388–397.

[26] Prasad Chougule and Soren Nielsen. “Overview and Design of self-acting pitch control mechanism for vertical axis wind turbine using multi body simulation approach”. In: *Journal of physics: conference series.* Vol. 524. 1. IOP Publishing. 2014, p. 012055.

[27] T Dagdevir et al. “NUMERICAL INVESTIGATION OF AERODYNAMIC CHARACTERISTICS FOR THREE BLADED DARRIEUS WIND TURBINE ON NACA0021, NACA0015 AND CLARK-Y”. In: ().

[28] GJM Darrieus. “Turbine having its rotating shaft transverse to the flow of current (patent no.: 1835018)”. In: (1931).

[29] Abdul Salam Darwish and Riadh Al-Dabbagh. “Wind energy state of the art: present and future technology advancements”. In: *Renewable Energy and Environmental Sustainability* 5 (2020), p. 7.

[30] Naresh V Datla et al. “Towards a nitinol actuator for an active surgical needle”. In: *Smart Materials, Adaptive Structures and Intelligent Systems.* Vol. 45103. American Society of Mechanical Engineers. 2012, pp. 265–269.

[31] Thomas W Duerig, KN Melton, and DWCM Stöckel. *Engineering aspects of shape memory alloys.* Butterworth-heinemann, 2013.

[32] Ravi K Duggirala, Christopher J Roy, and Joseph A Schetz. “Analysis of interference drag for strut-strut interaction in transonic flow”. In: *AIAA journal* 49.3 (2011), pp. 449–462.

[33] Okeoghene Eboibi, Louis Angelo M Danao, and Robert J Howell. “Experimental investigation of the influence of solidity on the performance and flow field aerodynamics of vertical axis wind turbines at low Reynolds numbers”. In: *Renewable Energy* 92 (2016), pp. 474–483.

[34] T. J. M. Eijkhout. *Literature Assignment: Design of Sustainable Smart Material Structures Adaptable to External Stimuli.* Delft University of Technology, 2021.

[35] Abd Elmaged and Hiba Kamal. “Passive solar tracking system”. PhD thesis. UOFK, 2015.

[36] Sandra Eriksson, Hans Bernhoff, and Mats Leijon. “Evaluation of different turbine concepts for wind power”. In: *renewable and sustainable energy reviews* 12.5 (2008), pp. 1419–1434.

[37] Rashid Ahammed Ferdaus et al. “Energy efficient hybrid dual axis solar tracking system”. In: *Journal of Renewable Energy* 2014 (2014).

[38] William Froude. *On the elementary relation between pitch, slip, and propulsive efficiency.* Tech. rep. 1920.

[39] Masoud Ghasemian and Amir Nejat. “Aero-acoustics prediction of a vertical axis wind turbine using Large Eddy Simulation and acoustic analogy”. In: *Energy* 88 (2015), pp. 711–717.

[40] Hermann Glauert. “Airplane propellers”. In: *Aerodynamic theory.* Springer, 1935, pp. 169–360.

[41] Florin Grofu. “Control system for photovoltaic panels tracker”. In: *Fiabilitate si Durabilitate* 2018 (2018), pp. 333–338.

[42] Yonghui Guo et al. “Aerodynamic analysis of a step adjustment method for blade pitch of a VAWT”. In: *Journal of Wind Engineering and Industrial Aerodynamics* 188 (2019), pp. 90–101.

[43] M Saqib Hameed and S Kamran Afaq. “Design and analysis of a straight bladed vertical axis wind turbine blade using analytical and numerical techniques”. In: *Ocean Engineering* 57 (2013), pp. 248–255.

[44] Brian Hand and Andrew Cashman. “A review on the historical development of the lift-type vertical axis wind turbine: From onshore to offshore floating application”. In: *Sustainable Energy Technologies and Assessments* 38 (2020), p. 100646.

[45] Brian Hand, Ger Kelly, and Andrew Cashman. “Aerodynamic design and performance parameters of a lift-type vertical axis wind turbine: A comprehensive review”. In: *Renewable and Sustainable Energy Reviews* 139 (2021), p. 110699.

[46] Nandita Hari, Joseph A Schetz, and Rakesh K Kapania. “Numerical prediction of interference drag of a strut-surface intersection in supersonic flow”. In: *AIAA Scitech 2019 Forum.* 2019, p. 0295.

[47] A Reza Hassanzadeh et al. “Comparison of conventional and helical savonius marine current turbine using computational fluid dynamics”. In: *World Applied Sciences Journal* 28.8 (2013), pp. 1113–1119.

[48] Prabhakar R Holambe, DB Talange, and VB Bhole. “Motorless solar tracking system”. In: *2015 International Conference on Energy Systems and Applications.* IEEE. 2015, pp. 358–363.

[49] WC Hsieh et al. “Experimental study on performance of vertical axis wind turbine with NACA 4-digital series of blades”. In: *Advanced Materials Research.* Vol. 488. Trans Tech Publ. 2012, pp. 1055–1061.

[50] W Huang. “On the selection of shape memory alloys for actuators”. In: *Materials and design* 23.1 (2002), pp. 11–19.

[51] W Huang and W Toh. “Training two-way shape memory alloy by reheat treatment”. In: *Journal of materials science letters* 19.17 (2000), pp. 1549–1550.

[52] S. I. et al Ibrahim. “Desert Reconstruction”. PhD thesis. POWER and MACHINE DEPT. FACULTY OF ENGINEERING AL-AZHAR UNIVERSITY, May 2014.

[53] TF Ishugah et al. “Advances in wind energy resource exploitation in urban environment: A review”. In: *Renewable and sustainable energy reviews* 37 (2014), pp. 613–626.

[54] Mazharul Islam, David S-K Ting, and Amir Fartaj. “Aerodynamic models for Darrieus-type straight-bladed vertical axis wind turbines”. In: *Renewable and sustainable energy reviews* 12.4 (2008), pp. 1087–1109.

[55] Mazharul Islam, David SK Ting, and Amir Fartaj. “Design of a special-purpose airfoil for smaller-capacity straight-bladed VAWT”. In: *Wind Engineering* 31.6 (2007), pp. 401–424.

[56] Siddhant Jain and Ujjwal K Saha. “The state-of-the-art technology of H-type darrieus wind turbine rotors”. In: *Journal of Energy Resources Technology* 142.3 (2020).

[57] Houigab Jeong, Seungho Lee, and Soon-Duck Kwon. “Blockage corrections for wind tunnel tests conducted on a Darrieus wind turbine”. In: *Journal of Wind Engineering and Industrial Aerodynamics* 179 (2018), pp. 229–239.

[58] Savonius Sigurd Johannes. *Rotor adapted to be driven by wind or flowing water.* US Patent 1,697,574. Jan. 1929.

[59] M Johari, Muhd Jalil, and Mohammad Faizal Mohd Shariff. “Comparison of horizontal axis wind turbine (HAWT) and vertical axis wind turbine (VAWT)”. In: *International Journal of Engineering and Technology* 7.4.13 (2018), pp. 74–80.

[60] Milos Jovanovic, Zeljko Despotovic, and Djordje Urukalo. “The chronological system of solar tracking implemented on mobile solar generator-IMP MSEG”. In: *Zbornik Medjunarodne konferencije o obnovljivim izvorima elektricne energije–MKOIEE* 5.1 (2017), pp. 107–113.

[61] Manivannan Sivaperuman Kalairaj et al. “Nitinol actuated soft structures towards transnasal drug delivery: a pilot cadaver study”. In: *Medical & biological engineering & computing* 58.3 (2020), pp. 611–623.

[62] George B Kauffman and Isaac Mayo. “The story of nitinol: the serendipitous discovery of the memory metal and its applications”. In: *The chemical educator* 2.2 (1997), pp. 1–21.

[63] Ozan Keysan et al. “C-GEN, a lightweight direct drive generator for marine energy converters”. In: (2010).

[64] Leonardo Brito Kothe, Sérgio Viçosa Möller, and Adriane Prisco Petry. “Numerical and experimental study of a helical Savonius wind turbine and a comparison with a two-stage Savonius turbine”. In: *Renewable Energy* 148 (2020), pp. 627–638.

[65] Vimal Kumar, Marius Paraschivoiu, and Ion Paraschivoiu. “Low Reynolds number vertical axis wind turbine for Mars”. In: *Wind Engineering* 34.4 (2010), pp. 461–476.

[66] L Lazauskas. “Three pitch control systems for vertical axis wind turbines compared”. In: *Wind engineering* (1992), pp. 269–282.

[67] Ying-bin Liang et al. “Blade pitch control of straight-bladed vertical axis wind turbine”. In: *Journal of Central South University* 23.5 (2016), pp. 1106–1114.

[68] Yinong Liu, Yong Liu, and Jan Van Humbeeck. “Two-way shape memory effect developed by martensite deformation in NiTi”. In: *Acta materialia* 47.1 (1998), pp. 199–209.

[69] Ji Ma, Ibrahim Karaman, and Ronald D Noebe. “High temperature shape memory alloys”. In: *International Materials Reviews* 55.5 (2010), pp. 257–315.

[70] Abbas Fadhil Mahmood and Haider Lafta Aneed. “Improving Aerodynamic Coefficients of an airfoil using suspended wing”. In: *Dijlah Journal* 3.3 (2020).

[71] Andrés Meana-Fernández et al. “Proposal of an Optimized Airfoil Geometry for Vertical-Axis Wind Turbine Applications”. In: *Multidisciplinary Digital Publishing Institute Proceedings*. Vol. 2. 23. 2018, p. 1464.

[72] Sander Mertens, Gijs van Kuik, and Gerard van Bussel. “Performance of an H-Darrieus in the skewed flow on a roof”. In: *J. Sol. Energy Eng.* 125.4 (2003), pp. 433–440.

[73] T Micha Premkumar et al. “Numerical Studies on the Effect of Cambered Airfoil Blades on Self-Starting of Vertical Axis Wind Turbine Part 1: NACA 0012 and NACA 4415”. In: *Applied Mechanics and Materials*. Vol. 787. Trans Tech Publ. 2015, pp. 250–254.

[74] Adit Sunil Misar and Mesbah Uddin. *Effects of Solver Parameters and Boundary Conditions on RANS CFD Flow Prediction Over a Gen-6 NASCAR Racecar*. Tech. rep. SAE Technical Paper, 2022.

[75] *Modeling Turbulence*. ANSYS Inc. URL: `https://www.afs.enea.it/project/neptunius/docs/fluent/html/ug/node405.htm#chap-turbulence`.

[76] MH Mohamed. "Impacts of solidity and hybrid system in small wind turbines performance". In: *Energy* 57 (2013), pp. 495–504.

[77] MH Mohamed. "Reduction of the generated aero-acoustics noise of a vertical axis wind turbine using CFD (Computational Fluid Dynamics) techniques". In: *Energy* 96 (2016), pp. 531–544.

[78] Amin A Mohammed et al. "Vertical axis wind turbine aerodynamics: summary and review of momentum models". In: *Journal of Energy Resources Technology* 141.5 (2019).

[79] Palanisamy Mohan Kumar et al. "Review on the evolution of Darrieus vertical axis wind turbine: Large wind turbines". In: *Clean Technologies* 1.1 (2019), pp. 205–223.

[80] Erik Möllerström et al. "Noise propagation from a vertical axis wind turbine". In: *inter. noise 2014, 43rd International Congress on Noise Control Engineering, Melbourne, Australia, November 16-19, 2014*. Australian Acoustical Society. 2014.

[81] Gerald Müller et al. "A resistance type vertical axis wind turbine for building integration". In: *Renewable Energy* 111 (2017), pp. 803–814.

[82] BG Newman. "Multiple actuator-disc theory for wind turbines". In: *Journal of Wind Engineering and Industrial Aerodynamics* 24.3 (1986), pp. 215–225.

[83] Chi-Cong Nguyen, Phat-Tai Tran, et al. "A numerical study of thickness effect of the symmetric NACA 4-digit airfoils on self starting capability of a 1kW H-type vertical axis wind turbine". In: *International Journal of Mechanical Engineering and Applications* 3.3 (2015), p. 7.

[84] Lam Nguyen and Meredith Metzger. "Optimization of a vertical axis wind turbine for application in an urban/suburban area". In: *Journal of Renewable and sustainable Energy* 9.4 (2017), p. 043302.

[85] Walter Nsengiyumva et al. "Recent advancements and challenges in Solar Tracking Systems (STS): A review". In: *Renewable and Sustainable Energy Reviews* 81 (2018), pp. 250–279.

[86] Özer ÖĞÜÇLÜ. "Structural Design and Stress Analysis of a Helical Vertical Axis Wind Turbine Blade". In: *Sakarya Üniversitesi Fen Bilimleri Enstitüsü Dergisi* 24.6 (2020), pp. 1151–1161.

[87] *Open Jet Facility*. URL: `https://www.tudelft.nl/lr/organisatie/afdelingen/aerodynamics-wind-energy-flight-performance-and-propulsion/facilities/low-speed-wind-tunnels/open-jet-facility`. (accessed: 27.05.2022).

[88] Ion Paraschivoiu. "Double-multiple streamtube model for studying vertical-axis wind turbines". In: *Journal of propulsion and power* 4.4 (1988), pp. 370–377.

[89] Jeff Perkins and D Hodgson. "The two-way shape memory effect". In: *Engineering aspects of shape memory alloys* (1990), pp. 195–206.

[90] Sayyad Basim Qamar and Isam Janajreh. "A comprehensive analysis of solidity for cambered darrieus VAWTs". In: *International Journal of Hydrogen Energy* 42.30 (2017), pp. 19420–19431.

[91] M Ragheb. "Optimal rotor tip speed ratio". In: *Lecture notes of Course no. NPRE* 475 (2014).

[92] M Ragheb. "Wind energy conversion theory, betz equation". In: *Wind Energie* (2014).

[93] William John Macquorn Rankine. "On the mechanical principles of the action of propellers". In: *Transactions of the Institution of Naval Architects* 6 (1865).

[94] Abdolrahim Rezaeiha, Ivo Kalkman, and Bert Blocken. "Effect of pitch angle on power performance and aerodynamics of a vertical axis wind turbine". In: *Applied energy* 197 (2017), pp. 132–150.

[95] Abdolrahim Rezaeiha, Hamid Montazeri, and Bert Blocken. “Towards optimal aerodynamic design of vertical axis wind turbines: Impact of solidity and number of blades”. In: *Energy* 165 (2018), pp. 1129–1148.

[96] Amine Riad et al. “Bio-sun tracker engineering self-driven by thermo-mechanical actuator for photovoltaic solar systems”. In: *Case Studies in Thermal Engineering* 21 (2020), p. 100709.

[97] Jihad Rishmany et al. “Optimization of a Vertical Axis Wind Turbine Using FEA, Multibody Dynamics and Wind Tunnel Testing”. In: (2017).

[98] JCAY Rizk and Y Chaiko. “Solar tracking system: more efficient use of solar panels”. In: *World Academy of Science, Engineering and Technology* 41 (2008), pp. 313–315.

[99] Sung-Cheoul Roh and Seung-Hee Kang. “Effects of a blade profile, the Reynolds number, and the solidity on the performance of a straight bladed vertical axis wind turbine”. In: *Journal of Mechanical Science and Technology* 27.11 (2013), pp. 3299–3307.

[100] Allan Soon Chan Roong and Shin-Horng Chong. “Laboratory-scale single axis solar tracking system: Design and implementation”. In: *International Journal of Power Electronics and Drive Systems* 7.1 (2016), p. 254.

[101] TAU Roshan et al. “Development of a PID based closed loop controller for shape memory alloy actuators”. In: *2018 Moratuwa Engineering Research Conference (MERCon)*. IEEE. 2018, pp. 460–464.

[102] Magedi Moh M Saad and Norzelawati Asmuin. “Comparison of horizontal axis wind turbines and vertical axis wind turbines”. In: *IOSR Journal of Engineering (IOSRJEN)* 4.08 (2014), pp. 27–30.

[103] A Sagharichi, M Zamani, and Am Ghasemi. “Effect of solidity on the performance of variable-pitch vertical axis wind turbine”. In: *Energy* 161 (2018), pp. 753–775.

[104] TA Schroeder and CM Wayman. “The two-way shape memory effect and other “training” phenomena in Cu-Zn single crystals”. In: *Scripta metallurgica* 11.3 (1977), pp. 225–230.

[105] *SeaTwirl S2. The Next Generation Wind Power.* URL: `https://seatwirl.com/products/seatwirl-s2/`. (accessed: 15.01.2022).

[106] Thomas Sebastian and Matthew A Lackner. “Development of a free vortex wake method code for offshore floating wind turbines”. In: *Renewable Energy* 46 (2012), pp. 269–275.

[107] John A Shaw et al. “Tips and tricks for characterizing shape memory alloy wire: part 1—differential scanning calorimetry and basic phenomena”. In: (2008).

[108] Andrew Shires. “Design optimisation of an offshore vertical axis wind turbine”. In: *Proceedings of the Institution of Civil Engineers-Energy* 166.1 (2013), pp. 7–18.

[109] Vivek Shukla and Ajay Kumar Kaviti. “Performance evaluation of profile modifications on straight-bladed vertical axis wind turbine by energy and Spalart Allmaras models”. In: *Energy* 126 (2017), pp. 766–795.

[110] Amit Pratap Singh and Indresh Yadav. “A Review on The Axis Tracking Used for Solar PV Application”. In: *IOP Conference Series: Materials Science and Engineering*. Vol. 1116. 1. IOP Publishing. 2021, p. 012063.

[111] AM Siregar and Chandra A Siregar. “Reliability test prototype wind turbine savonius type helical as an alternative electricity generator”. In: *IOP Conference Series: Materials Science and Engineering*. Vol. 674. 1. IOP Publishing. 2019, p. 012059.

[112] David A Spera. “Wind turbine technology”. In: (1994).

[113] James H Strickland. *Darrieus turbine: a performance prediction model using multiple streamtubes*. Tech. rep. Sandia Labs., Albuquerque, N. Mex.(USA), 1975.

[114] Xiaojing Sun, Diangui Huang, and Guoqing Wu. “The current state of offshore wind energy technology development”. In: *Energy* 41.1 (2012), pp. 298–312.

[115] Herbert J Sutherland, Dale E Berg, and Thomas D Ashwill. “A retrospective of VAWT technology”. In: *Sandia National Laboratories* (2012), pp. 1–64.

[116] Katrina E Swalwell, John Sheridan, WH Melbourne, et al. "The effect of turbulence intensity on stall of the NACA 0021 aerofoil". In: *14th Australasian fluid mechanics conference*. 2001, pp. 941–944.

[117] K Takeda and M Kato. "Wind tunnel blockage effects on drag coefficient and wind-induced vibration". In: *Journal of Wind Engineering and Industrial Aerodynamics* 42.1-3 (1992), pp. 897–908.

[118] Student Design Team et al. "Conceptual Design of a Martian Power Generating System Utilizing Solar and Wind Energy". In: ().

[119] RJ Templin. *Aerodynamic performance theory for the NRC vertical-axis wind turbine*. Tech. rep. National Aeronautical Establishment, Ottawa, Ontario (Canada), 1974.

[120] Jerin Kuriakose Tharamuttam and Andrew Keong Ng. "Design and development of an automatic solar tracker". In: *Energy Procedia* 143 (2017), pp. 629–634.

[121] Wenlong Tian et al. "Numerical study of energy recovery from the wakes of moving vehicles on highways by using a vertical axis wind turbine". In: *Energy* 141 (2017), pp. 715–728.

[122] Willy Tjiu et al. "Darrieus vertical axis wind turbine for power generation I: Assessment of Darrieus VAWT configurations". In: *Renewable energy* 75 (2015), pp. 50–67.

[123] Annemiek Van Boeijen et al. *Delft design guide: Design strategies and methods*. 2014.

[124] *Vertical Offshore Wind Turbines More Efficient than Conventional Ones, Study Shows*. URL: `http://www.oedigital.com/`. (accessed: 20.01.2022).

[125] *Vertical Sky A32*. URL: `https://www.agilewindpower.com/en/product`. (accessed: 1.07.2022).

[126] Nicolò Viti, Daniel Valero, and Carlo Gualtieri. "Numerical simulation of hydraulic jumps. Part 2: Recent results and future outlook". In: *Water* 11.1 (2019), p. 28.

[127] CM Vivek et al. "A review on vertical and horizontal axis wind turbine". In: *International Research Journal of Engineering and Technology (IRJET)* 4.4 (2017), pp. 247–250.

[128] Abdul Wadood. "Brief overview on nitinol as biomaterial". In: *Advances in Materials Science and Engineering* 2016 (2016).

[129] F. M. White. *Fluid mechanics fifth edition*. Boston, Massachusetts: WCB/McGraw-Hill, 1999.

[130] Robert Whittlesey. "Vertical axis wind turbines: Farm and turbine design". In: *Wind Energy Engineering*. Elsevier, 2017, pp. 185–202.

[131] Seiji Yamada, Tomohiro Tamura, and Shinsuke Mochizuki. "Effects of wing section on mean characteristics and temporal torque Variation for a small straight-bladed vertical axis wind turbine". In: *Journal of Fluid Science and Technology* 6.6 (2011), pp. 875–886.

[132] Yingxue Yao et al. "A multipurpose dual-axis solar tracker with two tracking strategies". In: *Renewable Energy* 72 (2014), pp. 88–98.

[133] Li-xun Zhang et al. "Effect of blade pitch angle on aerodynamic performance of straight-bladed vertical axis wind turbine". In: *Journal of Central South University* 21.4 (2014), pp. 1417–1427.

[134] Haitian Zhu et al. "Effect of geometric parameters of Gurney flap on performance enhancement of straight-bladed vertical axis wind turbine". In: *Renewable Energy* 165 (2021), pp. 464–480.